Using tourmaline to track boron cycling at the Isua Belt, SW Greenland

Dominic J. D'Amato, Earth and Planetary Sciences, McGill University, Montreal, Canada, submitted July, 2024

A thesis submitted to McGill University in partial fulfillment of the requirements of the degree of Masters of Science, Geology

Table of Contents:

Figures and Tables:

Acknowledgements

I have many people to thank for my success in completing this thesis. First, my to parents for always being supportive, encouraging my curiosity, and inspiring me to work hard. My advisor, Vincent van Hinsberg for being both a scientist and person who I admire on many levels – this would not have been possible without his patience, knowledge, enthusiasm, and guidance. My office friends – Raven Polk and Maude Bilodeau for helping to keep me sane when all else was failing and for taking my mind off research when it was needed. Catherine Crotty for teaching me how to say “no”, and how to use lab equipment at McGill during a time of uncertainty. Stan Roozen for explaining things slowly and always taking time whenever I had questions related to tourmaline. Dr. Jillian Kendrick for constantly helping me out with data processing, interpretation, and analytical work. This would not have been possible without her. Dr. Glenn Poirier for saving days of additional work due to his expertise on the EPMA and his patience. Lang Shi for being available whenever I called upon him for help and questions. Joshua Davies for helping with geochronological work, including processing data, helping with the interpretation of said data, and teaching me geochronological software. Andre Poirier for accommodating me whenever I needed to use the ICPMS at UQAM for geochronology. Jeanne Paquette for being an exceptional instructor and helping me understand how to teach concepts in ways that students can understand. Galen Halverson for being on my committee and asking relevant questions and being interested in the research. Darrell Henry for being my external reviewer and taking the time to give constructive feedback.

Abstract:

The early Earth was different in conditions and compositions of its geosphere, hydrosphere, and atmosphere compared to the present. The rock record provides a means to constrain these conditions, processes and compositions, but this requires an understanding of what these rocks represent and how they formed. Tourmaline-rich horizons in ca. 3.7 Ga Eoarchean rocks in the Isua belt of western Greenland have been suggested to represent enrichment of B in sediments and seawater, and this is important as B is considered key in the stabilization of prebiotic molecules such as ribose and pentose. Indeed, these tourmaline-rich rocks have been argued as proof for the existence of B-enriched environments promoting the emergence of life.

There are several issues with using tourmaline for this: 1. Tourmaline forms during metamorphism, and the host rock has passed through filters of diagenesis and metamorphism before being recorded, thereby complicating the use of tourmaline as a direct proxy for the surface sedimentary environment; 2. Tourmaline commonly has a complex growth history spanning the history of a rock; and 3. It can form from internally and externally derived B-sources, and may not represent redistribution of internally derived B.

Detailed petrography was conducted to determine tourmaline petrogenesis for 3 occurrences in the Eoarchean Isua belt meta-sediments. These include a tourmalinite, its metapelitic host schists, and a mafic schist containing a tourmaline vein. The vein tourmaline formed at ca. 400˚C, accompanied by metasomatism of the host rock and formation of tourmaline and apatite away from the vein. U-Pb dating of apatite places this B-metasomatism event at 1.7 Ga. The disseminated tourmalines in the meta-pelite nucleated at 400˚C followed by prograde growth to peak metamorphic conditions of 650˚C. Textures, compositional zoning, thermal history and tourmaline mode are consistent with closed-system formation from redistribution of a typical meta-pelite protolith B content. Tourmaline in the tourmalinite nucleated and grew at a constant T of 350˚C, followed by prograde to peak metamorphic history from 500 to ca. 600˚C. The temperature and composition of the initial growth indicate formation by external introduction of B. The composition of the tourmalinite is incompatible with known B-rich protoliths and thermodynamic modelling shows that its host rocks could not have been the precursor for B-metasomatism. Zircon U-Pb dating provides a protolith age of 3.7 Ga for the meta-pelites and a metamorphic age of 3.6 Ga for the tourmalinite, consistent with earlier geochronology.

Tourmaline in the northern part of the Isua belt has complex formation histories and formed in response to at least three events: an early B-metasomatism between 3.7 and 3.6 Ga, possibly linked to felsic magmatism; growth during closed-system progressive B-release during prograde metamorphism around 3.6 Ga; and a further B-metasomatism event at 1.7 Ga. Hence, tourmaline-rich rocks from Isua cannot be used to infer the presence of B-rich sediments in the Eoarchean nor to back-calculate Archean seawater compositions. Only disseminated tourmaline in meta-pelite formed under closed-system metamorphic conditions and has the potential to retain information on B in the protolith.

Résumé:

Les conditions et la composition de la géosphère, de l'hydrosphère et de l'atmosphère de la Terre primitive étaient différentes de celles de la Terre actuelle. L'enregistrement des roches permet de contraindre ces conditions, processus et compositions, mais il faut pour cela comprendre ce que ces roches représentent et comment elles se sont formées. Il a été suggéré que les horizons riches en tourmaline dans les roches éoarchéennes d'environ 3,7 Ga de la ceinture d'Isua, dans l'ouest du Groenland, représentent un enrichissement en B dans les sédiments et l'eau de mer, ce qui est important car le B est considéré comme un élément clé de la stabilisation des molécules prébiotiques telles que le ribose et le pentose. En effet, ces roches riches en tourmaline ont été considérées comme une preuve de l'existence d'environnements enrichis en B favorisant l'émergence de la vie.

L'utilisation de la tourmaline à cette fin pose plusieurs problèmes: 1. La tourmaline se forme au cours du métamorphisme et la roche hôte est passée par les filtres de la diagenèse et du métamorphisme avant d'être enregistrée, ce qui complique l'utilisation de la tourmaline comme indicateur direct de l'environnement sédimentaire de surface; 2. la

tourmaline a généralement une croissance complexe qui s'étend sur toute l'histoire d'une roche; et 3. elle peut se former à partir de roches internes et externes, mais aussi à partir de roches plus profondes. Elle peut se former à partir de sources de B d'origine interne et externe, et peut ne pas représenter une redistribution de B d'origine interne.

Une pétrographie détaillée a été réalisée pour déterminer la pétrogénèse de la tourmaline pour 3 occurrences dans les méta-sédiments de la ceinture d'Isua de l'Éoarchéen. Il s'agit d'une tourmalinite, de ses schistes hôtes métapélitiques et d'un schiste mafique contenant une veine de tourmaline. La veine de tourmaline s'est formée à env. 400˚C, accompagnée d'un métasomatisme de la roche hôte et de la formation de tourmaline et d'apatite loin de la veine. La datation U-Pb de l'apatite situe cet événement de métasomatisme B à 1,7 Ga. Les tourmalines disséminées dans la métapélite se sont formées à 400˚C, puis ont connu une croissance prograde jusqu'aux conditions métamorphiques maximales de 650˚C. Les textures, la zonation de la composition, l'histoire et le mode de tourmaline sont cohérents avec la formation d'un système fermé à partir de la redistribution du contenu B d'un protolithe méta-pélite typique. La tourmaline dans la tourmalinite s'est développée à une température constante de 350˚C, suivie d'une histoire métamorphique prograde de 500 à environ 600˚C. La température et la composition de la croissance initiale indiquent une formation par introduction externe de B. La composition de la tourmalinite est incompatible avec les protolithes connus riches en B et la modélisation thermodynamique montre que ses roches hôtes n'ont pas pu être le précurseur du métasomatisme B. La datation U-Pb au zircon donne un âge de protolithe de 3,7 Ga pour les méta-pélites et un âge métamorphique de 3,6 Ga pour la tourmalinite, ce qui est cohérent avec la géochronologie antérieure.

La tourmaline dans la partie nord de la ceinture d'Isua a une histoire de formation complexe et s'est formée en réponse à au moins trois événements : un métasomatisme B précoce entre 3,7 et 3,6 Ga, peut-être lié au magmatisme felsique ; une croissance pendant la libération progressive de B en système fermé pendant le métamorphisme prograde autour de 3,6 Ga ; et un autre événement de métasomatisme B à 1,7 Ga. Par conséquent, les roches riches en tourmaline d'Isua ne peuvent pas être utilisées pour déduire la présence

de sédiments riches en B à l'Éoarchéen ni pour recalculer les compositions de l'eau de mer à l'Archéen. Seule la tourmaline disséminée dans la métapélite s'est formée dans des conditions de métamorphisme en système fermé et a le potentiel de conserver des informations sur le B dans le protolithe.

Preface/Author contributions:

The sample preparation, analytical work, data reduction/analysis, and writing of this manuscript took place from August 2021 until August 2024 at McGill University in Montreal, Canada. The conception of the ideas was done as a collaboration by Dominic D'Amato and Dr. Vincent van Hinsberg. All samples used were provided by Dr. Peter Appel and Dr. Stephen Moorbath and without these contributions the work would not have been possible due to the scarcity of accessible samples from the field site. Specific author contributions are listed below.

The analytical lab work was conducted at McGill University, UQAM, University of Laval, and University of Ottawa.

Dominic D'Amato: Sample preparation, analytical lab work (microscopy, EPMA, SEM, ICPMS), writing of the body of the manuscript.

Vincent van Hinsberg: Assistance with writing of manuscript, assistance with generation of graphs and figures, assistance with data analysis of EPMA data.

Jillian Kendrick: Assistance with data reduction and analysis of geochronology data.

Comments on the manuscript were provided by Dr. Darrell Henry of LSU.

1. Introduction

1.1 Boron on the early Earth and its role in stabilizing life

The "search for life" is a major ongoing topic of research in the scientific community. Understanding the fundamental question of where we come from has long been a driver of scientific inquiry, and as we have advanced as a society this has only been amplified. The conditions needed for life to stabilize on the early Earth could have been present in a variety of geologic environments including water-rock interaction such as at black smokers (hydrothermal vents) promoted by steep energy and compositional gradients (Georgieva et al. 2021), on the surface of minerals including borates and sulfides that act as a template for complex organic structures (Hazen and Ausubel, 2016), in restricted basins that may develop enrichments in elements that promote organic synthesis, and more.

Particular focus has recently been directed to the behaviour and concentrations of boron (B) in the Archean surface environment. It has been shown that B in solution stabilizes and catalyzes prebiotic molecules (including ribose and pentose needed for RNA) by forming protective complexes. The variety of geologic environments allows for different stabilization pathways for ribose. This includes both borate mediated stabilization of ribose (Mishima et al. 2016, Ricardo et al, 2004), and the silicate mediated formose reaction (Vázquez-Mayagoitia et al, 2011). Without the assistance of minerals (borates or silicates) in the stabilization of ribose, the reaction will run to completion and the final product will be a brown tar (Mishima et al. 2016) which is subsequently unreactive. When borate (in the form of water-soluble B-minerals such as colemanite) is added to the solution it acts as a protective group forming a complex with other simple probiotic molecules (glyceraldehyde enantiomers). The complexation allows for the exposed aldehyde functional group to further react with simple alkenes (glycolaldehyde) as opposed to forming a polymer and turning into a tar. This disassociates and reacts with additional B in solution to form a stable cyclic pentose compound (Mishima et al. 2016). The B thus allows inorganically formed molecules to persist long enough to further react to more complex molecules, and potentially to the self-replicating structures of earliest life. This mediating potential of B depends strongly on its concentration and form (e.g. trigonally or tetrahedrally coordinated). We have a good understanding of modern boron cycling and its concentrations in the crust (2-36ppm), seawater (4.52ppm), mantle (0.1-0.5ppm), oceanic sediments and altered basalts (10-200ppm) (Marschall, 2017), island arc basalts (1-90ppm), MORB/OIB (0.28-3ppm) (Mohan et al. 2008), however boron cycling in the Archean is not fully understood. It is therefore unclear whether B would be present in sufficient quantity and in the right coordination (tetrahedral) and the right location to perform this stabilizing role.

Preserved fluid samples from the earliest history of the Earth are very rare and we are therefore forced to use the geological rock record to derive information on B in the surface environment. Tourmaline is the mineral commonly used as it is the most common borosilicate in the Earth's crust, it lacks internal diffusion below 650°C, it is refractory, resistant to alteration, has a wide stability field promoting growth in a variety of environments, and is an effective tracer of fluid evolution (Henry and Dutrow 1996; van Hinsberg et al. 2011). Tourmaline has been reported from most Archean supracrustal belts, including the Eoarchean Isua belt in Greenland, which shows evidence for many of the environmental features and prerequisite conditions thought to be necessary for early life on Earth.

1.2 Tourmaline

Tourmaline supergroup minerals are the most common and widespread borosilicate mineral in the Earth's crust (Henry and Dutrow 1996, van Hinsberg et al. 2011, Bosi 2018). In the following text the tourmaline mineral supergroup will be referred to as "tourmaline" and we will restrict ourselves to schorl- to dravite-dominated compositions as the samples discussed in this study are all restricted to these tourmaline species.

Tourmaline has been of interest to the scientific community for hundreds of years and was first noted for its electrical properties (pyroelectricity and piezoelectricity). These polar non-equivalent electrical properties of tourmaline were observed when the tourmalines were both heated (pyroelectricity) and subject to stress (piezoelectricity) (Fox and Fink, 1934, Henry and Dutrow, 2018). More recent work has focused on using tourmaline as a petrogenetic indicator of pressure, temperature, and composition of its growth environment using its elemental and isotopic composition (van Hinsberg et al. 2011).

The general formula and site occupancies for tourmaline are as follows: $XY_3Z_6T_6O_{18}(BO_3)_3V_3W$; where X = Na, Ca, K, []; Y = Fe^{2+}, Fe^{3+}, Mg, Mn, V, Cr, Ti, Li, Al; Z = Al, Fe^{2+}, Fe^{3+}, Mg, V, Cr; T = Si, Al, B; O = O; B = B; V = O, OH; W = O, OH, F (Hawthorne and Henry 1999, Bosi, 2018). Within this variety in compositions there are two main series; the schorl-dravite series (Fe-Mg-Al) and the schorl-elbaite series (Fe-Li-Al). The X-site occupants for the purpose of this study are Na, Ca, and [], with negligible K. Aluminum can reside at a variety of sites within the tourmalines structure (Z, Y and T), however it will first occupy the Z site, followed by excess Al residing in the Y and T sites. Alternatively, Fe and Mg preferentially incorporate into the Y site before the excess is distributed to the Z site (Bosi 2018). We will not consider the schorl-elbaite series here, because it does not occur in the samples studied.

Tourmaline is found in a variety of geologic environments ranging from granitic pegmatites to ore-forming systems to salt domes, and its presence mainly depends on the availability of B (Henry and Dutrow 1996, Henry et al. 1999). As tourmaline is dependent on B there must be a proximal B source for tourmaline to form in the different geologic environments. In pelites, two of the common and important B reservoirs are clays (smectite to illite transition releases 100-2,000 ppm B) and micas (breakdown of biotite and muscovite to K-feldspar). During progressive metamorphism, these phases break down releasing B and forming phases with lower B. Under closed system conditions, this B is generally redistributed to tourmaline. Additionally, hydrothermal fluids, for example associated with magmatic bodies, can also be enriched in B and are commonly associated with B-metasomatism and tourmalinisation of host rocks (Henry and Dutrow 1996). Once B is incorporated into tourmaline, it is generally immobilized as tourmaline is a refractory phase with large P-T stability and which is stable in acidic fluids (van Hinsberg et al. 2011) and resistant to alteration during transport and changing geologic conditions (alteration of tourmaline to clays in Li pegmatites has been noted but tends to be localized as opposed to a widespread phenomenon (Jahns and Wright 1951, Čopjaková et al. 2020)).

Tourmaline has a wide stability field from low temperatures and pressures (as low as 150˚C nucleation temperature and <1kbar) to high-grade conditions (approaching 1000˚C in high pressure environments at >10kbar) (van Hinsberg et al. 2011). Experiments have demonstrated stability up to 50kbar pressure for certain compositions. In metamorphic rocks, tourmaline typically appears at 350°C and disappears during melting, or where alkalic fluids develop leading to B partitioning into the fluid phase (van Hinsberg and Schumacher 2011).

Tourmaline has very slow diffusion and is resistant to re-equilibration resulting in the formation of compositional zoning as growth and sector zones. Sector zoning forms from the non-symmetrical nature of the structure along the c-axis. This asymmetry is due to the orientation of the SiO_4 tetrahedra in tourmaline which have their apices all pointing towards the -c axis and their base pointing towards the +c axis. This leads to a partial negative charge on surfaces growing in the +c direction (basal plane of tetrahedra) and a partial positive charge on the -c axis (apex of tetrahedra) using the axis direction nomenclature of Burt et al. (1989). At low temperatures, this charge difference is the greatest, with surfaces in one growth direction having a partial positive change and in the other having a partial negative charge. In addition to these partial charges the two growth directions also have different bonds exposed at the growth surface. These differences in charge and growth surface morphology lead to different elements being preferentially incorporated. Surfaces grown in the +c axis direction will be Ti and Ca deficient and will have increased Al and [] at the X site, whereas those grown in the -c axis direction will have higher Ti, Ca, and other highly charged cations. As the temperature of the system increases the degree of fractionation among sectors will decrease until the growth in the different directions reaches a common composition. This convergence of the partition coefficient typically occurs around 650°C. If the system stays below about 650°C, this intersector partitioning can be used as a single crystal thermometer (van Hinsberg and Schumacher 2007). Growth in directions perpendicular to the c-axis is not subjected to these partial charge effects and is not sector zoned. This a-sector composition can therefore be used as a reference composition (van Hinsberg and Schumacher 2007).

Due to its refractory mechanical nature, tourmaline can withstand transport without undergoing significant alteration or weathering, allowing for subsequent tourmaline growth on preexisting cores given a conducive geochemical environment. The additional growth on preexisting cores commonly occurs on the R faces and the composition of the overgrowths shows a strong dependence on growth direction and temperature in the same way that sector zoning does (Henry and Dutrow 1996; Sperlich et al. 1996; van Hinsberg and Schumacher 2007). It has been noted that the fibrous overgrowths seen at diagenetic conditions are equivalent to the sector zones formed at low temperatures. This indicates that a common mechanism is controlling both types of growth. Since the same mechanism is governing both features, fibrous overgrowths can be analyzed in the same way that sector zones are and can help determine the temperatures associated with secondary growth events (Henry and Dutrow 1996).

As previously noted, tourmaline cannot form without B. This is a fundamental aspect of tourmaline and research in the search for the origin of life has brought B into the spotlight. It had been speculated that early Earth surface environments did not have the B contents needed to stabilize organic molecules through complexation with borate, in part because the early geologic record lacks evidence for borate minerals such as those found in current evaporite sediments (Grew et al. 2017). Tourmaline is however ubiquitous in the Archean, indicating that B was present in the crust in a wide variety of settings, and tourmaline-rich lithologies including the tourmalinites of the Isua belt (Appel 1984, Appel and Chaussidon 1997, Grew et al 2017) show moreover that B was locally highly enriched. It is represented in a variety of environments owing its origins to many different processes. Some of the common expressions of tourmaline in the Archean are hydrothermally formed tourmaline which form from the introduction of external fluids to a B deficient protolith, the formation of tourmaline-rich rocks from B-rich protoliths (stratiform tourmalinites), and the typical expression of tourmalines in metamorphic environments where B can be both internally and externally derived. Since tourmaline has become recognized as an excellent indicator mineral it is commonly used to look at the evolution of B in the crust. The growth zones record the changes associated with the geochemical environment (including the introduction of external fluids), and the sector zones record the thermal history due to the distribution of Ca and Ti among the +c, -c, and a-sectors.

Previously, tourmalines from the Isua Belt have been used to directly back-calculate the B-isotopic composition of Archean seawater and make inferences on B in Archean surface environments. This was based on the interpretation that these tourmalines formed from marine sediments (Chaussidon and Appel 1997, Grew et al. 2015). This interpretation came from the light isotopic signature of ^{10}B relative to ^{11}B and the assumption that the isotopic signature of tourmalines was a direct proxy for that of Archean seawater. Originally, Chaussidon did a reconnaissance study of B isotopes of many tourmalines from around the world and found that a single grain from the tourmaline-rich lithology of Appel (1984) had a light isotopic composition that was then ascribed to being formed from a seawater-derived fluid. This study was subsequently elaborated upon by Grew et al. (2015) who reached a similar conclusion, although they took into account the intermediate fractionation steps during diagenesis prior to tourmaline formation. Still, they followed the assumption from earlier studies that the tourmaline-rich lithologies are B-rich meta-sedimentary protoliths. However, to concentrate B in Archean seawater to levels that would be needed to form the tourmaline schists we see at Isua would require upwards of ~99.8 percent evaporation of seawater if B contents were similar to those found in present-day seawater. This would cause isotopic fractionation of ^{10}B and ^{11}B and make this fluid a poor proxy of the original seawater. Moreover, earlier studies performed no detailed petrogenetic analysis, despite tourmaline commonly recording complex and prolonged growth histories and being characterized by growth and sector zoning. Sector zoning fractionates the B-isotopes (van Hinsberg and Marschall 2007) leading to differences within a single crystal, which is not due to bulk rock or fluid compositions. This crystallographically controlled distribution can skew the isotopic ratios. To get a representative B isotopic composition one must analyse the a-sector of the grain or correct c-sector compositions to the equivalent a-sector. Growth zoning shows even larger variations in B-isotopic composition (van Hinsberg and Marschall 2007, Bebout and Nakamura 2003) and analyses must thus take the zoning into account, with bulk analyses of zoned grains largely meaningless. Lastly, individual grains may record both internal redistribution of B and external B introduction, where the latter cannot be used to infer the behaviour of B in the protolith. For these reasons, the previous studies on Isua tourmalines can be questioned and hence the validity of using these elemental and isotopic compositions of these tourmalines as proxies for their formation fluids.

1.3 Isua Greenstone Belt geologic background

The Isua Greenstone Belt (IGB), in Greenland, is one of the best preserved Eoarchean terranes and has been studied since its discovery in 1966. It was discovered by J. Kurki and L. Keto due to magnetic anomalies stemming from the banded iron formations present in the IGB (Keto and Kurki 1966, Rosing 2014). The IGB is a bow shaped granitoid-greenstone belt (Fig. 1) located about 150km north of the capital, Nuuk. The Isua Belt is a part of the Itsaq Gneiss Complex in the North Atlantic Craton. It is 35 km wide from the western to eastern limb (Nutman et al. 2017, Grew et al. 2015). The IGB contains a variety of lithologies that are representative of Archean greenstone belts (Fig. 1), most of which have been metamorphosed at greenschist- to amphibolite-facies conditions. These are generally referred to as supracrustal lithologies as they were originally formed near or deposited at the surface of the Earth. The lithologies include deformed and undeformed pillow basalts, metapelitic schists, metavolcanics, chemical sedimentary rocks (chert, BIFs, and carbonates), ultramafic lenses (dunites), primary sedimentary rocks (volcanogenic and sedimentary), amphibolites (tholeiitic), and a unit coined the "dividing sedimentary unit" (DSU) (Moorbath et al. 1973, Fedo, 2000, Myers, 2001, Szilas et al. 2015, Nutman et al. 2015, Nutman et al. 2020). The belt is flanked to the north and south by TTG suites (tonalite-trondhjemite-granodiorite) dated at 3.8 Ga (south terrane) and 3.7 Ga (north terrane) (Moorbath et al 1973, Frie et al. 1999, Nutman et al. 1997). These ages are based on whole-rock Sm–Nd and Rb–Sr (Moorbath et al, 1973) as well as U–Pb analysis of zircon grains (Nutman et al. 1997). Felsic volcanism has been dated at 3.71 Ga and tonalitic sheets crosscutting ultramafic units have been dated at 3.79 Ga. The flanking tonalitic terranes contain a high quantity of undeformed doleritic dykes which were introduced after the formation of the IGB at ~3.5 Ga (Fedo et al. 2001). These undeformed dykes are related to deformed dykes in the south which shows that regional deformation was more protracted in southern terranes than those in the north, and that the deformation seen at the IGB had concluded by 3.5 Ga.

The tectonic history of the IGB has been debated since its discovery with contrasting interpretations based on the same geochemical, structural, and geophysical data. There are three main models invoked to explain the formation of the belt:

1. Northward convergent under-thrusting of 3.8 Ga TTG and DSU beneath 3.7 Ga TTG (Nutman and Friend, 2009) – This model is based on detailed mapping and extensive field work, which led to the production of the 1:20,000 geologic map (Nutman and Friend 2009). The addition of new zircon data led to the determination that there are unrelated packages of rock of different age that were juxtaposed against each other, leading to the interpretation that the IGB represents a tectonic break that allowed the collision of the 3.7 and 3.8 Ga tonalitic terranes. The collision led to the formation of orthogneisses from the tonalites. The DSU is interpreted to be the decollement for this tectonic activity. Nutman and Friend

interpret the available zircon data from the 3.7 and 3.8 Ga terranes as being crustal additions (high εNd values) as opposed to being remnants of previously formed crust being reworked, and that the belt represents the tectonic break between these two terranes. Nutman and Friend propose that the DSU was deposited as marine sediments on the 3.8 Ga southern terrane as the 3.7 Ga northern terrane was being formed as a primitive arc assemblage (Nutman and Friend 2009). These two terranes, along with the DSU, were then juxtaposed against each other between 3.69 and 3.66 Ga. This collision of the tonalitic terranes resulted in extension of the crust leading to intrusive ultramafic to granitic dykes (Inaluk Dykes; Nutman and Friend 2009). Finally, shearing of the belt led to the intrusion of granitic and pegmatitic dykes. After this collision and shearing, there were additional metamorphic and hydrothermal episodes that affected both the northern and southern terranes, specifically a 3.61 Ga metamorphic event that has been dated by U–Pb on titanite grains in the southern terrane (Crowley 2003), as well as metamorphic rims on zircon dated at 3.64–3.62 Ga (Crowley 2003). These reinterpretations and addition of new U–Pb data has led Friend and Nutman to conclude that there was a broadly modern tectonic regime acting at the IGB leading to the collision and accretion of two unrelated crustal packages (N and S terranes) along a tectonic break coined the DSU which led to mylonitization along the contact and the subsequent formation of the IGB from both marine sediments and weathered crustal, volcanic, and igneous components.

2. Southward convergent accretionary prism (Arai et al. 2015, Chemenda et al. 1995, Hanmer and Greene, 2001) – Southwestward convergence reminiscent of the style of orogeny in the present-day Pacific. This proposed regime is based on large scale observations including the increasing metamorphic grade in the NE part of the IGB, the interpretation of lithologies as an accretionary complex, and the presence of flanking granitoid terranes. This model focuses on the NE part of the belt. The authors note increasing grades across this part of the belt from NE to SW that went from greenschist to amphibolite facies from mineral parageneses, and 380˚C to 560˚C based on garnet-biotite thermometry (Aria et al. 2015). This is similar to early estimates of peak conditions e.g., 5 kbar and 550˚C (Boak and Dymek 1982) to 7 kbar and

620˚C (Komiya et al. 2002). Based on this data, they propose that the 3.7 Ga terrane was subducted beneath the 3.8 Ga terrane, i.e, the opposite to Nutman and Friend (2009). This subduction formed an accretionary complex along the suture zone followed by a collision of the two terranes, leading to the subducted oceanic lithosphere to break off and change the angle of the collision. This slab breakoff led to the exhumation of the accretionary prism which makes up the IGB in this model.

3. Vertical-tectonic processes (Webb et al. 2021) – The non-plate tectonic model of Isua is based on reinterpretation of existing geochemical, geochronological, and structural data as well as new data. Webb et al. (2021) disagree with the interpretation of the lithological sequence as an ophiolite, especially due to the geochemical nature of the dunite lenses found within the unit. They also disagree with interpreting the geochemical signature as an arc magmatic setting based on the likely different nature of mantle and lithospheric processes in the Archean which should lead to different geochemical signatures. They also present new observations contradicting the metamorphic gradient proposed by Aria et al. (2015) as they note the presence of garnets in the far NE part of the belt. They interpret the apparent metamorphic gradient as due to pervasive retrogression, and not regional metamorphism leading to the formation of discrete isograds. Their model proposes the rapid formation of a 3.8 Ga supracrustal body leading to overloading of the crust and melting. This melting led to the formation of TTGs within the newly formed terrane. This process was then repeated and a large shear zone was developed, leading to intense and uniform metamorphism across the belt at amphibolite facies. This strain and metamorphism created folds at multiple scales, and the Isua Belt represents the largest exposed a-type fold on Earth in this model.

The nature of specific lithologies often has direct implications regarding the inferred geodynamic setting of the IGB, or evidence for the presence of life, and these are therefore strongly debated. There is disagreement about the nature of dunite lenses in the NW part of the IGB. Some groups consider them to be mantle residue, indicative of an ophiolitic package (Furnes et al. 2007) whereas other groups consider them to be an ultramafic cumulate and therefore not representative of any mantle components (Waterton et al. 2021). Nutman et al. (2016) have argued for primary biogenic structures (stromatolites) in the low strain zones at IGB, thus signalling the emergence of complex life in the Eoarchean. However, it has been noted that the structures lack the internal banding commonly seen in stromatolites, and that this could be representative of a boudin rather than a biogenically formed structure. Additionally, there are no features to determine the proper orientation of these structures (Zawaski et al. 2020).

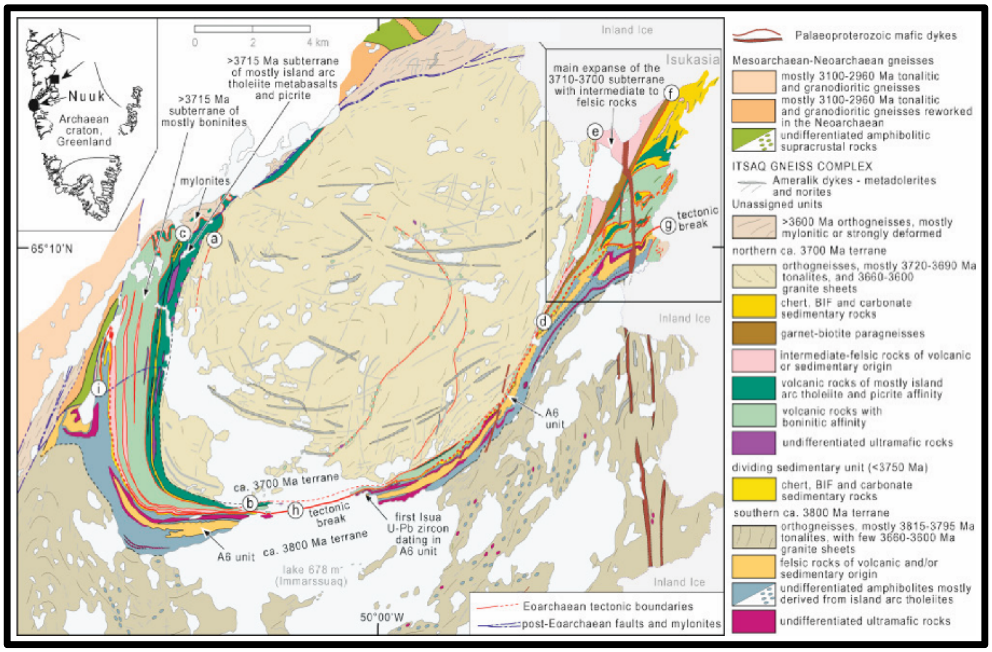

Figure 1: 1:20000 geologic map of the Isua Belt and flanking tonalitic bodies edited from Nutman and Friend (2009).

Tourmaline has been recognized as an accessory phase in many of the rock types present at the IGB, and locally as a major constituent. A distinct tourmaline-rich lithology has been identified and interpreted as a B-rich exhalative sediment (Appel and Chaussidon 1997, Grew et al. 2015). This lithology has been used to argue for local B-rich environments in the Eoarchean that could have stabilized prebiotic molecules and enabled life. Appel (1984) notes three environments that tourmaline was initially recognized at Isua. These were in impure carbonates, conglomerates, and a “tourmaline rich inclusion” (Appel 1984). Since then, tourmaline has been recognized in several additional rock types at Isua including metachert, schists, and amphibolites (including the garbenschiefer unit) (Grew et al., 2015). The tourmaline expresses itself differently depending on the rock type and it ranges from an accessory phase of <1% abundance to a major phase constituting up to 50% of the rock in tourmaline-rich horizons that are interpreted to be concordant and referred to as tourmalinite in the literature. A peculiar occurrence of tourmaline has a controversial origin with about 50% tourmaline present. This “inclusion” is discordant with the surrounding schists and compositionally distinct. Two interpretations of this inclusion with the first being a dismembered and redistributed vein (Nutman et al., 2000), and the second being an inherited boulder from a pre-Isua source (Appel, 1984, see Figure 2 for image). Both explanations are viable, and relating the growth histories of the tourmalines in the boulder to those in the belt will be important for differentiating between these. Tourmalines from the IGB have not been studied in great depth, and the past studies have focused on the isotopic and major element compositions (Appel 1984, Appel 1995, Chaussidon and Appel 1997, Grew et al. 2015,), aimed particularly at calculating the B isotopic composition in Archean seawater. The assumptions of an exhalative sedimentary origin for the tourmaline-rich rocks and a seawater source for B in the IGB have yet to be rigorously tested.

Figure 2: Image of tourmalinite in-situ modified from Appel (1984)

The origin and growth history of the tourmaline in the IGB must be determined before the significance of these rocks to early Earth B cycling can be known. To provide this crucial context, we have taken a comprehensive approach to investigating the petrogenesis of tourmaline-bearing rocks in the IGB. A detailed petrographic analysis of 3 tourmaline-bearing rock types from the NE part of the Isua Belt was conducted to determine the relationships between all the phases present and the formation history of the tourmaline. The petrographic analysis identified sector zoned grains on which we performed intersector thermometry to derive the thermal histories of the tourmalines from the different rock types and determine what events were recorded by these grains. A geochronological analysis permitted constraining the timing of B introduction and tourmaline formation, and distinguishing if a single or multiple tourmaline forming events led to the formation of compositionally distinct tourmaline based on the bulk rock compositions that the fluid interacted with. This provides the critical background needed to properly interpret the results from earlier studies and determine to what extent these tourmalines can be used as proxies for the early Earth's surface environments, in particular in terms of the presence and abundance of prebiotic molecule stabilizing B.

2. Methods

2.1 Samples

This study is based on a set of samples from the eastern part of the ISB collected by Stephen Moorbath and Peter Appel from the 1980s to 2000 (sample locations in Figure 3). Sample 427823 is a chlorite-actinolite greyish greenschist hosting a block-boudinaged tourmaline-quartz-carbonate vein (Fig 4a). The tourmaline vein is blueish-black in colour, massive in appearance and fine-grained. It is at shallow angle to the foliation in the schist. A quartz vein encloses the tourmaline, but pinches and swells and is not continuous, and the tourmaline is in direct contact with the host schist in places (Fig 4b). Quartz and carbonate fill extensional fractures in the tourmaline vein. Minor, disseminated, black tourmaline grains are present in the enclosing greenschist. The sample is from the “garbenschiefer” unit, which is interpreted to represent the metamorphosed equivalents of mafic to intermediate extrusive and intrusive igneous rocks that formed at 3.72 Ga (Nutman et al. 2022).

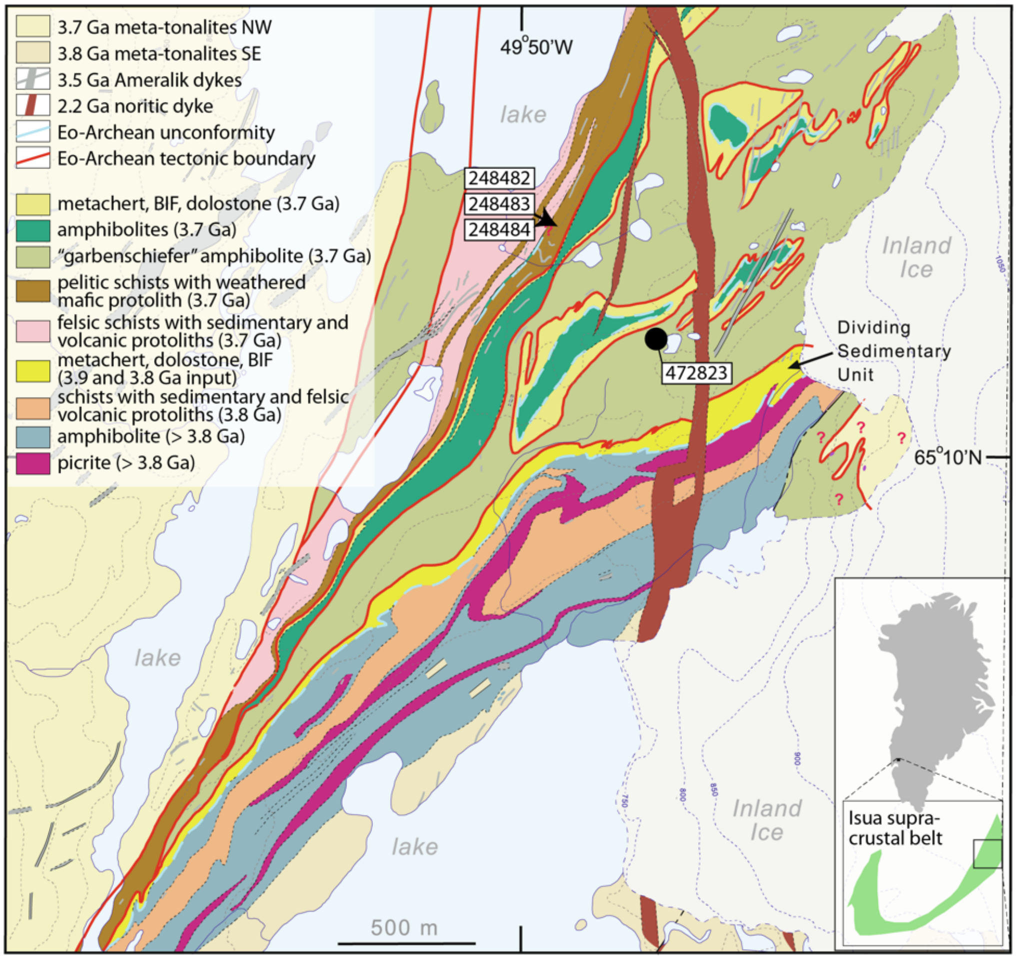

Figure 3. Geological overview map of the northeastern part of the Isua belt (modified after (Nutman et al. 2022) showing the locations of the samples used in this study. Coordinates for 472823 are known, but for the other samples, there is ambiguity regarding their exact location, although all are derived from the pelitic schist unit.

Samples 248484 K and M are meta-pelites sampled by coring from a *ca.* 400 m^2 aluminous lithology. The meta-pelites are interpreted to represent sediments derived from weathered mafic rocks, and have been dated to 3.71 Ga by zircon U-Pb chronology (Nutman et al. 1997, 2022) and 3.74 ± 0.05 Ga by Nd-Sm whole-rock chronology (Kamber et al. 1998). The meta-pelite lithology consists of variably deformed, banded garnet-biotite-plagioclase rocks ± quartz, muscovite, staurolite, epidote, and hornblende. Accessory zircon, tourmaline and apatite is common. Sample K is a well-foliated, dark grey micaschist with abundant garnets up to 5 mm in diameter. The foliation is defined by the micas (muscovite + biotite) and mm-thick, beige bands of quartz + plagioclase. The foliation wraps around the garnets. Sample M is a light-grey micaschist with large garnet augen up to 8 mm in diameter. The sample is muscovite-dominated with lenses of biotite + plagioclase. The foliation wraps around the garnets with tails of biotite, and shows crenulation and kink bands. There are minor bands of quartz + plagioclase with biotite rims, interpreted as incipient banding segregation. Sample M is heterogeneous on a mm-scale perpendicular to the foliation in both grainsize and mineral modes. This includes a layer with abundant black tourmaline on muscovite foliation surfaces. These tourmalines are up to 1 mm in length and idiomorphic. They are aligned to the foliation, but do not define a lineation. The 248484 A to M sample set has been extensively studied, including for its major and trace element bulk composition (McLennan 1981), for Nd-isotope signature and chronology (Moorbath et al. 1997; Kamber et al. 1998; Caro et al. 2003, 2006) and Pb-isotope signature (Kamber et al. 2003). These studies highlight that the samples preserve primary isotopic compositions, which are indicative of early crust segregation.

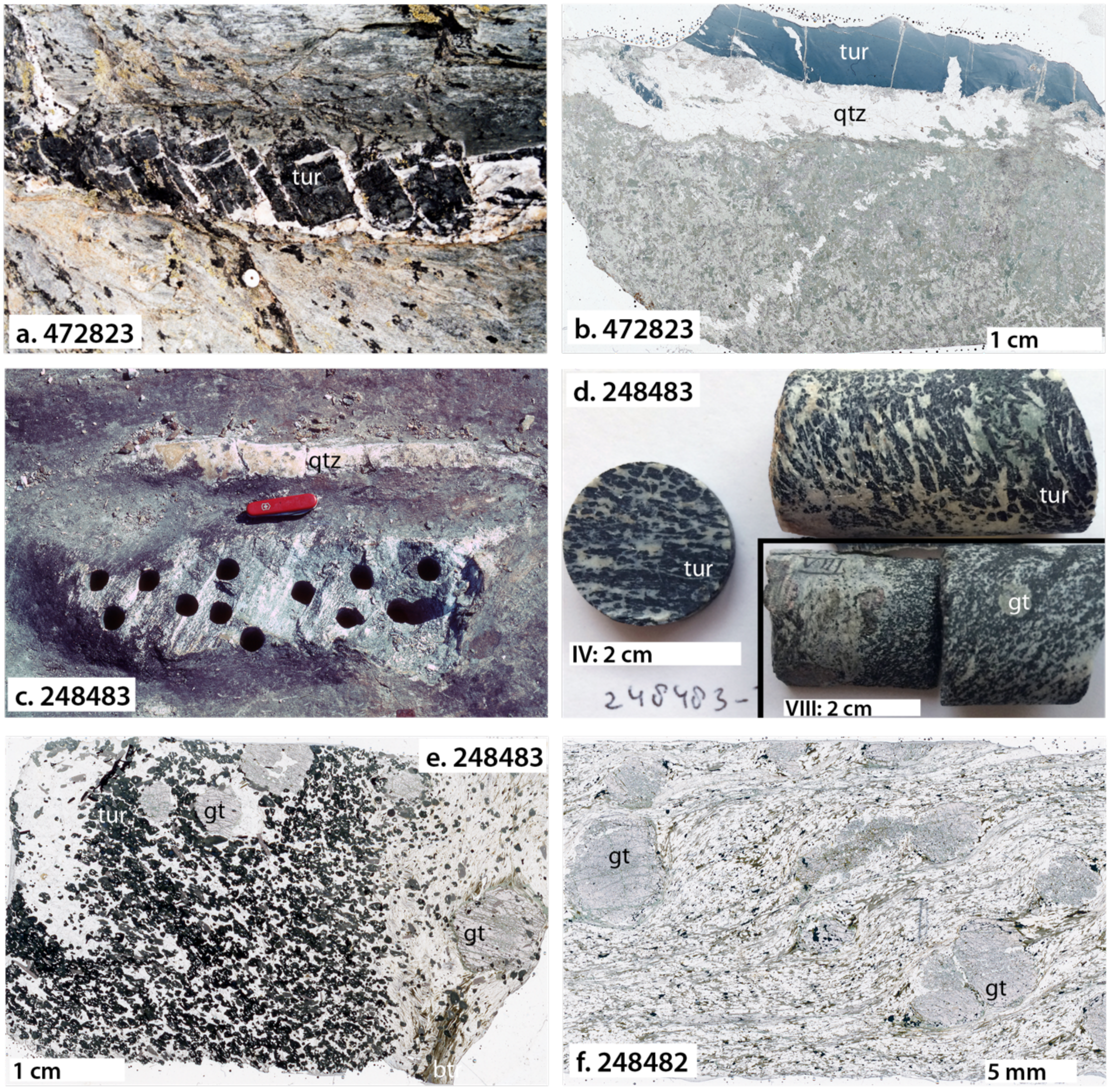

Figure 4. Field photograph of the greenschist-hosted boudinaged tourmaline vein with coin for scale; b. Thinsection scan (PPL) of the greenschist-hosted tourmaline vein showing the fibrous mass of blueish-green tourmaline at the top, mostly separated from the host greenschist by a quartz vein that contains clusters and isolated tourmaline grains; c,d. Photographs of the tourmalinite in the field and the core samples extracted from it, showing the tourmaline-defined banding; e. PPL thinsection scan of the tourmalinite and the host schist (on the right). Large garnets are present in both the tourmalinite and host schist that contain abundant tourmaline inclusions in their mantle growth zone; f. Thinsection scan (PPL) of the meta-pelitic schist lithology hosting the tourmalinite with similar, large, poikilitic garnets.

Sample 248483 is a tourmalinite within the meta-pelitic lithology (Appel 1984). It occurs as a 20 by 50 cm sized lens with a banding at high angle to the foliation in the enclosing micaschist (Fig. 4c,d). The banding is defined by alternating black tourmaline-dominated layers and white plagioclase-muscovite layers. Isolated garnet grains up to 7 mm in diameter are present in both the tourmaline and mica-dominated bands (Fig. 4d,e). The samples studied here are from 5 cores drilled into the lens (I – IV and VIII), and there is significant heterogeneity among and along cores, in particular in the tourmaline mode. Enclaves of host meta-pelite schist are present in multiple cores, and consist of well-foliated micaschist with isolated garnets and variable modes of small black tourmaline grains on mica surfaces. Tourmalines in the tourmalinite bands are mostly idiomorphic, elongate grains with a grainsize that varies among bands from mm-sized to grains of 1 cm length and 3 mm diameter. Tourmaline grains are aligned to the banding, and define a lineation, both at high angle to the foliation in the enclosing schist. Contacts with the host meta-pelitic schist, as well as schist enclaves are diffuse, with tourmaline mode and grainsize decreasing into the schist. Sample 248483 has previously been studied for protolith using textures, whole rock, and tourmaline compositions (Appel 1995), and for Pb and Nd isotopic signatures (Moorbath et al. 1997; Kamber et al. 1998, 2003), and is consistent in age with the host meta-pelite as determined by Nd-Sm whole-rock chronology (Kamber et al. 1998).

Sample 248482 is the meta-pelitic schist that is directly adjacent, and host to the 248483 tourmalinite. It is a competent, well-foliated, banded micaschist with dark bands of mica and lighter bands of quartz + plagioclase. Garnet occurs as 4-5 mm diameter augen, mostly in the quartz-plagioclase bands, but invariably with micas wrapping around the garnet and forming tails (Fig 4f). There is local isoclinal folding of the quartz-plagioclase bands. The schist is similar to schist fragments in the tourmalinite core samples, but only contains tourmaline as a minor accessory phase.

2.2 Petrography

Multiple thinsections from each sample, including a set of original thinsections supplied by Stephen Moorbath, were studied in reflected and transmitted light optical microscopy, and by back-scattered electron imaging on a PhenomXL desktop SEM. Phase identification was aided by an EDX spectrometer on the SEM.

2.3 EPMA

Major element compositions for tourmaline and associated minerals were determined by EPMA WDS analyses at the University of Ottawa (JEOL-JXA-8230 SuperProbe) and McGill University (Cameca SX-Five FE). Natural and synthetic mineral standards were used to calibrate the instruments, and secondary silicate standards were analysed to assess accuracy. Operating conditions were a 15 kV accelerating voltage, 20 nA current, and 10 and 2 μm beam diameter for the first and second analytical session, respectively, with K and Na analysed first to avoid alkali-loss. Garnet analyses were standardized on a separate set of standards including an almandine standard for Ca, Al, Fe, Mg and Si. Mineral analyses were normalized by their respective cations sum. Tourmaline analyses were normalised to cations on the Y, Z and T sites = 15. Distribution of cations over the Y and Z sites follows (Bosi 2018). Cation and anion sums were combined to calculate Fe^{2+} and Fe^{3+} contents of the oxides, assuming no vacancies in the X, Y, or T sites.

Element maps were obtained for select tourmaline grains to image their zoning. Data were collected on the McGill University Cameca EPMA and the Cameca SX-100 at Laval University, combining EDS and WDS data acquisition. Operating conditions for mapping at the University of Laval were 15 kV acceleration voltage and 100 nA beam current with 20 msec dwell time and a 1 μm pixel size, imaging Ca (PET), Ti (PET), Fe (LIF), Na (TAP), and Mn (EDS). At McGill University, the conditions were 15 kV and 100 mA with a variable pixel size from 0.5 to 1.0 μm. Element maps were edited in ImageJ to maximize contrast.

2.4 U-Pb geochronology

Tourmaline is a challenging mineral to date directly given its (strong) preference for the daughter isotope of most chronometers (*e.g.* Pb >> U, Sr >> Rb), or low abundance of the radioactive element including K and the REE (Marschall and Jiang 2011). We therefore date tourmaline formation indirectly here by dating the associated accessory phases zircon and apatite.

Selected zircon and apatite grains free of inclusions and fracture coatings were dated *in-situ* using laser ablation magnetic-sector HR-ICP-MS. Zircon grains were analysed in 30 µm thick polished thinsections, which permitted for zircon petrography, and in particular its relationships to the major minerals and tourmaline to be established. A total of 17 zircon spots was analyzed for the meta-pelite, and 23 for the tourmalinite. We attempted to analyse apatite directly in thinsection, but this was not successful because of problematic ablation and fracturing. They were therefore analysed in the polished offcut block of one of the thinsections that exposed both the vein and host schist. This permitted making use of the petrography on the thinsection and at the same time provided stable ablation and more material for analysis given that we could collect longer signals for these thicker apatite grains.

Analyses were conducted using a Photon Machines 193 nm laser ablation system with a two-volume ablation cell with the aerosols transferred in an ultrapure He flow to a Nu Attom HR-ICP-MS at the GEOTOP research centre at UQAM in Montreal, Canada. Three mL/min of N_2 was introduced to the gas flow prior to injection into the plasma. The Nu Attom mass spectrometer was operated in high-resolution mode and the isotopes that were analysed are ^{202}Pb ^{204}Pb, ^{206}Pb, ^{207}Pb, ^{208}Pb, ^{235}U, ^{238}U. A crater size of 20 µm was used for zircon analyses at a laser repetition rate of 10 Hz with a fluence of 4.5 J/cm^2 on sample, and data were collected for at least 30s. Zircon standard 91500 (Wiedenbeck et al., 1995) was used as the primary standard and OG1 (Stern et al. 2009) and Plešovice (Sláma et al., 2008) zircons as secondary references. Every 10 unknowns were bracketed by 3 analyses of 91500, 2 of

Plesovice, and 2 of OG1. NIST SRM 610 was also analyzed at the start and end of the run. The measured U/Th ratio of N610 is 1.05 and oxide formation was low at 0.08% $^{238}U^{16}O/^{238}U$ and 0.12% $^{232}Th^{16}O/^{232}Th$. The VizualAge module (Petrus and Kamber 2012) was used for processing the data in Iolite with a smoothed spline background subtraction and an exponential downhole correction scheme. Analyses of Plešovice zircon yielded a concordia age of 320.9 ± 1.2 Ma (MSWD = 0.56, n = 11) and OG1 analyses yielded a $^{207}Pb/^{206}Pb$ weighted mean age of 3450.1 ± 6.4 Ma (MSWD = 16, n = 10), relative to their accepted ages of 337.13 ± 0.37 Ma and 3465.4 ± 0.6 Ma, respectively. We note that OG1 is comparable to the age of zircons at Isua.

A total of 10 apatite grains was analysed, as well as vein tourmaline. The apatite grains are all > 50 µm in diameter, and BSE images show that they are unzoned and free of inclusions. The tourmaline represents an inclusion-free and unstrained domain of very fine-grained fibres (< 1 µm width) in the core of the vein. The tourmaline was analysed to provide an estimate of the common Pb composition of the tourmaline-forming fluid, given the negligible U content of tourmaline. A 50 µm crater size at 10 Hz repetition rate was used with a fluence of 4.54 J/cm^2, and data were collected for 30s. McClure Mountain syenite apatite (Schoene and Bowring, 2006) was used as the primary reference material and Durango and Fish Canyon Tuff apatites were analysed as secondary reference materials. Zircon 91500 and NIST 612 reference materials were also monitored. Every 7-8 unknowns were bracketed with 15 analyses of the primary and secondary reference materials. The U/Th ratio was 1.08 and oxide formation was 0.25% as determined on $^{238}U^{16}O/^{238}U$ and 0.53% for $^{232}Th^{16}O/^{232}Th$. Durango apatite yielded an age of 30.78 ± 0.47 (2SE) using a Stacey and Kramers (1975) common Pb regression, close to the accepted age at 31.44 ± 0.18 (McDowell et al., 2005). The analysed Fish Canyon Tuff apatite contained apparently very low concentrations of U and therefore a meaningful age could not be calculated. Data processing was done using the VizualAge UComPbine data reduction scheme (Chew et al., 2014) in Iolite 4 v.4.9.1 (Paton et al., 2011). An exponential fit was used for the downhole correction of the primary standard, with common Pb corrected based on ^{207}Pb using NIST 612 as a $^{207}Pb/^{206}Pb$ reference. Ages were calculated using IsoplotR online (Vermeesch, 2018).

2.5 Thermodynamic modelling

Metamorphism and boron-metasomatism were forward-modelled in thermodynamic calculations using the Perple_X suite of programs (Connolly and Petrini 2002; Connolly 2005). Bulk rock compositions were taken from (McLennan 1981; Appel 1984) for 248484 and 248483, respectively, and calculated for specific thinsections by combining thinsection mode estimates with EPMA data for the respective minerals in that sample. The 6.33 version of the Holland and Powell database (Holland and Powell 2011) was used for mineral end-members and combined with the mineral solid solution models biotite, chlorite, garnet, staurolite, cordierite, ilmenite, and muscovite from (White et al. 2014; White et al. 2014); plagioclase from Newton et al. (1981); K-feldspar from Haselton et al. (1983); and spinel from (White et al. 2002). Calculations were performed in the K-Na-Ca-Mg-Mn-Fe-Al-Si-O-H chemical system and fluid-saturated with a C-O-H fluid with $XCO_2 = 0.05$ (set arbitrarily). Metasomatism was modelled for a typical Archean crustal *P-T* gradient after (Lambert 1983).

3. Results

3.1 Sample petrography

Sample **427823** was investigated by optical and electron microscopy in 5 thinsections that cover the vein, the host, or the vein-host contact. The tourmaline vein consists of <10 µm fibres of blueish-green tourmaline. Grains are aligned and appear to “flow” with folds and kink-bands (Fig. 5a). The tourmalines have a larger grainsize at the vein rim of up to 20 µm and display zoning, with a light blue or green core of variable size, a darker-blue mantle, and a green rim (Fig. 5b). The cores are interpreted as sector zoning (cf. van Hinsberg et al. 2006). The tourmaline fibres are locally aligned to the vein contact, but more commonly, their orientation rotates almost 90˚ and they terminate perpendicular to the contact. Quartz, twinned plagioclase, carbonate, and idiomorphic epidote grains are present at the vein contact, interspersed with clusters or isolated grains of idiomorphic tourmaline. The vein border is followed by a 2-3 mm thick quartz vein with isolated chlorite grains, clusters of chlorite + epidote, and fragments of the host schist. The epidote grains have a core full of inclusions, mostly of epidote, with an idiomorphic, inclusion-free rim. Plagioclase is twinned and has inclusions of epidote and quartz.

The vein is locally pulled apart, resulting in extensional fractures perpendicular to the vein. These occur on several scales from 10s of μm thickness in thinsection, to mm-sized extensional fractures in hand specimen, and the bookshelf boudinaging observable in the outcrop photograph (Fig. 4a,b). There are at least two generations of these fractures. The older generation is lens-shaped and contains quartz and minor tourmaline. This tourmaline is fibrous and aligned to the fibres in the vein itself. Tourmaline fibres may, moreover, cut the fracture surface. The quartz is recrystallised and unstrained. Multi-stage fracturing is evidenced by bands of tourmaline. The textures suggest fracturing of a tourmaline fiber mush. The younger fractures contain amphibole, chlorite, plagioclase, epidote, carbonate, and opaques, and have tourmaline grains growing inward from the tourmaline vein fracture surfaces. In most cases, epidote is present on fracture surfaces, with amphibole, chlorite, plagioclase, and opaques in the interior, with chlorite and amphibole aligned parallel to the fracture. Fractures do not cut the host schist, and the fracture minerals appear to be in equilibrium with those of the host.

The host schist is weakly foliated with green to blueish-green amphibole, plagioclase, quartz, epidote, and idiomorphic laths of chlorite (Fig. 6). Amphibole grains have abundant, rounded quartz inclusions. Titanite and apatite are the dominant accessory phases, with titanite commonly displaying a rutile core. Tourmaline is present in the host as isolated, idiomorphic grains up to 100 μm in diameter. Their colour changes progressively from blueish-green near the vein to brown furthest away from the vein. These tourmaline grains are zoned, with a sector-zoning core that is either blueish-green or brown, a darker-green mantle, and a light-green outer rim. Apatite is a common accessory in the matrix and a size of up to 150μm, with size decreasing systematically with distance from the vein. All phases appear to be in equilibrium as evidenced from sharp, straight contacts and mutual inclusion relationships. Similar equilibrium relationships are present for the host and vein minerals at the vein-host contact, e.g. blueish-green tourmaline intergrown with plagioclase, epidote, and amphibole, suggesting that vein formation was at equivalent conditions.

Retrogression is present as albitization of plagioclase, mostly at rims, followed by pervasive sericitization, and local chloritization of amphibole (Fig. 5,6)

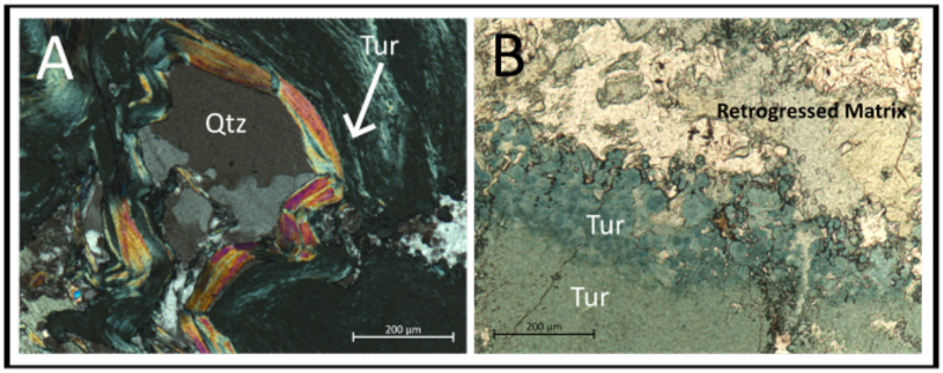

Figure 5: Micrographs of Sample 472823. A. XPL view of the tourmaline vein enclosing a fragment of schist. The tourmaline grains are fibres that appear to flow around the fragment with later development of kink bands in both the tourmaline and mica; B. PPL view of the edge of the tourmaline vein with larger, idiomorphic tourmaline grains intergrown with the matrix minerals showing color zoning with blue or darker green cores and olive-green rims. The matrix consists of plagioclase,

chlorite, epidote, quartz, disseminated tourmaline and minor carbonate, with sericite retrogression of the plagioclase.

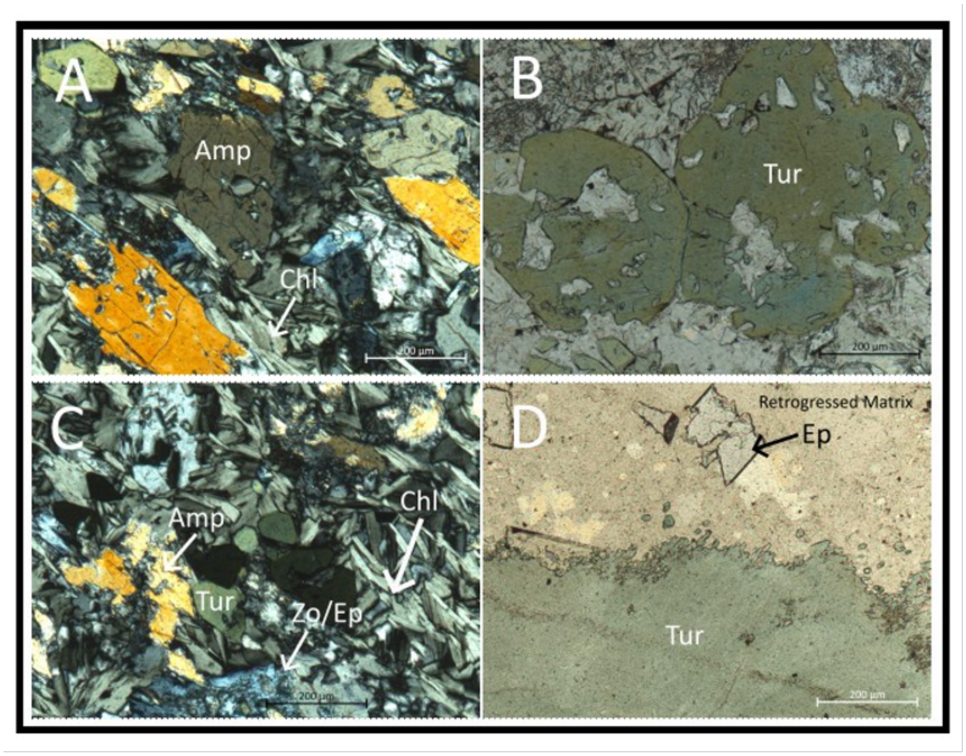

Figure 6: Micrographs of 472823 showing the typical occurrence of its constituent minerals. A,C. Greenschist host furthest away from the tourmaline vein with amphibole, plagioclase, chlorite, epidote and tourmaline; B. Large tourmaline grains distal to the vein with inclusions of quartz; D. Idiomorphic epidote together with sericitised plagioclase, with quartz inclusions, adjacent to the tourmaline vein.

Four thinsections were studied for sample **248484**, two of K and M each.

248484-M1 is a micaschist representative of sample M, whereas 248484-M2 represents a muscovite-rich layer with abundant tourmaline on the mica surfaces. The overall textures and mineralogy are identical, and differences are in mineral modes only. They are therefore described together.

The micas – intergrown muscovite and biotite – define a strong, crenulated foliation and enclose plagioclase, epidote, quartz, garnet, and opaques (Fig. 7). Plagioclase is twinned and has inclusions of quartz and epidote. Garnet is an order of magnitude larger than all other minerals and has inclusions of biotite, quartz, plagioclase, opaques, and tourmaline. The biotite is greenish-brown in colour, both in the matrix and as inclusions. The tourmaline grains are dark green in colour and have idiomorphic terminations. The largest grains display a concentric zoning with a variably sized dark green or light blue core, green mantle, and thin, lighter green rim. Grains sectioned parallel to the ***c***-axis display hourglass sector zoning (Fig. 7b). They contain inclusions of quartz and opaques. The peak mineral paragenesis is muscovite-biotite-garnet-epidote-plagioclase-quartz-opaque-tourmaline.

Biotite and garnet are retrogressed to chlorite, with local strong retrogression of garnet (Fig. 8b) resulting in clusters of randomly oriented chlorite with minor, irregular relicts of garnet and aligned grains of tourmaline and ilmenite (Fig. 8a). Epidote and calcite accompany the retrogression.

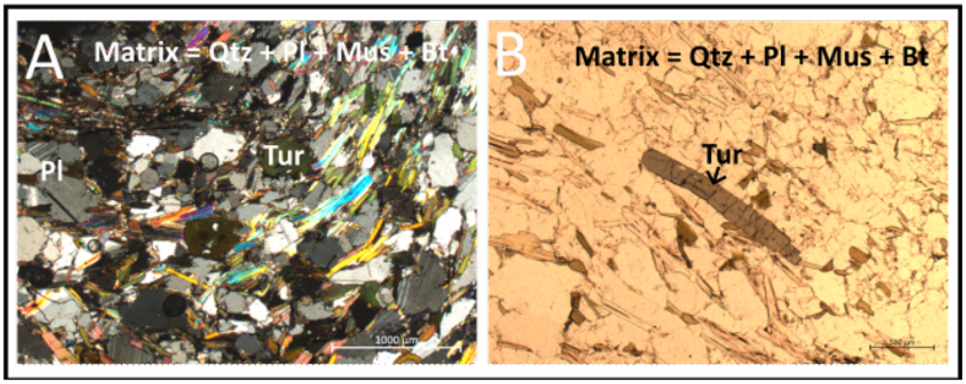

Figure 7: A. Representative XPL view of sample M1 showing the foliation-defining muscovite + biotite together with plagioclase, tourmaline and quartz; B. PPL view of large tourmaline grain parallel to the foliation with hourglass sector zoning. The grains has been pulled apart with fractures perpendicular to the c-axis.

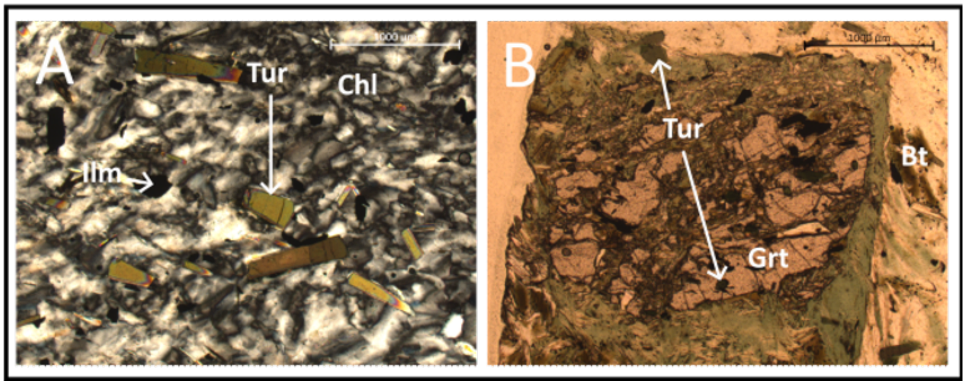

Figure 8: Photomicrographs of a retrogressed domain in sample M2. A. Randomly oriented chlorite grains replacing biotite with aligned tourmaline and ilmenite fully preserved; B. Angular relict of garnet + biotite heavily retrogressed by chlorite. The relict contains abundant idiomorphic tourmalines including as inclusions in the garnet (both core and rim).

248484-K is similar to sample M with mica bands that define a strong foliation enclosing bands and lenses of quartz, plagioclase, and garnet. The mica bands fold around the large, up to 8 mm diameter, garnets (Fig. 9a) with pressure shadows of biotite, plagioclase, and quartz. Blocky opaques (magnetite) are present dispersed in the matrix and as inclusions in quartz, plagioclase, and micas (Fig. 9b). Quartz is mostly unstrained and contains aligned inclusions. The garnets have a poikiloblastic core with abundant quartz inclusions and lesser, idiomorphic ilmenite (Fig. 9a). They have a mantle with less, but larger quartz inclusions together with ilmenite, magnetite, biotite, plagioclase, apatite, and tourmaline. Larger ilmenite inclusions have quartz, plagioclase, biotite, and apatite inclusions. The magnetite and ilmenite are locally in contact with a sharp, equilibrium boundary. The garnet rim has large inclusions of magnetite and ilmenite, again in equilibrium, with lesser biotite, tourmaline and plagioclase, and minor quartz. The rim has idiomorphic terminations and is intergrown with matrix biotite, magnetite, and plagioclase. The inclusions have a weak preferred orientation that is at an angle to the foliation in the host, indicating some rotation of the garnet grains. Epidote inclusions are locally present but replace plagioclase.

The biotite is green-brown in colour and locally contains zircons with a pronounced pleochroic halo in the host biotite. Some of the quartz-plagioclase bands contain idiomorphic epidote, in part intergrown with biotite. A second generation of epidote is observed associated with chlorite retrogression of garnet. Tourmaline occurs as a disseminated accessory phase in the mica bands and as inclusions in the poikiloblastic part of garnet. Tourmaline grains are aligned to the foliation, green to brown in colour and concentrically zoned (Fig. 9b). The zoning is consistent among grains, even those present as inclusions, with a core that is either light green or blue, a dark green-brown mantle, and a lighter green rim. The peak paragenesis for this sample is muscovite-biotite-garnet-epidote-plagioclase-quartz-opaque-tourmaline, i.e. the same as sample M.

The sample shows only minor retrogression, restricted to some chloritization of garnet and appearance of a second epidote generation.

Kyanite, staurolite and hornblende have been observed in the meta-pelite unit this sample is derived from but were not observed in the thinsections studied here.

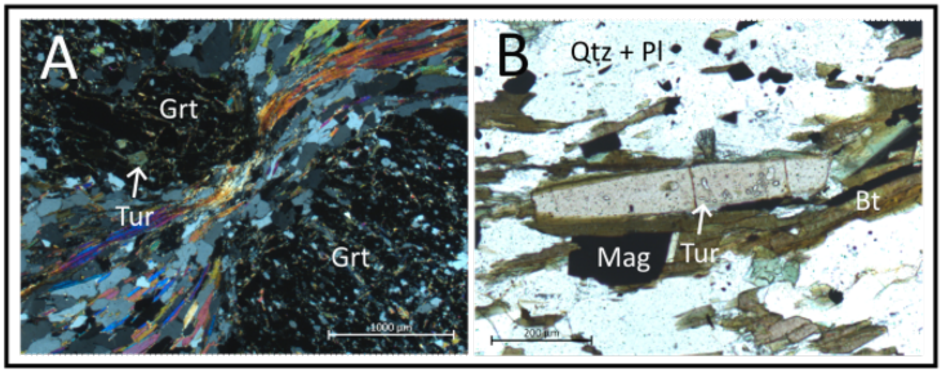

Figure 9: Representative micrographs from sample 248484K. A. XPL view of poikilitic garnets with inclusions of plagioclase, quartz, biotite and opaques. The micas fold around the garnet grains; B. elongate tourmaline grain aligned to the foliation in contact with biotite and magnetite.

Sample **248482** was studied in two thinsections. It is a micaschist, but has significantly less mica, especially muscovite, than sample 248484. The sample has a strong foliation defined by bands of quartz + plagioclase alternating with brown biotite and minor muscovite (Fig. 10b). Opaques are present as elongate grains in the mica bands, aligned to the foliation. One of the thinsections contains several large poikilitic garnets with idiomorphic outlines, as well as minor, idiomorphic staurolite grains (Fig. 10a). A rim of quartz grains is present on the garnets, and biotite folds around them. The garnets have randomly oriented inclusions of quartz, biotite, and opaques. Tourmaline occurs as small grains in the mica bands and is a minor accessory phase. It is dark green in colour. The peak paragenesis is muscovite-biotite-plagioclase-garnet-staurolite-quartz-opaque-tourmaline.

Epidote is present as small idiomorphic grains associated with chlorite retrogression of biotite and garnet, and plagioclase sericitization, and is interpreted to be retrograde.

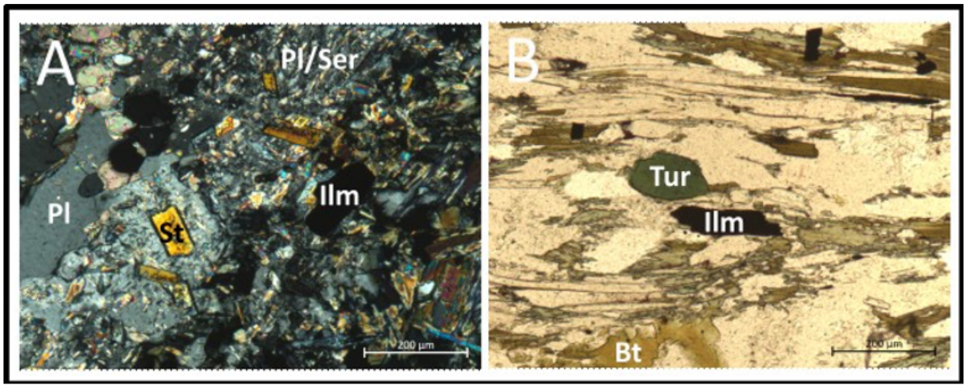

Figure 10 : Characteristic micrographs for sample 248482. A. XPL view of a rare staurolite grain in the sample, occurring with plagioclase (locally strongly sericitized), quartz, epidote and ilmenite; B. Typical matrix of the sample in PPL. The foliation is defined by biotite and lesser muscovite, with ilmenite and tourmaline aligned to the foliation. The colorless grains are plagioclase and quartz.

Four thinsection of sample **248483** were investigated, one each of core I and IV and two of core VIII. All display similar textures and minerals and vary mostly in mineral mode and in whether fragments of host schist are present. They are therefore described together.

The tourmalinite consists of alternating dark, tourmaline-dominated bands with interstitial plagioclase and muscovite, and light-coloured bands of plagioclase, muscovite, and minor quartz (Fig. 11b). Biotite and garnet are minor phases in both bands, but the garnet grains are large (up to 8 mm diameter). The core of the garnet is poikiloblastic and full of quartz inclusions (Fig. 12b), with lesser biotite, magnetite, and ilmenite, whereas tourmaline inclusions dominate the mantle, and minor ilmenite, quartz, and plagioclase inclusions the rim. Small apatite and zircon inclusions are present throughout. One garnet is intergrown with a large plagioclase grain that protrudes into the matrix, showing that plagioclase was in equilibrium with garnet throughout its growth. The garnet has idiomorphic terminations (Fig. 12b). Matrix biotite commonly shows replacement by muscovite. Plagioclase is twinned (Fig. 11b). The abundance of quartz inclusions in the garnet and tourmaline contrasts with the minor quartz mode in the matrix. However, the modes of the minerals vary perpendicular to the foliation, and there are also bands where muscovite is rare and quartz is the dominant phase both interstitial and in the light bands. Tourmaline grains are aligned and define a strong lineation that is parallel to the banding (Fig 4d, 11b). Inclusions within the tourmaline grains show this same preferred orientation. Grains are up to 1 cm in length. Pull apart fractures ⊥ to the long axis are common and have formed at multiple times with rim tourmaline growth present on some fracture surfaces, although for most, the fractures cut through the rim and no growth on the fracture surface is observed.

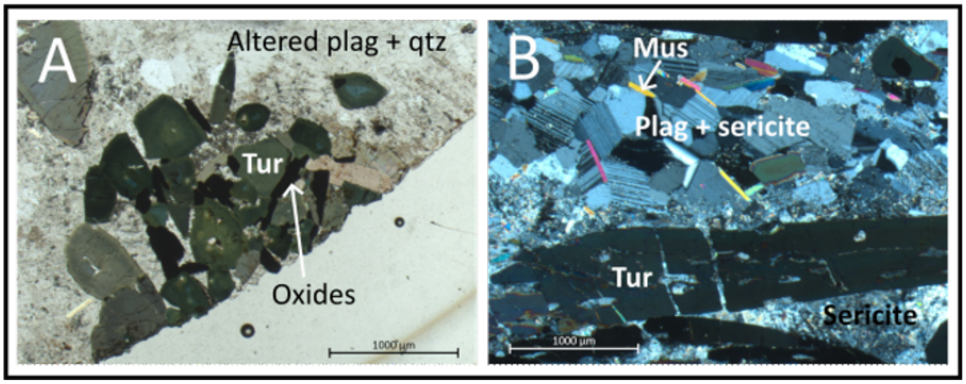

Figure 11: Micrographs of sample 248483-IV. A. PPL view of a cluster of concentrically zoned tourmaline grains intergrown with ilmenite in a matrix of mostly plagioclase with minor quartz and small epidote grains. B. XPL view of twinned plagioclase grains with minor sericitization in a light-colored plagioclase-muscovite band. A large, aligned tourmaline grains is part of the adjacent dark band and has interstitial sericitized plagioclase.

Tourmaline is green-brown in colour and concentrically zoned with variably sized dark green and light blue cores in ⊥ ***c*** cross-sections (Fig. 11a, 12). The inner mantle zone is dark green, followed by two light to darker green mantle zones, and finally a light green rim. Sections // ***c*** display hourglass sector zoning with light blue and dark green ***c***-sectors and a green ***a*** sector. This hourglass sector zoning appears as the variably sized and coloured cores in ⊥ ***c*** sections. The tourmalines have poikiloblastic cores with inclusions of quartz, tourmaline, opaques, and plagioclase (Fig. 12b). Some cores display irregular and laminar colour variations that may represent relict compositional variations inherited from the overgrown protolith minerals (see van Hinsberg et al. 2017).

The host schist is present as lenses and enclaves within the tourmalinite and core 248483-VIII appears to show the contact between the host micaschist and the tourmalinite (Fig. 4e). The micaschist in this sample has a strong, crenulated foliation defined by biotite, and lesser muscovite (Fig. 12a). The biotite grains have pronounced pleochroic haloes around accessory zircon inclusions. Plagioclase, garnet, opaques, and minor quartz are present in between the micas, with mica bands folding around the garnets and present in the pressure shadows. The garnet grains show identical textures and size to garnet in the tourmalinite with a poikiloblastic core with abundant quartz and ilmenite inclusions, a mantle with less, but larger inclusions of quartz, tourmaline, ilmenite, biotite and muscovite, and an idiomorphic rim that has minor inclusions of ilmenite. The inclusions are randomly oriented. Tourmaline is present as dispersed idiomorphic grains with identical zoning and inclusion assemblages and textures as grains in the tourmalinite (Fig. 12a). Overall tourmaline grainsize is smaller in the schist. The contact between schist and tourmalinite is diffuse, and minerals grow across the boundary. The foliation in the tourmalinite at the boundary is highly crenulated and, locally, this crenulated foliation terminates at high angle on the more regular foliation of the schist. However, within a few mm, the foliation instead rotates into that of the schist. We interpret the contact as a discordant boundary that was modified by later metamorphic mineral formation and growth, and deformation, and is hence early.

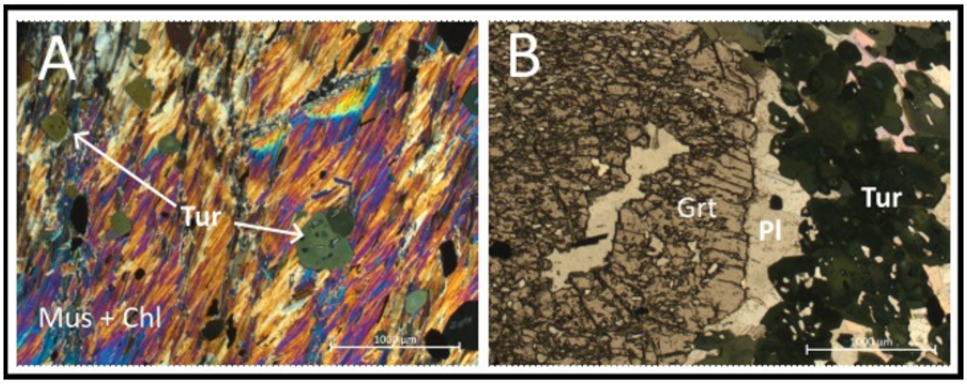

Figure 12: Micrographs of tourmalinite sample 248483-VIII (thinsection overview scan in Fig 4e). A. XPL view of a muscovite-biotite mica band in the host schist with disseminated, zoned tourmaline grains; B. PPL view of a large, poikilitic garnet grain in the tourmalinite with inclusions of quartz, plagioclase, opaques, biotite and tourmaline. The tourmaline around it is sector- and concentrically growth-zoned and has cores with abundant inclusions, mostly of quartz.

Lenses of micaschist within the tourmalinite are similar in appearance with a muscovite-dominated foliation, minor biotite, and garnet, plagioclase, quartz, and opaques in between the micas. Tourmaline is common and has identical zoning to the tourmaline grains in the enclosing tourmalinite, but grainsize is smaller.

The tourmaline is intergrown with biotite, muscovite and opaques, locally overgrows biotite, is aligned to the mica foliation, and has micas folding around grains, and has inclusions of all the matrix minerals. This indicates that tourmaline growth is syn-tectonic. The absence of tourmaline in the garnet cores suggest that tourmaline only appeared during garnet mantle growth. However, the tourmaline inclusions display the full zoning as observed in matrix tourmalines, and it would therefore appear that there was a hiatus in garnet growth. The garnet rims enclose pre-existing tourmalines and appear to post-date tourmaline growth, suggesting a sequence of garnet core → tourmaline core + mantle formation → garnet mantle + tourmaline rim → garnet rim. There are no disequilibrium textures between garnet rims and tourmaline. This indicates that the mineral assemblage is in equilibrium and represents a paragenesis of muscovite-biotite-tourmaline-garnet-plagioclase-quartz-opaques. This paragenesis is identical for the tourmalinite and host schist, although the mineral modes are different.

Retrogression of the sample is minor, except for some of the lenses of micaschist, and consists of chloritization of biotite and garnet along rims and fractures and sericitization of plagioclase with appearance of epidote. Brittle fractures cut across the sample at high angle to the foliation and banding and lead to closely spaced fractures in the garnet. The fractures are filled by a greenschist-facies assemblage of chlorite, epidote, quartz, and carbonate, and intense sericitization is observed where these cut plagioclase grains.

In the following, these samples will collectively be referred to as **greenschist-hosted tourmaline vein** (427823), **meta-pelite** (248482 and 248484) and **tourmalinite** (248483).

3.2 Mineral compositions

Representative mineral compositions as determined by EPMA are presented in Table 1, and the full set of analyses is provided in the supplementary Excel file. Tourmaline analyses are presented below for the ***a***-sector only, as this sector is not affected by sector-zoning preferential element uptake or exclusion and therefore allows for comparisons between samples and growth zones (see van Hinsberg et al. 2006). Compared to ***a***-sector compositions, ***c+*** sectors are characteristically depleted in Ca, Ti and ^{Z}Mg, and enriched in X-site vacancies and ^{Z}Al, whereas the inverse is true for the ***c-*** sector, in agreement with the systematics observed in other studies (e.g. van Hinsberg and Schumacher 2007, 2011; Berryman et al. 2017; van Hinsberg et al. 2017).

3.2.1 Greenschist-hosted tourmaline vein

Tourmaline has a composition intermediate between the dravite, schorl, uvite, and foitite endmembers (Ca enriched dravite) with a median mineral formula of $(Na_{0.57}Ca_{0.25}Vac_{0.17})_X$ $(Al_1Mg_{1.2}Fe_{0.7}Ti_{0.03})_Y$ $(Al_{5.1}Mg_{0.9})_Z$ Si_6O_{18} $(BO_3)_3$ $(O,OH)_4$. The X_{Mg} is uniform and relatively high at 0.75 ± 0.01. There is a progressive change in composition from the fibrous tourmaline in the vein, to discrete tourmaline grains on the vein rim, and then for disseminated tourmaline in the matrix with their distance from the vein (Fig. 13,14). The mean Na content decreases from 0.65 to 0.52 apfu, whereas the X-site vacancy content increases from 0.16 to 0.21. The total amount of Mg and Fe increases at the expense of Al, but the X_{Mg} remains unchanged (Fig. 13,14). Titanium increases from 0.023 to 0.034 apfu, and together with the increase in Fe is likely responsible for the darker and browner colours of the tourmaline. Fluorine was below the detection limit whereas it was routinely detected in the tourmalines in the other samples. In the tourmaline classification of (Henry and Dutrow 1996; Hawthorne and Henry 1999) these samples plot in the field of alkali tourmalines and hydroxy-subgroup.

The main greenschist silicate minerals are amphibole, plagioclase, chlorite and epidote. The fresh amphibole grains are magnesio-hornblende with an average mineral formula of $(\mathrm{Na_{0.31}K_{0.05}Ca_{0.04}})_\mathrm{A}(\mathrm{Ca_{1.86}Fe_{0.10}Mn_{0.04}})_\mathrm{B}(\mathrm{Mg_{2.67}Fe_{1.48}Al_{0.80}Ti_{0.04}V_{0.01}Cr_{0.001}})_\mathrm{C}(\mathrm{Si_{6.68}Al_{1.32}})_\mathrm{T}\mathrm{O_{22}}(\mathrm{OH_{1.98}Cl_{0.02}})$ and an X_{Mg} of 0.63. Retrograde rims are actinolite with a mineral formula of $(\mathrm{Na_{0.11}K_{0.02}Ca_{0.03}})_\mathrm{A}(\mathrm{Ca_{1.91}Fe_{0.05}Mn_{0.04}})_\mathrm{B}(\mathrm{Mg_{3.34}Fe_{1.32}Al_{0.32}Ti_{0.01}V_{0.01}})_\mathrm{C}(\mathrm{Si_{7.46}Al_{0.54}})_\mathrm{T}\mathrm{O_{22}}(\mathrm{OH_{1.98}Cl_{0.02}})$ and a somewhat higher an X_{Mg} of 0.71. Plagioclase varies in composition from $\mathrm{An_{46}Ab_{54}}$ to $\mathrm{An_{27}Ab_{73}}$ with universally low X_{Or} of 0.004. The more albitic plagioclase is found at the rim of grains and likely reflects retrograde re-equilibration. Chlorite has an average composition of $\mathrm{Mg_{3.1}Fe_{1.5}Al_{2.7}Si_{2.6}O_{10}OH_8}$ with negligible Ti, V and Cr, although a sub-population has V at 0.005 and Ti at 0.004 apfu. The Cl content is 0.03 mass%. The epidote is near end-member clino-zoisite in composition at $\mathrm{Ca_2Al_{2.6}Fe_{0.4}Si_3O_{12}OH}$. No F was detected.

Table 1. Representative mineral analyses as determined by EPMA.

	Tourmaline Vein (472823)				Micaschist (248482)						Pelite (248484)		
Wt%	Chl	Pl	Amp	Ep*	Grt	Bt	Ms	Chl	Pl	Ilm	Grt	Bt	Ms
SiO_2	25.7	58.3	43.7	39.8	36.7	35.4	47.0	24.1	58.8	0.01	37.1	35.6	45.9
TiO_2	0.00	n.d.	0.46	n.d.	0.03	1.68	0.53	0.10	0.01	52.0	0.01	1.76	0.33
Al_2O_3	22.9	26.2	15.2	29.4	20.7	17.9	36.1	22.4	26.3	n.d.	20.7	17.7	35.6
FeO_{Tot}	19.0	0.19	13.5	5.71	31.6	22.0	1.84	n.d.	0.07	47.2	35.3	22.6	2.10
MnO	0.25	0.02	0.30	0.13	3.80	0.06	n.d.	0.11	n.d.	0.83	0.94	0.04	n.d.
MgO	19.4	0.01	10.8	0.02	2.61	8.68	0.66	12.2	n.d.	0.06	2.12	8.51	0.59
CaO	0.04	7.63	11.9	24.4	3.12	0.01	0.06	0.04	7.83	0.01	3.41	n.d.	n.d.
Na_2O	n.d.	7.22	1.37	0.01	n.d.	0.17	1.31	n.d.	7.53	n.d.	0.01	0.10	0.84
K_2O	0.02	0.05	0.30	0.03	0.01	9.77	9.64	0.38	0.06	0.03	0.03	9.54	9.99
Cl	0.03		0.05	0.01		0.16	0.01	0.05				0.16	n.d.
F	n.d.		n.d.	n.d.		0.13	0.17	n.d.				0.31	0.08
H_2O	11.9		2.05	1.92		1.89	2.20	11.3				3.88	4.50
Total	98.9	99.7	99.6	101.3	98.5	97.9	99.4	99.7	100.4	99.9	99.5	100.0	100.0
a.p.f.u	O=18	O=8	O=24	O=13	O=12	O=24	O=24	O=18	O=8	O=3	O=12	O=24	O=24
Si	2.62	2.61	6.40	3.06	3.00	5.71	6.42	2.57	2.62	<0.01	3.01	5.50	6.12
Ti	<0.01	n.d.	0.05	n.d.	<0.01	0.20	0.05	0.01	<0.01	0.99	<0.01	0.20	0.03
Al	2.75	1.39	2.62	2.66	1.99	3.40	5.80	2.82	1.38	n.d.	1.98	3.23	5.59
Fe_{Tot}	1.62	0.01	1.65	0.37	2.16	2.97	0.21	2.61	<0.01	1.00	2.39	2.92	0.23
Mn	0.02	<0.01	0.04	0.01	0.26	0.01	<0.00	0.01	n.d.	0.02	0.06	0.01	n.d.
Mg	2.95	<0.01	2.37	<0.01	0.32	2.08	0.14	1.94	n.d.	<0.01	0.23	1.96	0.12
Ca	<0.01	0.37	1.86	2.01	0.27	<0.01	0.01	<0.01	0.37	<0.01	0.27	n.d.	n.d.
Na	n.d.	0.63	0.39	<0.01	n.d.	0.05	0.35	n.d.	0.65	n.d.	<0.01	0.03	0.22
K	<0.01	<0.01	0.06	<0.01	<0.01	2.01	1.68	0.05	<0.01	<0.01	<0.01	1.88	1.70
Cl	0.01		0.01	<0.01		0.04	<0.01	0.01				0.04	n.d.
F	n.d.		n.d.	n.d.		0.06	0.07	n.d.				0.15	0.04
H	8.09		2.00	0.99		2.03	2.00	8.03				4.00	4.00
Fe^{2+}					2.15					0.99	2.38		
Fe^{3+}					0.01					0.01	0.01		

	Pelite (248484)					Tourmalinite (248483)						
Wt%	Chl	Pl	Ilm	Mt	Ep*	Grt	Bt	Chl	Pl	Ilm	Amp	Ep*
SiO_2	24.0	58.9	n.d.	0.03	38.3	35.8	37.4	24.4	57.7	0.01	53.7	38.3
TiO_2	0.06	<0.01	51.96	0.05	0.06	0.01	1.71	0.18	n.d.	52.0	0.10	0.08
Al_2O_3	21.8	25.8	n.d.	0.14	26.1	20.9	18.0	22.6	26.0	0.02	3.34	27.2
FeO_{Tot}	29.5	0.07	46.53	90.7	10.1	35.6	21.9	28.1	n.d.	46.0	10.1	7.58
MnO	0.11	0.02	0.82	0.02	0.06	1.85	0.04	0.12	n.d.	0.50	0.30	0.20
MgO	12.2	n.d.	0.08	n.d.	0.02	1.70	8.29	12.5	n.d.	0.10	17.3	0.02
CaO	0.02	7.02	n.d.	n.d.	23.3	2.66	n.d.	0.01	7.46	n.d.	12.5	23.9
Na_2O	n.d.	7.42	<0.01	0.03	<0.01	0.01	0.21	n.d.	7.60	n.d.	0.27	0.01
K_2O	0.02	0.07	0.02	0.02	0.03	0.02	9.36	0.13	0.07	<0.01	0.05	0.02
Cl	0.02				0.01			0.03			0.03	n.d.
F					n.d.		0.18				n.d.	0.19
H_2O	11.3				1.92			11.4			2.11	
Total	99.0	99.3	99.1	91.0	99.8	98.5	97.1	99.3	98.9	98.6	99.8	99.6
a.p.f.u	O=18	O=8	O=3	O=4	O=13	O=12	O=11	O=18	O=8	O=3	O=24	O=13
Si	2.58	2.64	n.d.	<0.01	3.00	2.95	2.90	2.59	2.61	<0.01	7.63	3.01
Ti	<0.01	<0.01	0.99	<0.01	<0.01	<0.01	0.10	0.01	n.d.	1.00	0.01	<0.01
Al	2.77	1.37	n.d.	0.01	2.41	2.04	1.65	2.83	1.39	<0.01	0.56	2.52
Fe_{Tot}	2.66	<0.01	0.99	2.99	0.59	2.46	1.42	2.50	n.d.	0.98	1.20	0.45
Mn	0.01	<0.01	0.02	<0.01	<0.01	0.13	<0.01	0.01	n.d.	0.01	0.04	0.01
Mg	1.95	n.d.	<0.01	<0.01	<0.01	0.21	0.96	1.98	n.d.	<0.01	3.68	<0.01
Ca	<0.01	0.34	n.d.	<0.01	1.95	0.23	n.d.	<0.01	0.36	n.d.	1.91	2.01
Na	n.d.	0.65	<0.01	<0.01	<0.01	<0.01	0.03	n.d.	0.67	n.d.	0.07	<0.01
K	<0.01	<0.01	<0.01	<0.01	<0.01	<0.01	0.93	0.02	<0.01	<0.01	0.01	<0.01
Cl	<0.01				<0.01			0.01			0.01	n.d.
F					n.d.		0.04				n.d.	0.05
H	8.08				1.00			8.06			2.00	1.00
Fe^{2+}				1.00		2.37						
Fe^{3+}				1.99		0.08						

*Epidote analyses list Fe_2O_{3Tot}

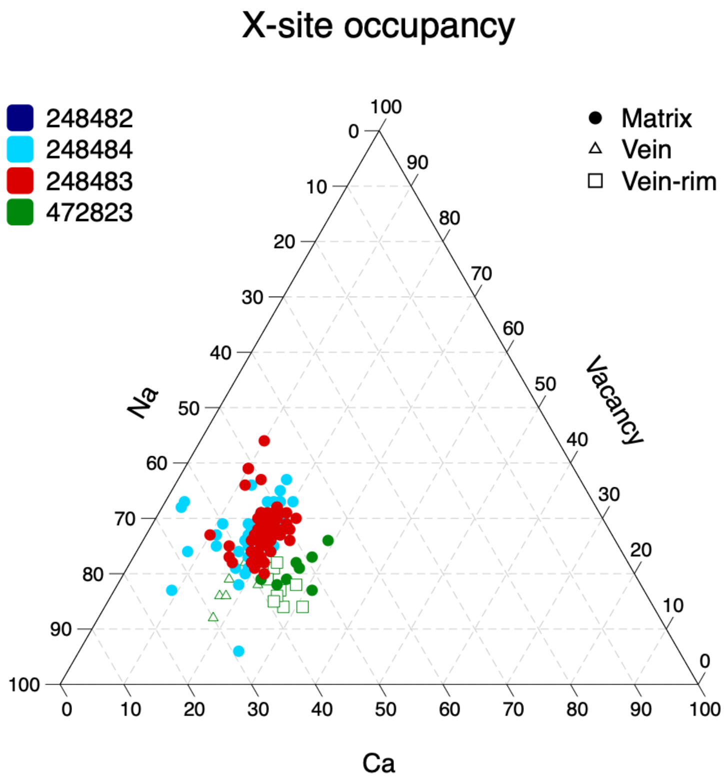
X-site occupancy
248482
248484
248483
472823
Matrix
Vein
Vein-rim
Na
Vacancy
Ca
0
10
20
30
40
50
60
70
80
90
100

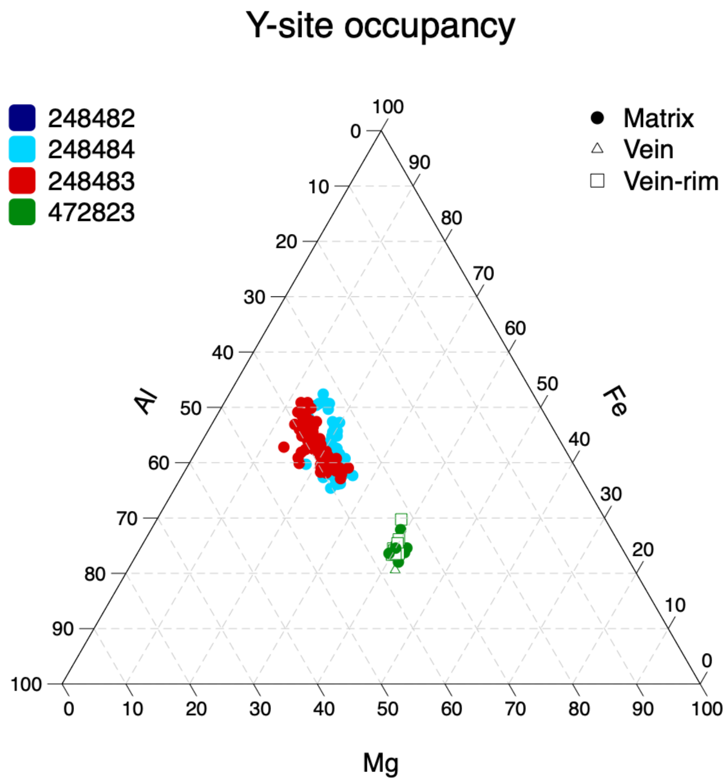

Figure 13: Major X- and Y-site occupancy of the tourmalines analysed in this study. The tourmalines in the greenschist-hosted tourmaline vein are split into those occurring as fibres in the vein, discrete grains at the edge of the vein, and grains in the greenschist matrix.

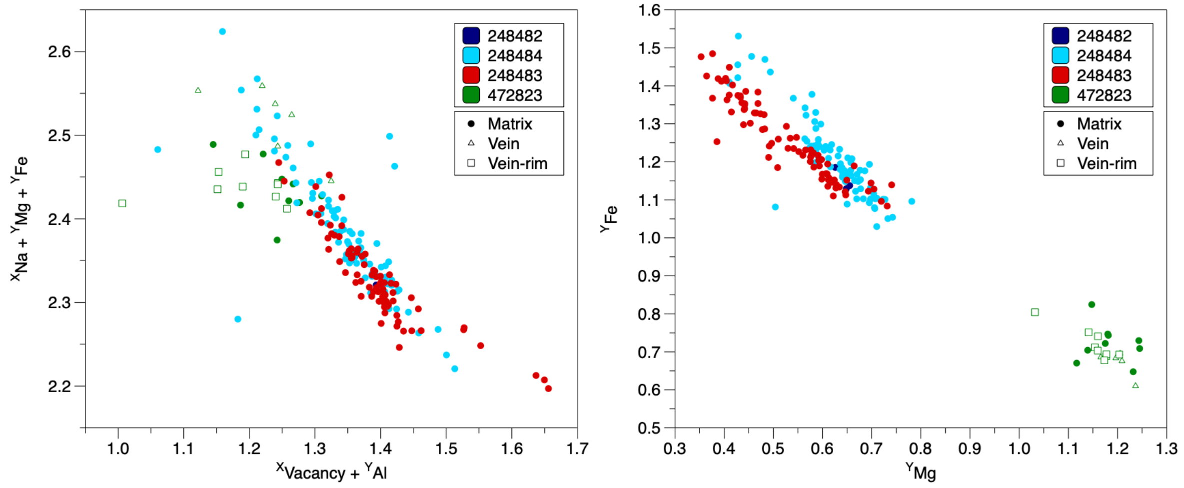

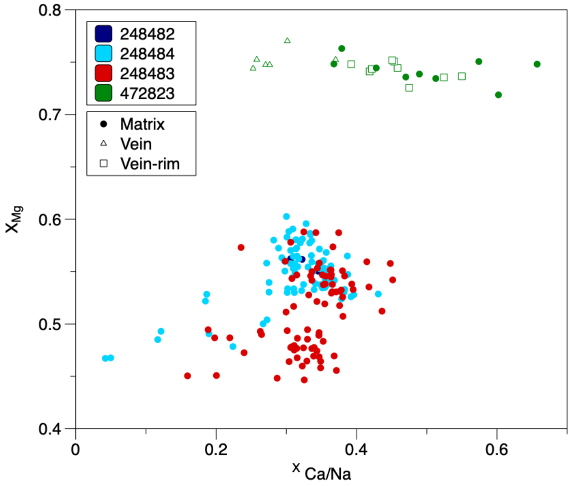

Figure 14: Tourmaline compositional differences among the samples, further subdivided into the types of tourmaline for the greenschist hosted tourmaline vein sample (472823). A,B. The Schorl-Dravite to (Mg,Fe)-foitite vector (exchange of elements within the solid solution of the tourmaline) and Y-site Fe <-> Mg exchange are the dominant exchange vectors; C. The vein tourmaline is distinct in its high X_{Mg} and further shows a progressive increase in Ca/Na with distance from the vein. The tourmalines in the tourmalinite (248483) display a bimodal distribution, with the rim compositions overlapping with the tourmalines found in the host meta-pelite unit (248482 and 248484).

3.2.2 Meta-pelite

Biotite has an X_{Mg} from 0.32 to 0.41 (mean of 0.39). It contains up to 0.21 Ti pfu, 0.02 Na pfu, 0.3 apfu ^{VI}Al, 0.02 apfu Cl and 0.04 apfu F. Compositional differences among thinsections and samples are negligible. The muscovite contains 19 ± 3% celadonite and 12 ± 3% paragonite components, but negligible margarite. There are small amounts of Ti and F at up to 0.05 and 0.07 apfu, respectively. The muscovite in sample 248482 is more Ti and F rich than 248484 and has a somewhat higher celadonite component and X_{Mg}. Plagioclase compositions show little variability among thinsections with a mean composition of $An_{35\pm1}Ab_{65\pm1}$. The orthoclase component is minimal at 0.38 ± 0.07%. There is no significant difference in plagioclase composition between the more aluminous 248484 samples and the more quartzo-feldspathic 248482 micaschist.

Garnet grains are zoned and show a range of compositions. Textural zoning and compositional zoning do not appear to have a relationship as the compositional trends do not deviate at textural boundaries. They are almandine-dominated at X_{Alm} from 0.64 to 0.83, X_{Py} from 0.05 to 0.11, X_{Gros} from 0.07 to 0.16, X_{Spes} from 0.01 to 0.16 and an X_{Mg} from 0.06 to 0.13. Point analyses were collected for geothermobarometry as well as transects over two garnet grains (Fig. 15). The garnet grains for these transects were selected for their large size and apparent full coverage of zoning, although it is unlikely that these, or any in the thinsection, represent a true section through the middle of the garnet. In sample 248482, there is an overall decrease in X_{Spes} and X_{Gros} from core to rim, with X_{Spes} showing a Mn-rich growth zone close to the rim and a sharp Mn increase at the outermost rim. The X_{Mg} follows the X_{Spes}, but shows the inverse. The outermost rim likely reflects retrograde re-equilibration. The high Mn, low X_{Mg} growth zone suggests an event or reaction that liberated Mn and Fe, and made it available for incorporation into the garnet.

The garnets in sample 248484 have much lower Mn contents, which likely reflects low bulk rock MnO content. The grossular and pyrope components are also somewhat lower. There are also differences ion absolute component fractions between the two garnet grains, but the core-rim trends are identical (Fig. 15). The core-rim trends in sample 248484 are similar to those in 248482, in particular in the X_{Mg} profile. However, the grossular content shows a sharp increase in the rim that is absent in sample 248482. Nonetheless, we conclude that the garnet grains in these samples broadly record the same growth history.

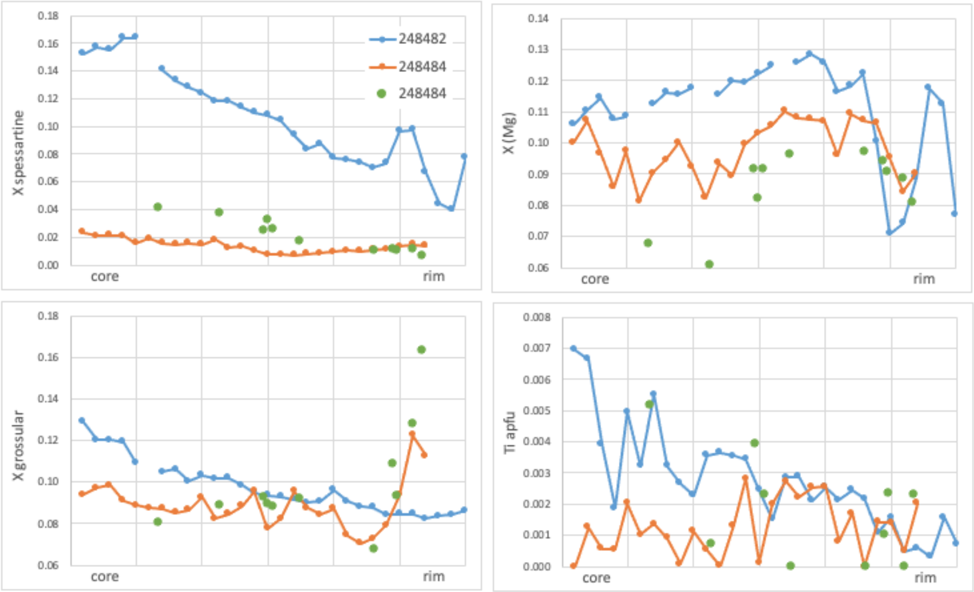

Figure 15: Core-rim transects over large garnet grains in the meta-pelite samples 248482 and 248484. The points connected by lines are for an equally spaced line analysis, whereas the green points are for located spot analyses.

The samples contain two oxides, magnetite and ilmenite. Magnetite dominates in the matrix of sample 248484, but both are present in the matrix and as co-existing inclusions in the rim and mantle zones of the garnet grains. Magnetite is near end-member with a maximum ülvospinel and hercynite component of 0.6% and 0.7%, respectively, and no detectable spinel component. The ilmenite is similarly near end-member ilmenite in composition ($Ilm_{99.3-99.5}$) with the remainder made up of a pyrophanite component at 0.3 to 0.5% and geikielite from 0.1 to 0.2%. The hematite component is *ca.* 3±1%. The near end-member compositions of these oxides do not permit meaningful estimates of equilibrium temperature or fO_2 to be obtained from them.

The tourmalines in the meta-pelite samples have overlapping compositions (Fig. 13,14) with an identical median mineral formula within uncertainty of $(Na_{0.55}Ca_{0.18}K_{0.01}Vac_{0.26})_X$ $(Al_{1.1}Mg_{0.6}Fe_{1.2}Ti_{0.08})_Y$ $(Al_{5.2}Mg_{0.8})_Z$ $(Si_{5.8}Al_{0.2})_TO_{18}$ $(BO_3)_3$ $(O,OH,F)_4$. The growth zoned grains display a general trend of increasing X_{Mg} from core to rim, and the dominant exchange vectors are $^{X}Na + ^{Y}(Mg,Fe) = ^{X}Vac + ^{Y}Al$ and $^{Y}Mg = ^{Y}Fe$ (Fig 14a,b).

3.2.3 Tourmalinite

The biotite has an X_{Mg} of 0.4 and contains 0.1 Ti pfu, 0.06 Na pfu, 1.64 apfu ^{VI}Al, and 0.05 apfu F (Cl was not analysed). Plagioclase has minimal compositional variability among grains and thinsections with a mean composition of $An_{35\pm1}Ab_{65\pm2}$ and a negligible orthoclase component. Retrograde replacement has up to a near end-member albite composition (Ab_{99}). The ilmenite is Ilm_{98-99} with up to 1% geikielite and 2% pyrophanite components. The hematite component of the ilmenite is minimal at up to 1%. All these minerals in the tourmalinite are similar in composition to those in the host meta-pelite.

Garnet is almandine-dominated (Alm_{77-82}) with 6 to 13% grossular, 6 to 11% pyrope and 1 to 7% spessartine components. The garnet grains are strongly zoned, but lack clear core to rim trends (Fig. 16). The compositions of the two grains analysed are moreover different at equivalent core-rim distance, although this could reflect a difference in sectioning level. The mean garnet composition is similar to that in the host meta-pelite (cf. Figs. 15 and 16) and it shows an equivalent range in composition from core to rim. This suggests that the irregular pattern observed from core to rim is not the effect of diffusional re-equilibration destroying the original regular zoning, but rather a feature of the garnets in this sample. This could indicate sharp changes in the exchanging mineral assemblage, but the presence of all matrix phases as inclusions throughout the garnet argues against this, or open-system control on composition.

Tourmaline is bimodal in composition, which is most distinct in X_{Mg} (Fig 14c), with the modes representing the core and the mantle + rim, respectively. The median core mineral formula is $(Na_{0.55}Ca_{0.18}K_{0.01}Vac_{0.26})_X$ $(Al_{1.1}Mg_{0.4}Fe_{1.4}Ti_{0.07})_Y$ $(Al_{5.2}Mg_{0.8})_Z$ $(Si_{5.6}Al_{0.4})_TO_{18}$ $(BO_3)_3$ $(O,OH,F)_4$., whereas the mantle + rim define a median tourmaline of formula $(Na_{0.53}Ca_{0.19}K_{0.01}Vac_{0.27})_X$ $(Al_{1.1}Mg_{0.6}Fe_{1.2}Ti_{0.08})_Y$ $(Al_{5.2}Mg_{0.8})_Z$ $(Si_{5.6}Al_{0.4})_TO_{18}$ $(BO_3)_3$ $(O,OH,F)_4$. The mantle + rim overlap in composition with the tourmalines in the meta-pelite samples

(Fig. 15,16), with slightly higher ^{T}Al (0.4 vs. 0.2 apfu) and Cr (0.005 vs. 0.002) as the main differences. The tourmaline compositions are intermediate between the dravite, schorl, uvite and foitite end-members, and belong to the alkali group and hydroxy sub-group of the tourmaline nomenclature.

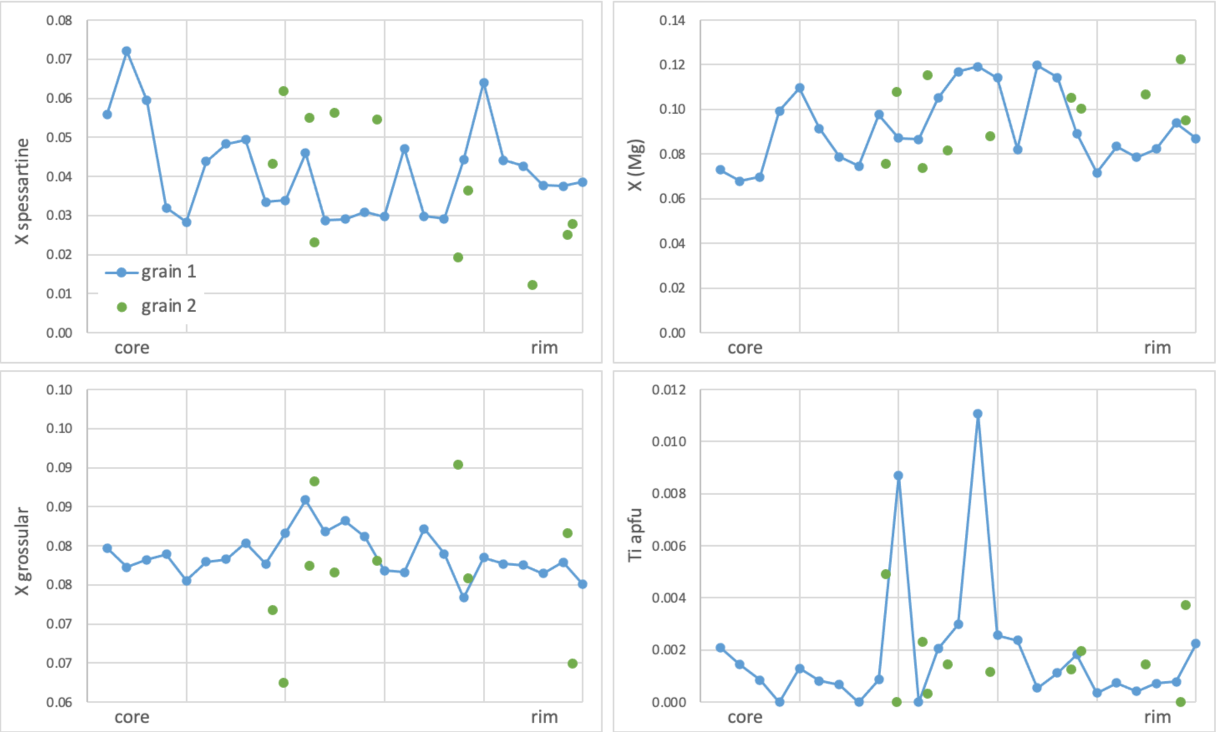

Figure 16: Compositional transect over a garnet grain in the tourmalinite sample 248483 (blue) and located spot analyses in a second garnet grain (green). There are no persistent trends from core to rim.

3.3 Zircon and apatite petrography and compositions

Zircon grains occur as small, idiomorphic inclusions in the micas and garnet, and in larger tourmaline grains in the tourmalinite. They also occur as dispersed accessory grains in the matrix of the samples. The zircon grains have equilibrium contacts with the foliation-defining micas, which also share equilibrium contacts with the tourmalines. We interpret that they were formed synchronously with the tourmaline. The zircons show minimal zoning in CL or BSE imaging (i.e. appearance is metamorphic in nature). Two of the zircons from the meta-pelite unit displayed cores in BSE imaging and both cores and rims were dated. The zircons in the tourmalinite display no textural difference between grains in the matrix and those present as inclusions in garnet and tourmaline, and we therefore interpret these to represent the same generation. Zircons in the matrix are mostly found associated with biotite, or in mica bands close to garnet. The zircons in the tourmalinite are unzoned aside from thin (< 5 μm) rims on some of the grains, and they are generally euhedral. Only a small subset of identified zircons could be analyzed because of laser ablation constraints (minimum crater size of 25 μm) or because they are not exposed on the sample surface.

No zircons of sufficient size were identified in the greenschist-hosted tourmaline vein sample (all are < 10 μm), and we dated apatite instead. Apatite grains in this sample are found in the host schist as dispersed accessory grains up to 150 μm in size, which display equilibrium contacts with all matrix minerals, including tourmaline. Larger, equant grains were selected for analysis to maximize the amount of sample material, and we analysed grains from adjacent to the vein to increasingly further away from it. The apatites become progressively smaller away from the vein, and the apatite composition, moreover, varies systematically, with apatite grains further away from the vein richer in Fe and Cl (Fe ranges from 0.154 wt% proximal to the vein to 0.263 wt% distal to the vein). These compositional systematics, together with the spatial size distribution are interpreted to reflect formation of apatite by fluid infiltration from the vein, equivalent to how we interpret the systematic colour variations in the tourmaline away from the vein. Whether the appearance of apatite is because of phosphorous-metasomatism, or the fluids simply trigger apatite formation is unclear, and is also not important here. What is essential is that apatite formation dates the veining event, and hence the appearance of tourmaline in this unit.

3.4 U-Pb geochronology

3.4.1 Zircon

All 17 zircon analyses from the meta-pelite sample are discordant and broadly form an array in ^{207}Pb/^{235}U vs ^{206}Pb/^{238}U space (Fig. 17a, data in the Supplementary Data File). After rejecting two analyses that were inconsistent with the trend, the 15 remaining analyses define a poorly constrained discordia with an upper intercept of 3724.3 ± 41.7 Ma and a lower intercept of 1790 ± 141 Ma (MSWD = 9). Zircon rims (n = 15) and cores (n = 2) yielded indistinguishable results, as they appear to define the same discordia. The poor fit of the discordia may indicate that the Pb loss history of this sample is more complex, though this cannot be resolved.

Zircon in the tourmalinite sample yielded 3 concordant analyses and 21 discordant analyses (Fig. 17b). The large spread in the discordant data prohibits the calculation of a robust discordia, and therefore we focus here on the concordant data. The three concordant zircon analyses yield an age of 3595.4 ± 11.3 Ma (MSWD = 1.3).

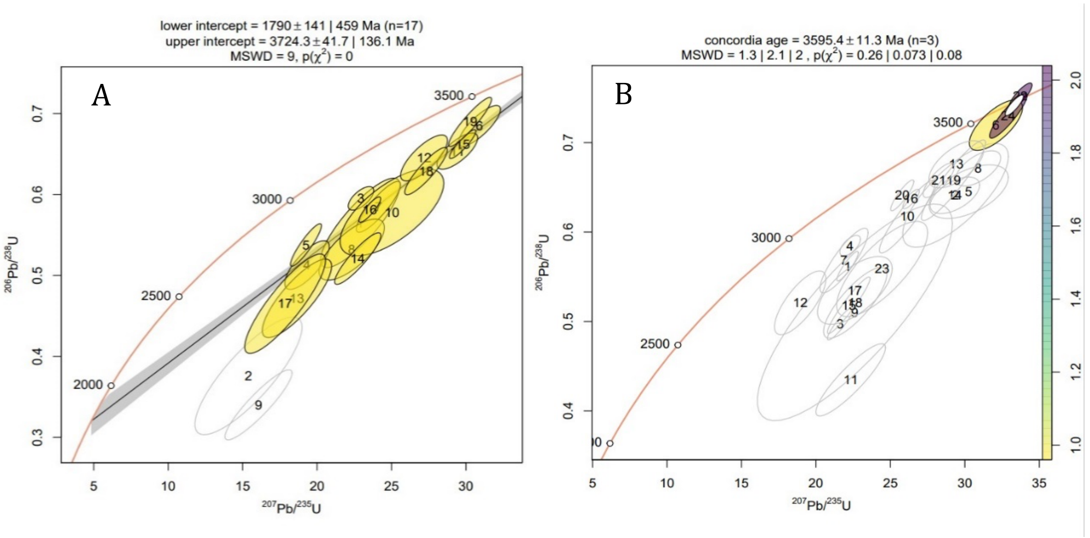

Fig. 17: Concordia diagrams showing results from zircon U-Pb geochronology for a) the meta-pelite sample and b) the tourmalinite sample.

3.4.2 Apatite

The 10 apatites analysed yielded sufficient U/Pb spread for calculation of a discordia in ^{238}U/^{206}Pb vs ^{207}Pb/^{206}Pb space (Fig. 18, data in the Supplementary Data File). When anchored at the ^{207}Pb/^{206}Pb value of vein tourmaline of 1.117 ± 0.033, the lower intercept with concordia is 1721 ± 76 Ma (2SE) with an MSWD of 1.2. Given the uncertainties for ^{207}Pb/^{206}Pb of both apatite and tourmaline, the calculated ordinate intercept is 1.145 ± 0.023. We interpret these results as the age and common Pb composition, respectively, of the co-precipitated apatite and tourmaline.

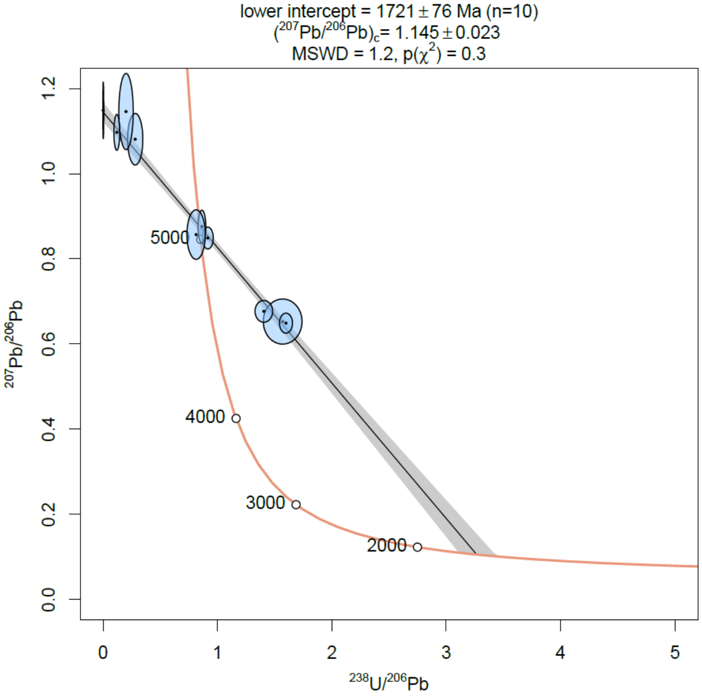

Fig 18:. Tera-Wasserburg concordia plot showing the calculated discordia for the apatite analyses, anchored at the ^{207}Pb/^{206}Pb composition of tourmaline in the same sample (1.117 ± 0.033).

4. Discussion

4.1 Geothermobarometry

4.1.1 Meta-pelite and tourmalinite

Hourglass sector zoning provides an opportunity to reconstruct the temperature-history of tourmaline formation, e.g. (van Hinsberg and Schumacher 2007, 2011; Berryman et al. 2017). In this thermometer, the temperature dependence of element partitioning between adjacent sectors in matching growth zones provides temperature constraints on formation of each growth zone, which are moreover preserved as a result of tourmaline's negligible diffusional re-equilibration (van Hinsberg et al. 2006; van Hinsberg et al. 2011). Two approaches were used to obtain matching pairs, both guided by back-scattered electron images and element maps of the sector zoning. In the first, growth zones were identified and analyses in a given growth zone but in adjacent sectors were directly matched. Although this provides the highest confidence, it lacks spatial resolution as there is only a limited number of growth zones that is sufficiently distinct to identify in imaging and element maps, and equivalence of growth can be difficult to establish. To obtain a higher resolution record, we used linear interpolation to obtain compositions at matching distances along core-rim transects in the two sectors. This method assumes that the relative growth rate of the two sectors is constant, i.e. the slope between the two sectors is constant (cf. van Hinsberg and Schumacher 2007). This is the case from core to rim for the meta-pelite tourmalines we analysed, but a kink is present for the tourmalinite tourmalines between the core and the mantle + rim (Fig. 21), and these two sections were therefore interpolated separately. Our tourmaline thermometry focuses on ***c+*** and ***a*** sector contacts as these are most clearly identifiable in the imaging and element maps, and therefore allow for the most accurate localisation of corresponding analyses. The ***c-*** sector is present in most grains, and can be recognised in sections perpendicular to ***c*** as a darker core.

Inter-sector thermometry was applied to two sector-zoned tourmaline grains in the meta-pelite (Fig 19a,b). Both grains display compositional heterogeneity in the +***c*** core, especially in Ti. This is common in metamorphic tourmaline and generally interpret to reflect inherited compositional variability from the precursor phases, (see e.g. van Hinsberg et al. 2017) coupled with low diffusion rates and fluid-solubility at low temperature, in particular for Ti, that inhibit mobilisation. We therefore applied a smoothing to the data and used that to derive interpolated temperatures (Fig. 20). The grains provide comparable results with nucleation at *ca.* 350-400˚C followed by progressive prograde growth to peak conditions of 650°C. The temperature estimates from Ca and Ti thermometry are equivalent and the overall T trends identical. The innermost core in grain M1 is thin (Fig 18a) and precise positioning of analyses points was challenging, especially because the sector zoning, clear in element mapping, is not obvious in BSE imaging. As a result, the +***c*** analyses of the inner core may have been influenced by the adjacent ***a*** sector, resulting in underestimating the element fractionation between the sectors and hence overestimating the temperature of formation. We therefore do not interpret this part of the temperature profile. The interpolated data also suggest a decrease in temperature for the mantle (60-80% along the core-rim transect), but the directly matched points do not provide the resolution to confidently confirm this. We prefer to interpret this as a (rapid) growth event at near-constant temperature, consistent with the temperature history for the compiled data (Fig. 20a).

The thermal history, and progressive prograde growth are consistent with that predicted for closed-system progressive redistribution of boron from clay and mica precursor minerals to tourmaline (van Hinsberg et al. 2011). There are no steps or gaps in the sectors or thermal profile and the tourmaline composition varies progressively with the temperature. We therefore interpret these tourmalines to be of metamorphic origin and record the prograde history of the sample from 350-400˚C to peak metamorphic conditions.

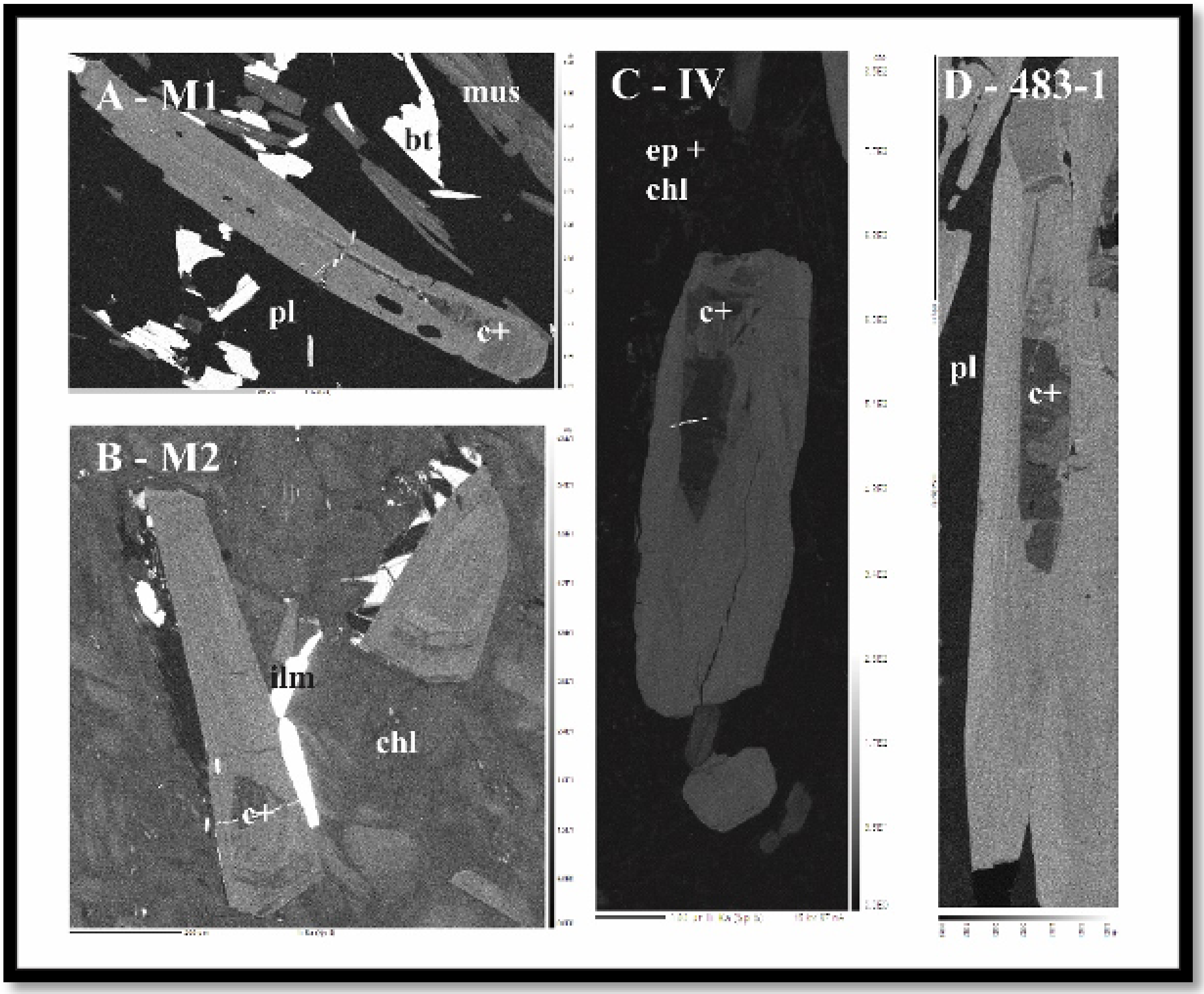

Figure 19: EPMA-WDS Ti element maps for sector zoned tourmaline grains in the meta-pelite (A,B) and the tourmalinite (C,D). Hourglass sector zoning can be observed, especially as the darker, lower Ti ***c+*** *sectors, with concentric growth zoning cutting through the sectors. Overall, the contrast in Ti content between the adjacent sectors decreases from core to rim, which suggests prograde growth.*

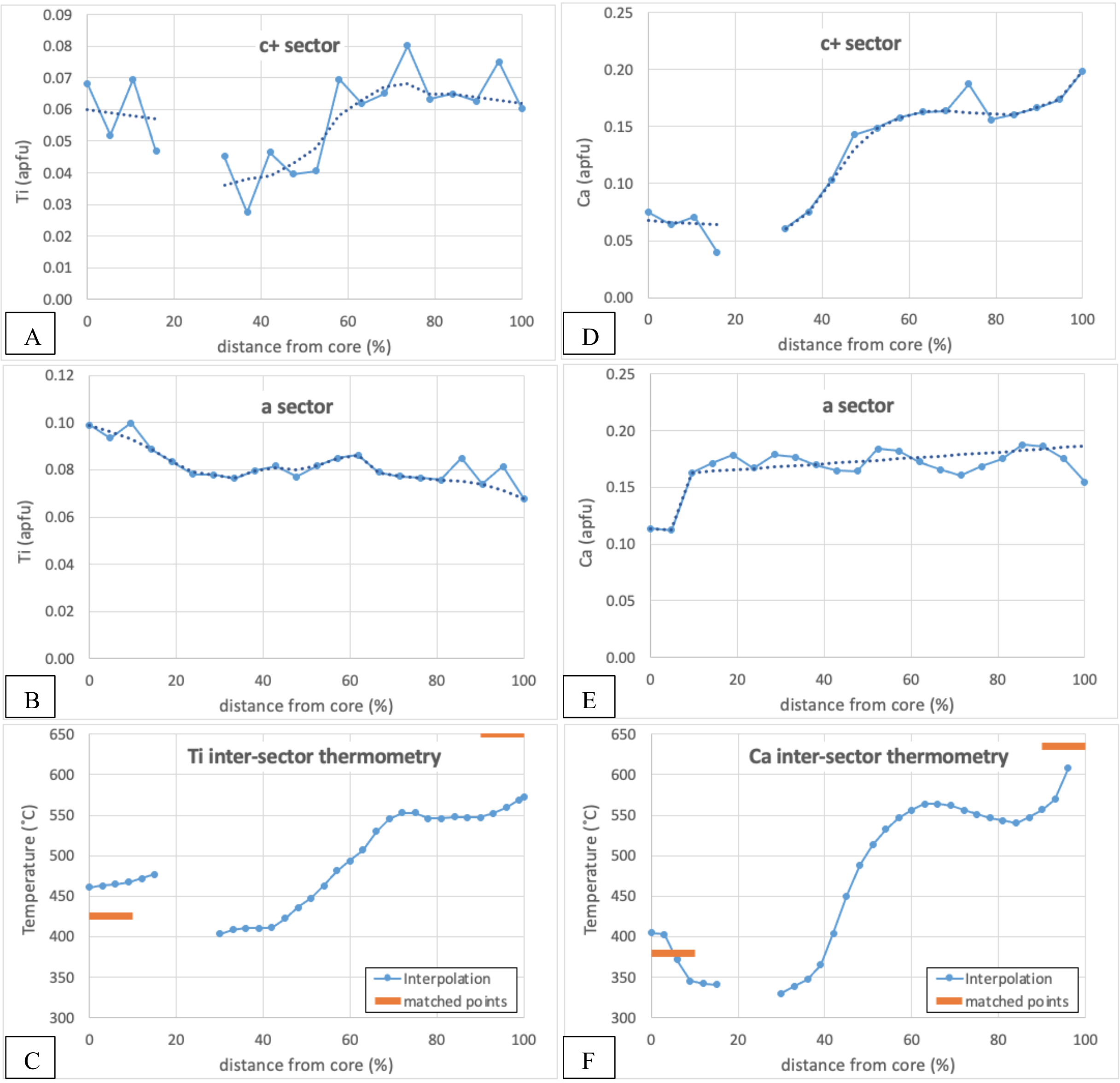

Figure 20: Inter-sector thermometry results for core-rim transects in two tourmaline grains in the meta-pelite, one in thinsection 248484-M1 (above) and the other in 248484-M2 (next page). Element maps of these grains are shown in Fig 19A,B.A-D and G-J: compositions in the adjacent c+ and a sectors for Ti and Ca, with coordinates harmonized to distance from the core in %. Smoothing was applied to the compositional data to account for heterogeneity inherited from the precursor mineral(s), and is shown as the dashed line. E-F,K-L: Temperatures derived from the interpolated, smoothed curves (blue) and from directly matched growth zones (orange). The matched points have highest confidence, but only few growth zoned were sufficiently distinct in imaging to match. Interpolation assumes constant relative growth rates between sectors.

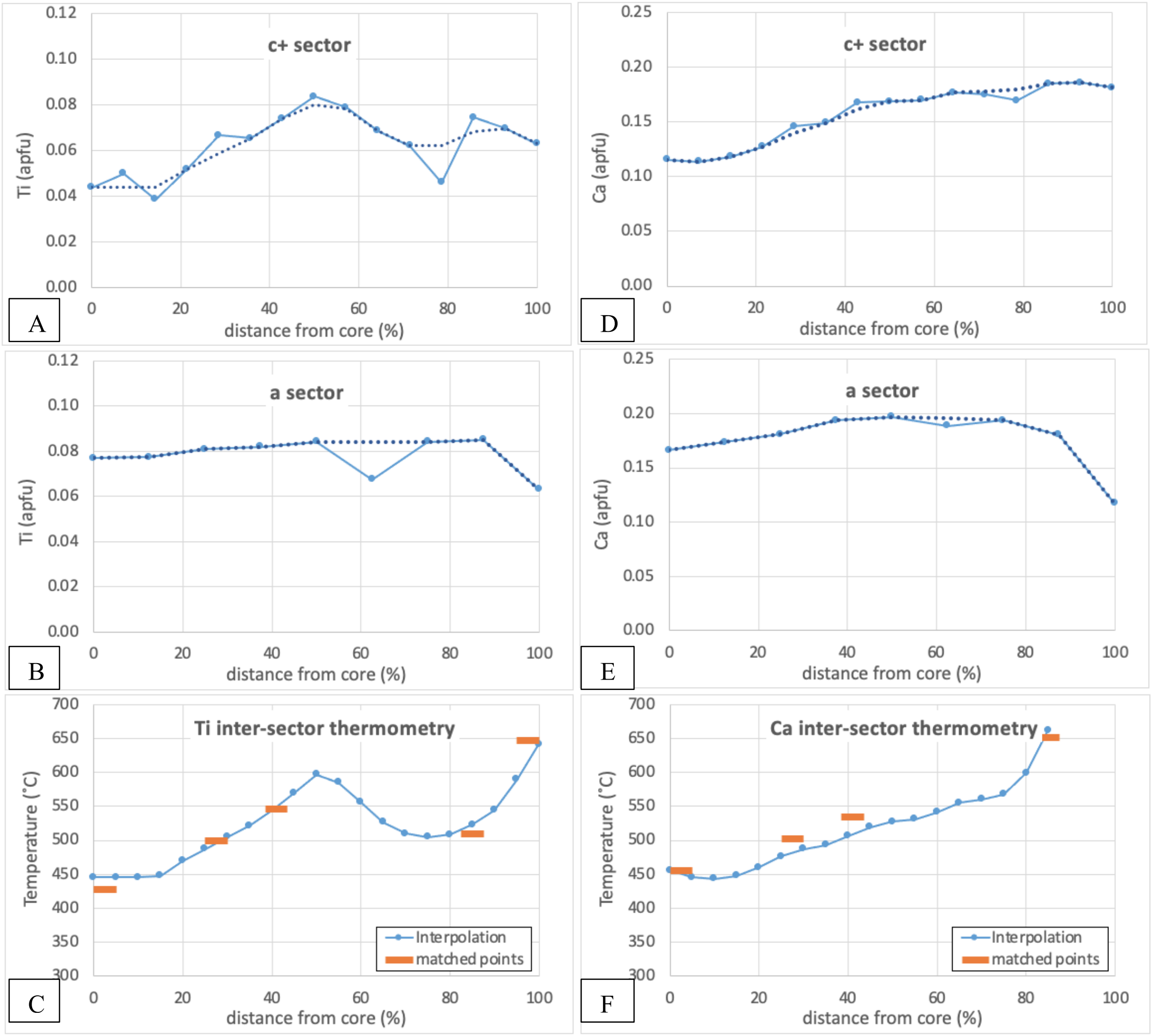

Figure 20: Continued, results for M2.

Inter-sector thermometry of the tourmalinite tourmalines shows two-stage growth (Fig. 21). The core of the grains formed at a near constant temperature of 350 ± 10˚C with excellent correspondence between Ca and Ti derived temperatures and for the two grains analysed. The mantle and rim show prograde growth up to *ca.* 600˚C. Interpolated and directly matched points are consistent in this thermal history. The tourmaline in core I appears to record retrograde growth in its rim with temperature decreasing to 500˚C. However, the zooming in the core is irregular in this part (Fig. 19c) and the compositional trends in the ***c+*** sector with decreasing Ca and Ti are not observed in the corresponding ***a*** sector (Fig. 21A). It can therefore not be excluded that this is an artefact. The tourmaline grain in core IV has a dark band at approximately 85% of the core-rim distance in its ***c+*** sector (Fig. 19d), which corresponds to a trough in Ca and Ti. The corresponding ***a*** sector does not show this in either the element maps or the compositional transect. We interpret this trough as compositional heterogeneity and the smoothed curve excludes it (Fig. 21g,h).

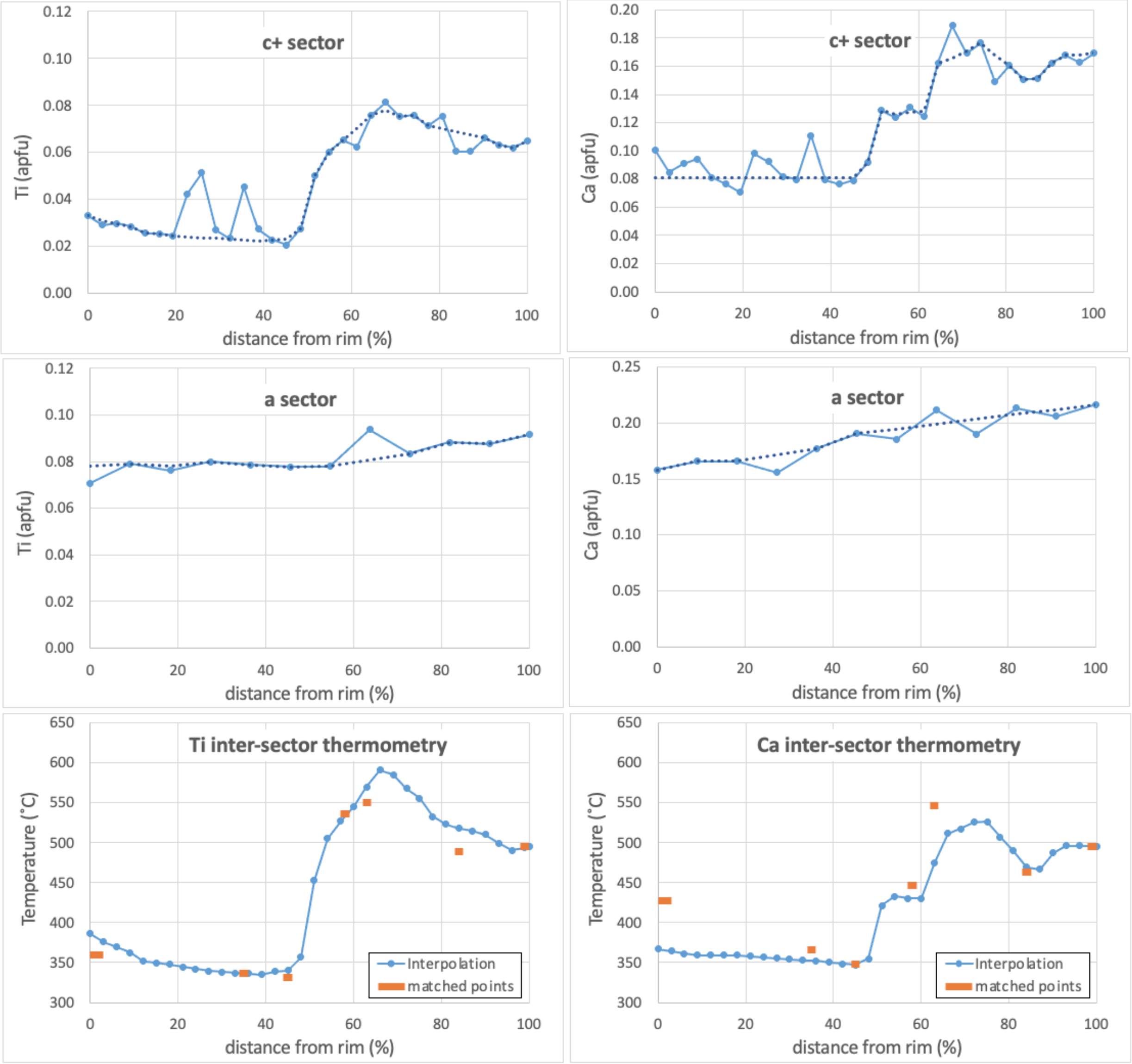

Figure 21: Inter-sector thermometry for core-rim transects in two tourmaline grains in the tourmalinite (core I above, core IV on the next page). Element maps of these grains are shown in Fig 19C,D. Further details as per the caption of figure 19.

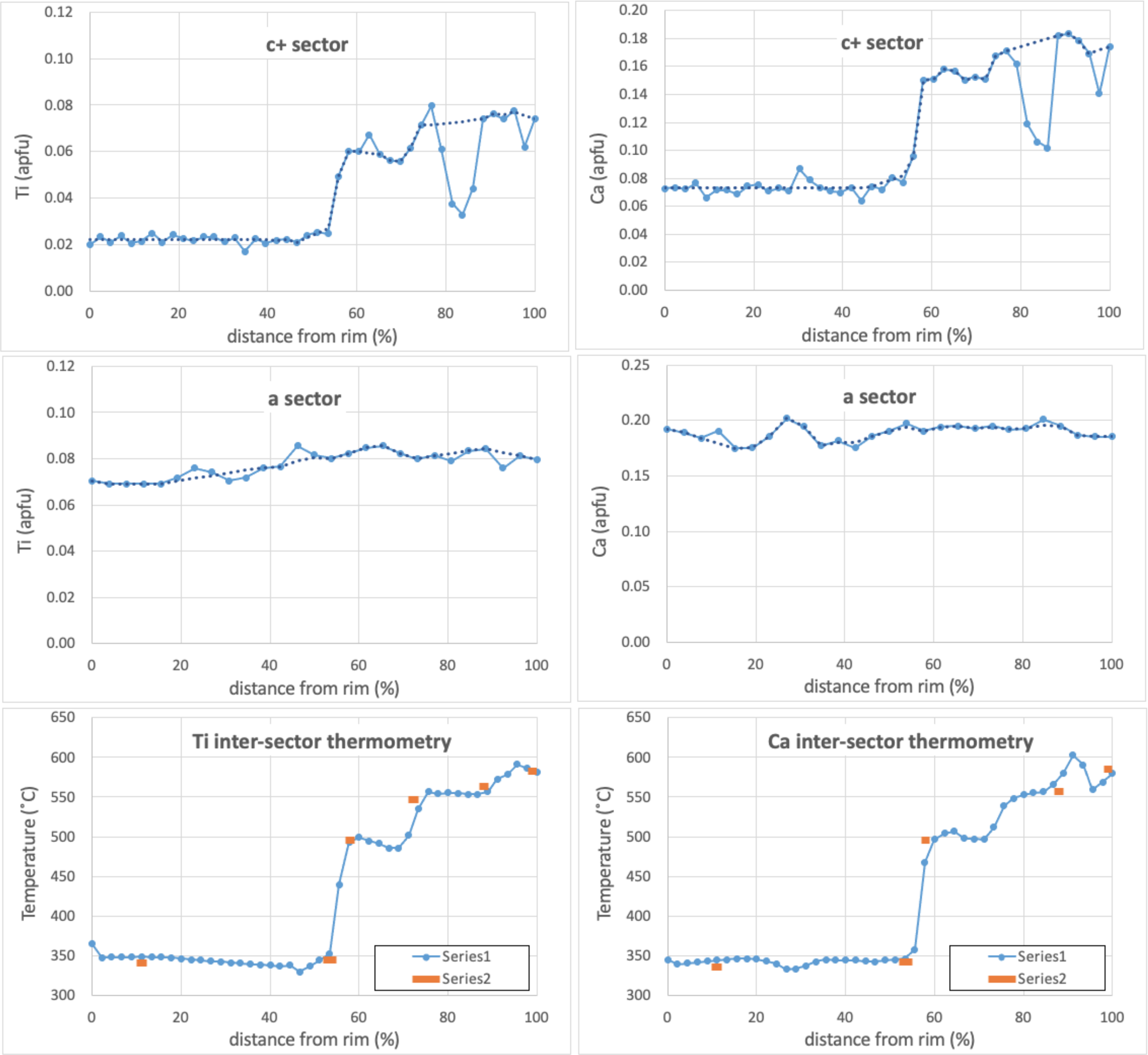

Figure 21 continued. Tourmaline grain in core IV of the tourmalinite.

The tourmaline temperature can be compared against temperature constraints derived from the peak metamorphic minerals. Ti-in-biotite thermometry (Henry et al. 2005) on large, well-preserved biotite grains in the matrix of the meta-pelite and tourmalinite samples gives indistinguishable temperature estimates of 575 ± 9˚C (n = 4) for sample 248482, 573 ± 3˚C (n = 2) for 248483 and 577 ± 15˚C (n = 15) for 248484. Garnet-biotite thermometry using the (Bhattacharya et al. 1992) calibration with garnet mixing parameters from (Hackler and Wood 1989) provides equivalent temperature estimates at 623˚C for sample 248482, 607˚C for 248484 and 592˚C for 248483, with a temperature variability of ± 35˚C for each sample. Combining the garnet-biotite temperatures with the GASP (Holdaway 2001) and GPMB (Hodges and Crowley 1985) barometers provides pressure estimates of 6.7 ± 1.0 kbar (248482), 6.1 ± 0.9 kbar (248484), and 5.2 ± 0.9 kbar (248483). These pressures are similar, albeit at the low end, of estimates in the literature (see Nutman et al. 2022 for an overview). This could be because of the absence of an Al-silicate in our samples, although kyanite is known from the meta-pelite unit and the results of the GPMB barometer, which does not require the presence of Al-silicate, is equivalent to GASP.

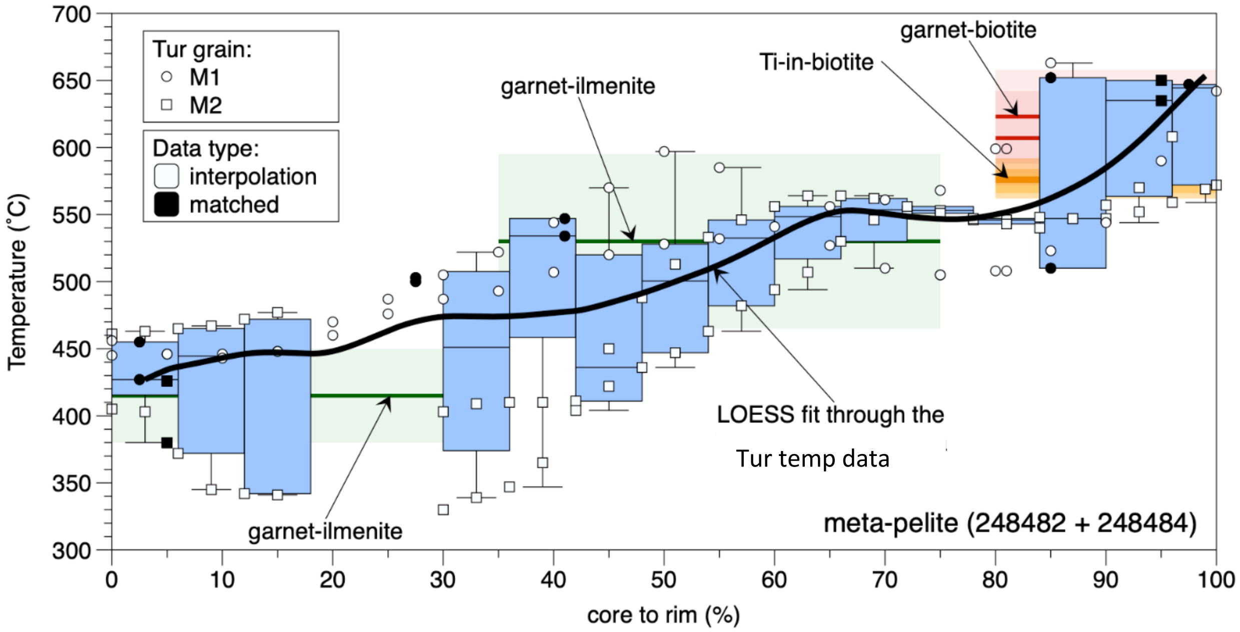

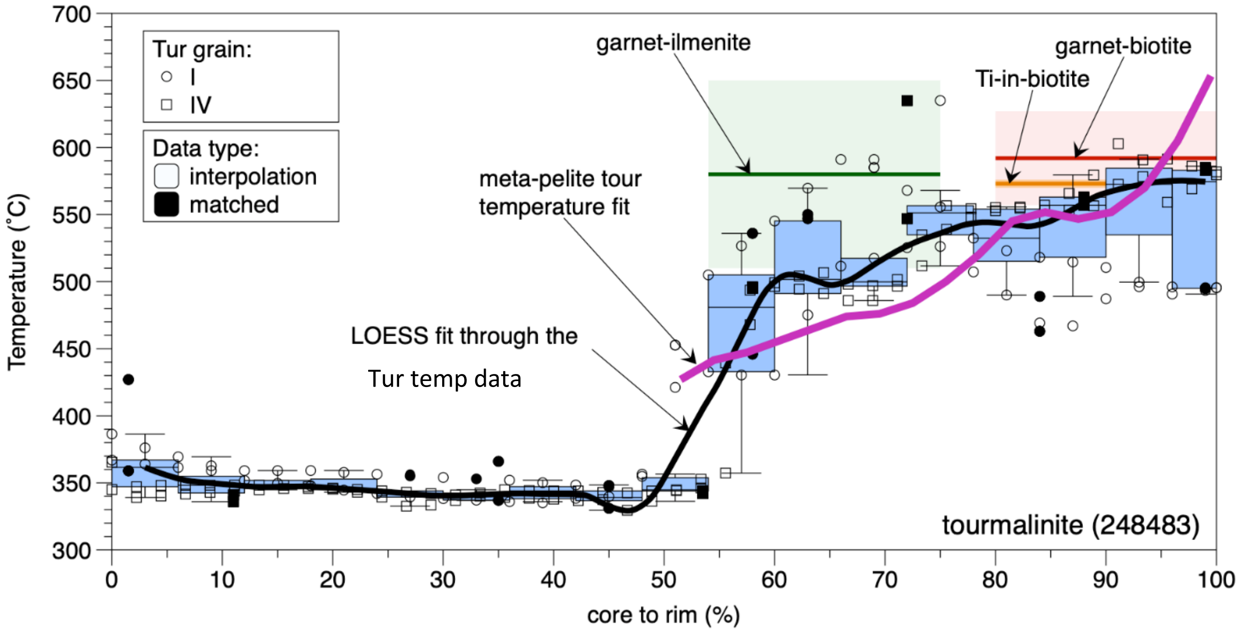

Figure 22: Compilation of temperature data for the meta-pelite (A) and the tourmalinite (B). Inter-sector thermometry data are presented as symbols subdivided for source grain and type, and subsequently binned in 6% intervals displayed as box-and-whiskers. A LOESS fit of the binned data is shown as the solid black line and highlights the overall trend through the data. The tourmaline-derived temperatures show good agreement with temperature estimates from other geothermometers. Meta-pelite tourmalines define a consistent prograde temperature history, whereas the tourmaline in the tourmalinite shows two-stage growth with formation of its core at constant T, followed by prograde growth that is consistent with the temperature history of the meta-pelite.

Additional temperature information can be obtained from garnet-ilmenite thermometry (Pownceby et al. 1987). This is particularly useful here because it can provide temperature constraints on garnet formation from the abundant ilmenite inclusions within it. Rim compositions of the garnet and especially the ilmenite in samples 248482 and 248484 are not suited to Mn-exchange thermometry given their low X_{Mn} (*cf.* Fig. 1 in Pownceby et al. 1987), resulting in calculated temperatures well above the melting point of these rocks. Inclusions in the mantle zone result in a mean T of 530 ± 65 ˚C for sample 248484, and 415 ± 35˚C for the core in both samples, with an overall progressive increase in T from core to mantle. Garnet-ilmenite pairs in sample 248483 similarly give unlikely temperatures for the garnet rim, where it contains abundant tourmaline inclusions. Ilmenite inclusions in the garnet mantle result in variable temperatures of 580 ± 70˚C with no apparent temperature trend. Ilmenite inclusions in the core were too small to analyse.

There is excellent agreement between these temperature estimates and those derived from tourmaline thermometry (Fig. 20). Peak temperatures recorded by tourmaline match, within uncertainty, with the temperatures derived from garnet rims and matrix biotite. Ilmenite inclusions in garnet cannot precisely be located within the tourmaline temperature history, but the temperatures derived from these are consistent with the approximate locations, and indicate that garnet is cogenetic with the tourmaline. Specifically, the core and mantle of the garnet in the meta-pelite formed during prograde growth, with garnet appearing at equivalent conditions to the tourmaline, and the rim represents peak conditions as per the garnet-biotite thermometry results.

In summary, peak metamorphic pressure and temperature conditions for the meta-pelite samples and the tourmalinite are indistinguishable within uncertainty, which we interpret to indicate a common metamorphic event. The prograde path, as recorded by sector-zoned tourmaline, is similar in initial tourmaline nucleation temperature (~400˚C), but markedly different in subsequent prograde trend. Whereas tourmaline the meta-pelite shows a progressive and consistent increase in temperature, tourmaline in the tourmalinite grows at near constant temperature of ~350˚C for at least 50% of its growth, followed by a rapid, or even stepwise increase towards peak metamorphic conditions (Fig 21). We interpret this as a two-step growth history, with the mantle and rim attributed to the regional metamorphism recorded by the meta-pelite tourmalines, whereas the core records an event not represented in the host meta-pelite.

4.1.2 Greenschist-hosted tourmaline vein

Tourmaline inter-sector thermometry was applied to pairs consisting of ***c***-sector cores that could be attributed to sector zoning given colour and compositional systematics (see van

Hinsberg and Schumacher 2007) and their immediately adjacent ***a***-sectors. These are blue and dark green cores in the larger tourmaline grains at the edge of the tourmaline vein, as well as the blue and brown cores in accessory tourmalines in the greenschist matrix. Even the larger grains on the edge of the tourmaline vein are small (~ 10 μm diameter), which makes single zone analyses challenging. The best sector zoning analyses provide a vein formation temperature of 410 ± 30°C (n = 7) calculated from Ca partitioning and 470 ± 65°C (n = 3) from Ti partitioning. We prefer the Ca derived temperatures given the low Ti content of these tourmalines (< 0.05 pfu) coupled with low Ti mobility in typical natural systems at low temperature, but the temperature results are within uncertainty. Disseminated accessory tourmaline grains in the matrix give 465 ± 30°C (n = 3, Ca) and 400°C (n = 1, Ti), *i.e.* indistinguishable from those calculated for the tourmaline vein. These temperature estimates agree with the greenschist-facies mineral assemblage of this sample and suggest that the minerals reflect a common equilibration stage. Moreover, the equivalent T of tourmaline formation in the vein and as accessory grains in the matrix supports the interpretation based on progressive tourmaline colour variations that all tourmaline results from B-metasomatism.

4.2 Thermodynamic modeling

The tourmalinite has been interpreted in previous studies to represent the metamorphosed equivalent of a B-rich protolith (Appel 1984). Tourmalinites can also form by B-metasomatism and to test this hypothesis, we conducted forward thermodynamic modelling to determine the changes in mineral paragenesis, mode and composition during progressive B introduction into an aluminous protolith. This also allows us to test the viability of various potential protoliths, in particular the enclosing meta-pelites.

Results are shown in Fig 23a,b and indicate that B-metasomatism of neither the host meta-pelite unit (248484), nor associated felsic metasediments (248481 from Bolhar et al. 2005) could produce the tourmalinite, with the principal issues a lack of sufficient Al in the former and Fe + Mg in the latter that prohibit reaching the observed tourmaline mode in the tourmalinite. A maximum tourmaline mode of 30% is possible for the meta-pelite unit, whereas only 12% tourmaline would be able to form in the more quartzo-feldspathic 248482 sample. This confirms the earlier interpretations that the tourmalinite does not represent a tourmalinised equivalent of its host lithologies. It is worth noting that at the observed tourmaline mode for each sample, the pseudosections predict the observed mineral paragenesis for the *P*-*T* conditions derived from geothermobarometry.

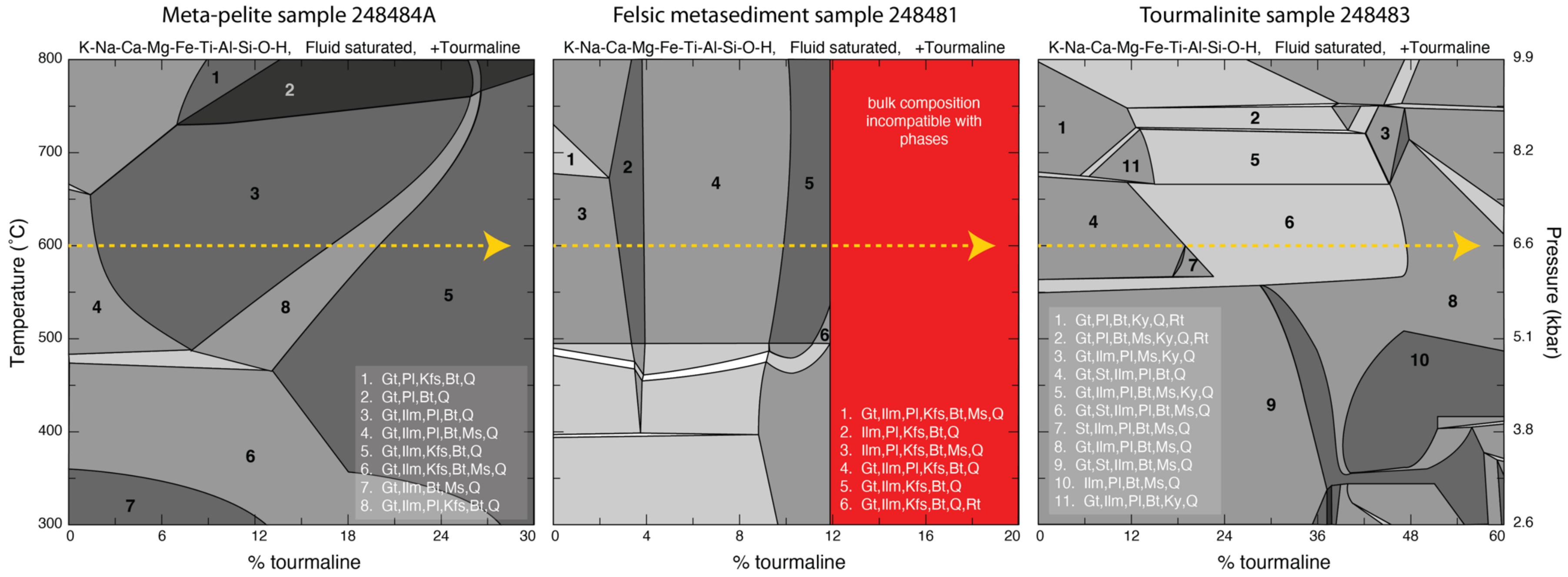

Figure 23: Mineral stability pseudosections calculated using Perple_X and showing changes in paragenesis as a result of progressive introduction of B. Metasomatism was calculated along a geothermal gradient and the yellow arrow shows the evolving mineral paragenesis at 600°C for: A. Meta-pelite bulk rock composition from From Bolhar et al. 2005 sample 248484-A; B. Felsic metasediment bulk rock composition from Bolhar et al. 2005; and C. Tourmalinite composition calculated from EPMA data and point counting of mineral modes in thin section. Only the calculated bulk composition for the tourmalinite would be able to form the mode of tourmaline observed with the other samples limited to 30 and 12%, respectively.

The bulk composition for tourmalinite 248483-VIII calculated from the mineral modes in its thinsections and corresponding mineral compositions determined by EPMA indeed differs from 248482 and 248484 mainly in its Al_2O_3 content, which is twice that of the other two samples. Removing tourmaline from this composition, using the mean tourmaline composition in the sample and a mode of 55%, results in a bulk composition that is similar to 248482 and 248484, but strongly enriched in Al and Ca and depleted in Mg. Given that Al is immobile under most crustal conditions, this likely reflects a protolith difference. Progressive B-metasomatism of this composition leads to sharp changes in mineral paragenesis, mode and composition (Fig 23c), commencing, at the *P*-*T* conditions of the sample, with the introduction of muscovite as Mg + Fe are progressively incorporated in the tourmaline whereas K is not. Staurolite subsequently disappears. Garnet remains stable as it accommodates the Ca left over from the lower Ca/Na ratio of the tourmaline compared to that of the bulk rock. The predicted final paragenesis fits that which is observed, including the characteristic abundance of muscovite, and the absence of staurolite despite the high Al content. Moreover, the modelling predicts steps in X_{Mg} and X_{Ca} for garnet that are not linked to changes in *P*-*T* conditions, which match the lack of consistent compositional trends from core to rim in the garnets in this sample (Fig. 15,16). Although not direct proof, the modelling is consistent with this sample being the result of metasomatic introduction of B into an Al-rich protolith variant of the mafic and felsic schists.

4.3 Tourmaline genesis

4.3.1 Greenschist-hosted tourmaline vein sample

The tourmaline vein sample reflects external, open-system introduction of boron. Tourmaline is present in this sample as fine-grained fibrous tourmaline in the vein, and larger grains on the vein rim and in the matrix of the greenschist host of the vein. The fibrous texture in the vein suggests rapid crystallisation of tourmaline, with nucleation dominating over growth, and the flow and pull apart textures of the fibres indicate formation of a mush of fibres that was aligned during flow and locally pulled apart. Tourmaline fibres are regarded as direct proxies for the composition of the fluid from which they formed (Dutrow and Henry 2000, 2018). Using the average temperature of formation from inter-sector thermometry of 422°C and the temperature – fluid composition relationships established by (Goerne and Franz 2000; Goerne et al. 2001, 2011) provides estimates for the Na and Ca concentration in the vein-forming fluid of 0.33 and 0.03 mol L^{-1}, respectively.

The vein-forming fluid also infiltrated into the host schist where it introduced B and led to the formation of disseminated tourmalines, as evidenced from the systematic trends in com–position and colour away from the vein, and the equivalent formation temperatures derived from tourmaline inter-sector thermometry. Apatite also formed because of metasomatism and shows systematic trends in size and composition with vein distance. The fluid composition calculated for the discrete and matrix tourmaline grains is less sodic and more calcic with Na decreasing to 0.27 mol L^{-1} away from the vein and Ca increasing to 0.04 mol L^{-1}. We interpret this increase in Ca/Na ratio to reflect a progressively larger contribution to tourmaline composition from the host rock.

The matrix minerals in the greenschist host are in equilibrium with matrix tourmaline and the mineral paragenesis is in agreement with the formation temperature of the tourmaline. The same minerals are also observed in contact with the vein tourmaline, both in schist enclaves within the vein, and at schist-vein contacts. None of the tourmaline grains show cores that could be interpreted as detrital or reflecting an earlier episode of growth. There are compositionally-distinct amphibole cores and inclusions in larger grains that reflect an earlier metamorphism, with amphibole-plagioclase geothermometry (Putirka, 2008) indicating higher-grade amphibolite-facies conditions, in agreement with the metamorphic conditions generally accepted for the garbenschieffer unit (Nutman et al., 2022). However, these are relicts and the main metamorphic conditions represented by the sample are greenschist-facies. We therefore conclude that this sample reflects an equilibrium state where tourmaline and apatite were introduced by metasomatism, and the host schist silicate minerals re-equilibrated to the *P*-*T* conditions.

4.3.2 Meta-pelite

Tourmaline is a disseminated, accessory phase in the meta-pelites with local concentration in mica-rich bands. Tourmaline rims show textural equilibrium with the peak metamorphic minerals, but the grains are all concentrically zoned, indicating that they record a growth history of changing *P*-*T* and/or fluid compositions. Inter-sector thermometry shows that tourmaline appeared at *ca.* 350°C and subsequently grew on the prograde path up to the peak metamorphic conditions. A number of grains show minor retrograde growth at the rim, leading to a stronger sector contrast. These growth zones are at the analytical resolution in terms of analyses, but suggest temperatures that are *ca.* 70°C below the peak conditions, which is well above the predominant retrograde overprint that leads to chloritization of biotite and garnet and sericitization of plagioclase. There is excellent agreement in this temperature history with other geothermometers (Fig 22), and this agreement, moreover, shows co-genesis of tourmaline and garnet.

Tourmaline has an overall mode that is identical to that found in modern meta-pelites (e.g. van Hinsberg and Schumacher 2011; Berryman et al. 2017). Unfortunately, the bulk B content of these samples is unknown, but in amphibolite-facies meta-pelites, tourmaline is generally the dominant host for B (Henry and Dutrow 1996; Leeman and Sisson 1996), and we can therefore conclude that the B content of these samples is equivalent to that in modern meta-pelites. The textures, temperatures and compositions of these tourmalines are, moreover, indistinguishable from those observed for typical, modern meta-pelites (e.g. van Hinsberg and Schumacher 2011; Berryman et al. 2017), and we conclude that the appearance and growth of tourmaline in these samples represents progressive redistribution of B into tourmaline during metamorphism under more-or-less closed-system conditions (fluid-loss will have occurred during prograde metamorphism and will have removed soluble elements). Boron in this sample thus reflects protolith-derived boron.

4.3.3 Tourmalinite

The tourmalinite was previously interpreted as either a metamorphosed B-rich protolith (proposed to be of submarine exhalative origin) deposited in the meta-pelite sequence as a block given that the tourmalinite banding is discordant with the host schist foliation (Appel 1984), or as a tectonically dismembered tourmaline vein introduced during metamorphism based on tourmalinite zircon ages postdating the protolith age, but being consistent with metamorphism (Nutman et al. 2000). Grew et al. (2015) support the sedimentary origin for the unit based on the mineralogy and aluminous nature.

Our interpretation differs, and we neither support the B-rich protolith nor the dismembered vein hypotheses. Instead, we interpret the tourmalinite to represent B-metasomatism of an aluminous member of the meta-pelite lithology, which was subsequently dismembered and rotated into its current configuration during subsequent metamorphism. This is based on several arguments:

1. The bulk-rock composition of this unit does not match typical sedimentary B-rich protolith candidates. Rather than high B, its main characteristic is its high Al content. The thermodynamic modelling indicates that it is not possible to grow the amount of tourmaline observed here in the adjacent meta-pelites because they lack sufficient Al.
2. Aluminium is largely immobile in typical metamorphic fluids, which suggests that the high Al content of the tourmalinite is a primary feature.
3. Inter-sector thermometry shows that nucleation and *ca.* 50% of the subsequent growth of the tourmaline took place at a constant temperature, which was followed by prograde growth up to the regional peak metamorphic conditions. This indicates

two stages of tourmaline growth, of which the second part is prolonged. This is incompatible with a tourmaline-vein origin.

4. Garnet grains in the tourmalinite have textures identical to garnets in the adhering schist, the host micaschist (248482) and the meta-pelite host lithology (248484). These garnets are in equilibrium with the tourmaline as shown by mutual inclusion textures and their growth spans the appearance of tourmaline in the sample. As such, the garnet cannot represent inherited grains, and, rather, the garnet and tourmaline are co-genetic. Geothermometry involving garnet shows that it records a prograde metamorphic history. This argues against a vein origin.
5. The compositions of the tourmaline core are near-constant, especially for the ***c+*** sector (Fig. 21). Given the abundance of tourmaline in these samples (mode is ~60%), and a tourmaline composition that differs markedly from that of the bulk rock (higher X_{Mg} and lower Ca + K), Raleigh fractionation would have occurred under closed-system conditions leading to compositional zoning in the tourmaline. Instead, there is no such zoning, with the absence of zoning in X_{Mg} most striking. This strongly suggests an external control on tourmaline composition under open-system conditions.
6. The composition of the tourmaline mantle and rim does vary, and this composition correlates with temperature (e.g. X_{Mg} versus T). This shows that the tourmaline composition was responding to its environment post-core.
7. Compositional zoning in the tourmalinite garnet is complex and appears to show steps rather than a smooth profile. The thermodynamic modelling predicts such a complex profile as progressively B-metasomatism leads to changes in paragenesis and mineral modes.
8. The tourmalinite is characterised by, locally abundant, peak-metamorphic muscovite, whereas the enclosing meta-pelite schists are biotite-dominated. The thermodynamic modelling shows that this would be expected in a B-metasomatism scenario and results from sequestering of Mg + Fe by tourmaline with residual enrichment in K +Al.

9. The tourmaline mantle and rim temperature history is consistent with the prograde metamorphic history recorded by the enclosing schists, and suggests a common history of the lithologies from this point onward.

These arguments lead us to an interpreted history where an influx of B from an external fluid results in formation of abundant tourmaline in an aluminous member of the meta-pelite unit at constant T and with a fluid-controlled composition. This event predates metamorphism, but at a temperature of *ca.* 350°C, it is not sedimentary nor diagenetic in nature. The isotopic composition for the tourmaline cores in the tourmalinite is consistent at $\delta^{11}B$ = -22 ‰ (Grew et al. 2015). Such a light B-isotopic composition has been found in tourmalines that formed in granite-related veins, and at Broken Hill in non-marine evaporite deposits (Marschall and Jiang 2011), and is not in itself diagnostic for the B source. However, it is does not fit a marine B source as observed in tourmalines in submarine massive sulfide deposits, for example.

Following this B-metasomatism, the tourmalinite lithology shares the metamorphic history of its current host rocks, indicating that these lithologies are together from this point inward. Their markedly different structural orientation in the field may reflect the large difference in rock competence, with the tourmalinite having acted as a competent boudin that was rotated into its current orientation during the deformation that accompanied the prograde metamorphism. The rotation and continuity in mica foliation at the contact of tourmalinite and host schist supports this interpretation. Growth of the tourmaline during prograde metamorphism is interpreted to result from B-redistribution into tourmaline from phases that break down on the prograde path as well as possible growth of larger grains at the expense of smaller ones in an Ostwald ripening process. The correlations between T and mantle + rim tourmaline composition, and the convergence in composition between host schist and tourmalinite tourmalines argues against further B-metasomatism, and rather supports growth under closed-system conditions.

4.4 Geochronology

4.4.1 Tourmaline vein

Apatite and tourmaline are co-genetic as discussed above, which allows apatite to be used to date the vein formation and B-metasomatism event. A complication in this case is that we cannot assume the common Pb isotopic composition to have been constant for all apatite grains as they could represent variable contributions of elements from the host rock and the external metasomatizing fluid. However, we can use the common Pb isotopic composition of tourmaline in the tourmaline vein as an estimate of the fluid common Pb composition, given that tourmaline preferentially incorporates Pb while taking up negligible U and has a closure temperature sufficiently high to preserve the Pb-isotopic composition deposits (Marschall and Jiang 2011). In fact, tourmaline has a $^{207}Pb/^{206}Pb$ of 1.117 ± 0.033, whereas a value of 1.145 ± 0.023 results when apatite data is included (Fig. 18), *i.e.* within error, which indicates that the fluid controlled the Pb isotopic composition of the apatite and there was no significant contribution from the host rock.

The resulting age for the B-metasomatism event is 1721 ± 76 Ma (2SE). This age is much younger than the accepted protolith age of 3.7 Ga for the host schists (Nutman et al. 2022) and indicates that the B metasomatism represents a distinct, and much younger event. This age overlaps with limited felsic magmatic ages in the area of 1623 ± 65 Ma and 1610 ± 130 Ma, which (Nutman et al. 2022) have provisionally assigned to a 1.6 Ga continental break-up stage at the start of the Mesoproterozoic.

4.4.2 Meta-pelite and tourmalinite

The zircon analyses for the host meta-pelite unit define a discordia with an upper intercept age of 3724 ± 42 Ma, and a lesser defined lower disturbance event at 1790 ± 141 Ma (Fig. 17a). The age derived here is consistent with earlier results of 3.71 Ga by zircon U-Pb chronology (Nutman et al. 1997, 2022) and 3.74 ± 0.05 Ga by Nd-Sm whole-rock chronology

(Kamber et al. 1998). These ages are taken to represent the age of the protolith, as the zircons are interpreted as magmatic grains in the volcanic sediments. The lower intercept matches the age derived from apatite in the tourmaline vein and suggests that this event did not only lead to tourmaline-veining and B-metasomatism, but also partially reset the zircon chronometer, which would be consistent with it reflecting a regional event, as postulated at ~1.6 Ga of (Nutman et al. 2008; 2022).

Zircon analyses in the tourmalinite also define a discordia extending to an upper intercept that matches 3 concordant analyses. These concordant analyses define an age of 3595 ± 11 Ma (Fig. 17b). Earlier zircon dating of this tourmalinite yielded ages from 3590 to 3560 Ma (Nutman et al. 2000), which were interpreted as the age of metamorphism. These ages are consistent with our results as is the interpretation given that the zircons we dated were present in the matrix of the sample and could have formed during metamorphism in that they are not present in the cores of the tourmaline where they would reflect an earlier stage. Given that the B-metasomatism that produced the abundant tourmaline in this sample predates the metamorphism, but post-dates protolith deposition, the age of this event is between 3.7 and 3.6 Ga. Intrusion of pegmatites and granite sheets is known for the northern Isua belt at 3620 to 3630 Ma and could be a potential source of fluid and B (Nutman et al. 2000).

5. Conclusions and implications

Tourmaline in the northern part of the Isua belt has complex histories and formed in response to at least three events. The oldest tourmaline identified here results from B-metasomatism of an aluminous member of the meta-pelite unit at between 3.7 and 3.6 Ga, and results in the formation of a tourmalinite. This age, and the major element and B-isotopic composition of the tourmaline are consistent with formation linked to granitic magmatism and resulting fluid activity in the area. Disseminated tourmaline grains in the meta-pelite unit, as well as the tourmaline mantle and rim in the tourmalinite are attributed to prograde to peak metamorphism, with the peak of metamorphism dated to 3.6 Ga. The tourmaline mode in the meta-pelite is consistent with B-contents for typical meta-pelitic protoliths, and growth of tourmaline is postulated to have taken place under largely closed-system conditions. The B in these samples is therefore interpreted as protolith-derived. Thirdly, an overprint event at 1.7 Ga partially resets the zircon chronometer in the meta-pelite and leads to metasomatism in the garbenschiefer unit with introduction of tourmaline and apatite. This event takes place at greenschist-facies conditions and given that the sample's mineralogy has almost fully re-equilibrated at these conditions and the fact that it is also observed in the meta-pelite suggests that it reflects a significant retrograde overprint event with regional extent. It overlaps within age uncertainty with the regional thermal overprint at 1.6 Ga of (Nutman et al. 2008; 2022), which they link to continental break-up at the start of the Mesoproterozoic. In summary, tourmaline formation can be linked to two distinct B metasomatism events that affected the Isua belt almost 2 Gy apart, as well as to prograde metamorphism over a 300°C thermal history.

The complexity of tourmaline formation in Isua has important implications for extracting information from tourmaline regarding the sources of its constituent elements and the nature and composition of the protolith, and, by extension, the Archean surface environment. Particular focus has been on using tourmaline as an indicator of the B cycling, B content and B isotopic composition of the Archean hydrosphere (Chaussidon and Appel 1997; Grew et al. 2015), given its implications for the origins and earliest evolution of life (Mishima et al. 2016; Ricardo et al, 2004). Such inferences require that the tourmaline grows from protolith B, and our results indicate that this is only the case for the samples where tourmaline is a minor, accessory phase, with the other examples representing externally derived, metasomatic B. The abundance of tourmaline in these latter samples does, therefore, also not imply high B in Archean surface environments. Even for samples where tourmaline can be taken to have formed under closed-system conditions, *i.e.* the disseminated accessory grains in the meta-pelite, the growth history is prolonged and spans prograde conditions from 350 to 650°C. Tourmaline compositions vary significantly from core to rim, and isotopic compositions vary alongside (see core-rim profiles Grew et al. 2015). Tourmaline boron-isotopic fractionation is strongly temperature dependent (Meyer et al. 2008; Marschall et al. 2009) and any attempt to work out the B-isotopic signature of the formation fluid, or to work back to that of the protolith (*cf.* Grew et al. 2015) thus requires information on the formation temperature of any growth zone for which the B-isotopic composition was determined.

In conclusion, Isua tourmaline grains hold a treasure-trove of information on the origins and development of the Isua greenstone belt, but to interpret this information correctly requires a careful assessment of how tourmaline formed, when it formed, and what process or event it provides information on. Ironically, the samples with the smallest tourmaline mode hold the greatest potential for reconstructing aspects of B content and cycling in the Archean surface environments. With regards to this specific type of occurrence, our results indicate tourmaline contents, textures and growth histories that are identical to those observed in modern meta-pelites, suggesting that B contents in protolith sediments and B metamorphic cycling to have been equivalent in the Archean.

6. References

Appel, P. (1984) Tourmaline in the Early Archean Isua Supracrustal Belt, West Greenland. Journal of Geology, 92: 599-605.

Appel, P. and Chaussidon, M. (1997) Boron isotopic composition of tourmalines from the 3.8-Ga-old Isua supracrustals, West Greenland: implications on the δ^{11}B value of early Archean seawater. Chemical Geology, 171-180

Appel, P.W.U. (1984) Tourmaline in the Early Archaean Isua Supracrustal Belt, West Greenland. The Journal of Geology, 92, 599–605.

Appel, P.W.U. (1995) Tourmalinites in the 3800 Ma old Isua supracrustal belt, West Greenland. Precambrian Research, 72, 227–234.

Arai, T., Omori, S., Komiya, T., Maruyana, S. (2015) Intermediate P/T-type regional metamorphism of the Isua Supracrustal Belt, southern west Greenland: The oldest Pacific-type orogenic belt? Tectonophysics, 662, 22-39

Bebout, G., Nakamura, E. (2003) Record in metamorphic tourmalines of subduction-zone devolatilization and boron cycling. Geology, 31, 5, 407-410

Berryman, E.J., Kutzschbach, M., Trumbull, R.B., Meixner, A., Hinsberg, V. van, Kasemann, S.A., and Franz, G. (2017) Tourmaline as a petrogenetic indicator in the Pfitsch Formation, Western Tauern Window, Eastern Alps. Lithos, 284–285, 138–155.

Bhattacharya, A., Mohanty, L., Maji, A., Sen, S.K., and Raith, M. (1992) Non-ideal mixing in the phlogopite-annite binary: constraints from experimental data on Mg–Fe partitioning and a reformulation of the biotite-garnet geothermometer. Contributions to Mineralogy and Petrology, 111, 87–93.

Boak, J. L., Dymek, R. F. (1982) Metamorphism of the ca. 3800 Ma supracrustal rocks at Isua, West Greenland: implications for early Archaean crustal evolution. Earth and Planetary Science Letters, 59, 1, 155-176

Bosi, F. (2018) Tourmaline crystal chemistry. American Mineralogist, 103, 298–306.

Burt. D. M. (1989) Vector representation of tourmaline compositions. American Mineralogist, 74, 7-8, 826-839

Caro, G., Bourdon, B., Birck, J.-L., and Moorbath, S. (2006) High-precision ^{142}Nd/^{144}Nd measurements in terrestrial rocks: Constraints on the early differentiation of the Earth's mantle. Geochimica et Cosmochimica Acta, 70, 164–191.

Caro, G., Bourdon, B., Birck, J.-L., and Moorbath, S. (2003) ^{146}Sm–^{142}Nd evidence from Isua metamorphosed sediments for early differentiation of the Earth's mantle. Nature, 423, 428–432.

Chaussidon, M., and Appel, P. (1997) Boron isotopic composition of tourmalines from the 3.8-Ga-old Isua supracrustals, West Greenland: Implications on the delta B-11 value of early Archean seawater. Chemical Geology, 136, 171–180.

Chemenda, A. I., Mattauer, M., Malavieille, J., Bokun, A. N. (1995) A mechanism for syn-collisional rock exhumation and associated normal faulting: results from physical modelling. Earth and planetary science letters, 132, 1-4, 225-232.

Chew, D.M., Petrus, J.A., and Kamber, B.S. (2014) U–Pb LA–ICPMS dating using accessory mineral standards with variable common Pb. Chemical Geology, 363, 185–199.

Connolly, J.A.D. (2005) Computation of phase equilibria by linear programming: A tool for geodynamic modeling and its application to subduction zone decarbonation. Earth And Planetary Science Letters, 236, 524–541.

Connolly, J.A.D., and Petrini, K. (2002) An automated strategy for calculation of phase diagram sections and retrieval of rock properties as a function of physical conditions. Journal of Metamorphic Geology, 20, 697–708.

Čopjaková, R., Prokop, J., Novak, M., Losos, Z., Skoda, R., Hola, M. (2020) Hydrothermal alteration of tourmaline from pegmatitic rocks enclosed in serpentinites: Multistage processes with distinct fluid sources. Lithos, 380-381

Crowley, J. (2003) U–Pb geochronology of 3810–3630 Ma granitoid rocks south of the Isua greenstone belt, southern West Greenland. Precambrian Research, 126, 3, 235-257

Dutrow, B.L., and Henry, D.J. (2000) Complexly zoned fibrous tourmaline, cruzeiro mine, minas gerais, brazil: a record of evolving magmatic and hydrothermal fluids. The Canadian Mineralogist, 38, 131–143.

Dutrow, B.L., and Henry, D.J. (2018) Tourmaline compositions and textures: reflections of the fluid phase. Journal of Geosciences, 99–110.

Fedo, C. (2000) Setting and origin for problematic rocks from the >3.7 Ga Isua Greenstone Belt, southern west Greenland: Earth’s oldest coarse clastic sediments. Precambrian Research, 101, 1, 69-78

Fox, G., Fink, G. (1934) The Piezoelectric Properties of Quartz and Tourmaline. Physics. 5, 10, 302-306

Frie, R., Bridgewater, D., Rosing, M., Stecher, O. (1999) Controversial Pb-Pb and Sm-Nd isotope results in the early Archean Isua (West Greenland) oxide iron formation: Preservation of primary signatures versus secondary disturbances. Geochimica et Cosmochimica Acta, 63, 473-488

Furnes, H., de Wit, M., Staudigel, H., Rosing, M., & Muehlenbachs, K. (2007) A vestige of Earth's oldest ophiolite. Science, 315, 5819, 1704-1707

Georgieva, M., Little, C., Maslannikov, V., Glover, A., Ayupova, N., Herrington, R. (2021) The history of life at hydrothermal vents. Earth-Science Reviews, 217, 1-20

Goerne, G. von, and Franz, G. (2000) Synthesis of Ca-tourmaline in the system CaO-MgO-Al_2O_3-SiO_2-B_2O_3-H_2O-HCl. Mineralogy and Petrology, 69, 161–182.

Goerne, G. von, Franz, G., and Heinrich, W. (2001) Synthesis of tourmaline solid solutions in the system Na_2O-MgO-Al_2O_3-SiO_2-B_2O_3-H2O-HCl and the distribution of Na between tourmaline and fluid at 300 to 700 °C and 200 MPa. Contributions to Mineralogy and Petrology, 141, 160–173.

Goerne, G. von, Franz, G., and Hinsberg, V.J. van (2011) Experimental determination of Na–Ca distribution between tourmaline and fluid in the system CaO–Na_2O–MgO–Al_2O_3–SiO_2–B_2O_3–H_2O. Canadian Mineralogist, 49, 137–152.

Grew, E.S., Dymek, R.F., Hoog, J.C.M.D., Harley, S.L., Boak, J., Hazen, R.M., and Yates, M.G. (2015) Boron isotopes in tourmaline from the ca. 3.7–3.8Ga Isua supracrustal belt, Greenland: Sources for boron in Eoarchean continental crust and seawater. Geochimica et Cosmochimica Acta, 163, 156–177.

Hackler, R.T., and Wood, B.J. (1989) Experimental determination of Fe and Mg exchange between garnet and olivine and estimation of the Fe-Mg mixing properties in garnet. American Mineralogist, 74, 994–999.

Hanmer and Greene, (2001) A modern structural regime in the Paleoarchean (~3.64 Ga); Isua Greenstone Belt, southern West Greenland. Tectonophysics, 346, 3, 201-222

Haselton, H.T., Hovis, G.L., Hemingway, B.S., and Robie, R.A. (1983) Calorimetric investigation of the excess entropy of mixing in analbite-sanidine solid solutions; lack of evidence for Na,K short-range order and implications for two-feldspar thermometry. American Mineralogist, 68, 398–413.

Hawthorne, F., and Henry, D.J. (1999) Classification of the minerals of the tourmaline group. European Journal Of Mineralogy, 11, 201–215.

Hazen, R., Ausubel, J. (2016) On the nature and significance of rarity in mineralogy. American Mineralogist, 101, 1245-1251

Henry, D.J., and Dutrow, B.L. (1996) Metamorphic tourmaline and its petrologic applications. In E. Grew and L. Anovitz, Eds., Boron: Mineralogy, Petrology and Geochemistry Vol. 33, pp. 503–557. Boron.

Henry, D.J., Guidotti, C.V., and Thomson, J.A. (2005) The Ti-saturation surface for low-to-medium pressure metapelitic biotites: Implications for geothermometry and Ti-substitution mechanisms. American Mineralogist, 90, 316–328.

Hinsberg, V J van, Henry, D.J., and Dutrow, B.L. (2011) Tourmaline as a Petrologic Forensic Mineral: A Unique Recorder of Its Geologic Past. Elements, 7, 327–332.

Hinsberg, V.J. van, and Schumacher, J.C. (2007) Intersector element partitioning in tourmaline: a potentially powerful single crystal thermometer. Contributions to Mineralogy and Petrology, 153, 289–301.

Hinsberg, V.J. van, and Schumacher, J.C. (2011) Tourmaline as a petrogenetic indicator mineral in the Haut-Allier metamorphic suite, Massif Central, France. The Canadian Mineralogist, 49, 177–194.

Hinsberg, V.J. van, Franz, G., and Wood, B.J. (2017) Determining subduction-zone fluid composition using a tourmaline mineral probe. Geochemical Perspectives Letters, 160–169.

Hinsberg, V.J. van, Schumacher, J.C., Kearns, S., Mason, P.R.D., and Franz, G. (2006) Hourglass sector zoning in metamorphic tourmaline and resultant major and trace-element fractionation. American Mineralogist, 91, 717–728.

Hinsberg, V.J., Marschall, H.R., (2007) Boron isotope and light element sector zoning in tourmaline: implications for the formation of B-isotopic signatures. Chemical Geology, 238, 141–148

Hinsberg, V. J. van, Henry, D.J., and Marschall, H.R. (2011) Tourmaline: An Ideal Indicator of Its Host Environment. Canadian Mineralogist, 49, 1–16.

Hodges, K.V., and Crowley, P.D. (1985) Error estimation and empirical geothermobarometry for pelitic systems. American Mineralogist, 70, 702–709.

Holdaway, M.J. (2001) Recalibration of the GASP geobarometer in light of recent garnet and plagioclase activity models and versions of the garnet-biotite geothermometer. American Mineralogist, 86, 1117–1129.

Holland, T.J.B., and Powell, R. (2011) An improved and extended internally consistent thermodynamic dataset for phases of petrological interest, involving a new equation of state for solids. Journal of Metamorphic Geology, 29, 333–383.

Jahns R. H., Wright L. A. (1951) Gem- and lithium-bearing pegmatites of the Pala district, San Diego County, California.

Kamber, B.S., Collerson, K.D., Moorbath, S., and Whitehouse, M.J. (2003) Inheritance of early Archaean Pb-isotope variability from long-lived Hadean protocrust. Contributions to Mineralogy and Petrology, 145, 25–46.

Kamber, B.S., Moorbath, S., and Whitehouse, M.J. (1998) Extreme Nd-isotope heterogeneity in the early Archaean—fact or fiction? Case histories from northern Canada and West Greenland—Reply. Chemical Geology, 148, 219–224.

Komiya, T., Hayashi, M., Maruyama, S., & Yurimoto, H. (2002). Intermediate-P/T type Archean metamorphism of the Isua supracrustal belt: implications for secular change of geothermal gradients at subduction zones and for Archean plate tectonics. American Journal of Science, 302, 9, 806-826

Kurki, J., Keto, L. (1966) 1966 report on geological investigations at Isua 1966. Kryolitselskabet Øresund A/S Prospekting report, 20219

Lambert, R.S.J. (1983) Proterozoic Geology: Selected Papers from an International Proterozoic Symposium. Geological Society of America Memoirs, 155–166.

Leeman, W.P., and Sisson, V.B. (1996) Geochemistry of boron and its implications for crustal and mantle processes. Reviews in Mineralogy and Geochemistry, 33, 645–707.

Marschall, H., Wanless, V., Shimizu, N., Pogge von Strand, P., Monteleone, B. (2017) The boron and lithium isotopic composition of mid-ocean ridge basalts and the mantle. Geochimica et Cosmochimica Acta, 207, 102-138

Marschall, H.R., and Jiang, S.-Y. (2011) Tourmaline Isotopes: No Element Left Behind. Elements, 7, 313–319.

Marschall, H.R., Meyer, C., Wunder, B., Ludwig, T., and Heinrich, W. (2009) Experimental boron isotope fractionation between tourmaline and fluid: confirmation from in situ analyses by secondary ion mass spectrometry and from Rayleigh fractionation modelling. Contributions To Mineralogy and Petrology, 158, 675–681.

McDowell, F.W., McIntosh, W.C., and Farley, K.A. (2005) A precise ^{40}Ar–^{39}Ar reference age for the Durango apatite (U–Th)/He and fission-track dating standard. Chemical Geology, 214, 249–263.

McLennan, J. (1981) Trace element geochemistry of sedimentary rocks: Implications for the composition and evolution of the continental crust. PhD thesis, Australian National University.

Meyer, C., Wunder, B., Meixner, A., Romer, R.L., and Heinrich, W. (2008) Boron-isotope fractionation between tourmaline and fluid: an experimental re-investigation. Contributions To Mineralogy and Petrology, 156, 259–267.

Mishima, S., Ohtomo, Y., Kakegawa, T., (2016) Occurrence of Tourmaline in Metasedimentary Rocks of the Isua Supracrustal Belt, Greenland. Implications for Ribose Stabilization in Hadean Marine Sediments. The Journal of the International Study for the Origin of Life, 46, 247-271

Mohan, M., Kamber, B., Piercy, S. (2008) Boron and arsenic in highly evolved Archean felsic rocks: Implications for Archean subduction processes. Earth and Planetary Science Letters, 274, 479-488

Moorbath, S., Onions, R.K., Pankhurst, R.J. (1973) Early Archean Age for Isua Iron Formation, West Greenland. Nature 245, 5421, 138–139

Moorbath, S., Whitehouse, M.J., and Kamber, B.S. (1997) Extreme Nd-isotope heterogeneity in the early Archaean — fact or fiction? Case histories from northern Canada and West Greenland. Chemical Geology, 135, 213–231.

Myers, J.S., (2001) Protoliths of the 3.8–3.7 Ga Isua greenstone belt, West Greenland, Precambrian Research, 105, 2-4, 129-141

Newton, R.C., Wood, B.J., and Kleppa, O.J. (1981) Thermochemistry of silicate solid solutions. Bulletin de Minéralogie, 104, 162–171.

Nutman, A., Bennett, V., Friend, C. (2015) The emergence of the Eoarchean proto-arc: evolution of a c. 3700 Ma convergent plate boundary at Isua, southern west Greenland. Geological Society, London, Special Publications, 389, 1, 113-133

Nutman, A., Bennett, V., Friend, C., Yi, K. (2020) Eoarchean contrasting ultra-high-pressure to low-pressure metamorphisms (<250 to >1000 C/GPa) explained by tectonic plate convergence in deep time, Precambrian Research, 344

Nutman, A., Friend, C. (2009) New 1:20,000 scale geological maps, synthesis and history of investigation of theIsua supracrustal belt and adjacent orthogneisses, southern West Greenland: A glimpse of Eoarchaean crust formation and orogeny. Precambrian Research, 172, 3, 189-211.

Nutman, A.P., Bennett, V.C., Friend, C.R.L., and Mcgregor, V.R. (2000) The early Archaean Itsaq Gneiss Complex of southern West Greenland: the importance of field observations in interpreting age and isotopic constraints for early terrestrial evolution. Geochimica et Cosmochimica Acta, 64, 3035–3060.

Nutman, A.P., Bennett, V.C., Friend, C.R.L., and Rosing, M.T. (1997) ~ 3710 and ⩾ 3790 Ma volcanic sequences in the Isua (Greenland) supracrustal belt; structural and Nd isotope implications. Chemical Geology, 141, 271–287.

Nutman, A.P., Friend, C.R.L., Bennett, V.C., Yi, K., and Kranendonk, M.V. (2022) Review of the Isua supracrustal belt area (Greenland) Eoarchean geology from integrated 1:20,000 scale maps, field observations and laboratory data: Constraints on early geodynamics. Precambrian Research, 379, 106785.

Paton, C., Hellstrom, J., Paul, B., Woodhead, J., and Hergt, J. (2011) Iolite: Freeware for the visualisation and processing of mass spectrometric data. Journal of Analytical Atomic Spectrometry, 26, 2508.

Petrus, J.A. and Kamber, B.S. (2012) VizualAge: A novel approach to laser ablation ICP-MS U-Pb geochronology data reduction. Geostandards and Geoanalytical Research, 36, 247–270.

Pownceby, M.I., Wall, V., and O'Neill, H.S. (1987) Fe-Mn partitioning between garnet and ilmenite: experimental calibration and applications. Contributions To Mineralogy and Petrology, 97, 116–126.

Putirka, K.D. (2008) Thermometers and Barometers for Volcanic Systems. Reviews in Mineralogy and Geochemistry, 69, 61–120.

Ricardo, A., Carrigan, M. A., Olcott, A. N., Benner, S. A. (2004) Borate minerals stabilize ribose. Science, 303, 5655, 196-196

Rosing, M., Amils, R., Gargaud M., Cernicharo Quinta, J., Irvine, W., Pinti, D., Viso, M. (2014) Isua Supracrustal Belt. Encyclopedia of Astrobiology.

Schoene, B. and Bowring, S.A. (2006) U–Pb systematics of the McClure Mountain syenite: thermochronological constraints on the age of the ^{40}Ar/^{39}Ar standard MMhb. Contributions to Mineralogy and Petrology, 151, 615–630.

Sláma, J., Košler, J., Condon, D.J., Crowley, J.L., Gerdes, A., Hanchar, J.M., Horstwood, M.S.A., Morris, G.A., Nasdala, L., Norberg, N., Schaltegger, U., Schoene, B., Tubrett, M.N., and Whitehouse, M.J. (2008) Plešovice zircon — A new natural reference material for U–Pb and Hf isotopic microanalysis. Chemical Geology, 249, 1–35.

Sperlich, R., Giere, R., Frey, M., (1996) Evolution of compositional polarity and zoning in tourmaline during prograde metamorphism of sedimentary rocks in the Swiss Central Alps. American Mineralogist, 81, 1222–1236

Stacey, J.S. and Kramers, J.D. (1975) Approximation of terrestrial lead isotope evolution by a two-stage model. Earth and Planetary Science Letters, 26, 207–221.

Stern, R.A., Bodorkos, S., Kamo, S.L., Hickman, A.H., and Corfu, F. (2009) Measurement of SIMS Instrumental Mass Fractionation of Pb Isotopes During Zircon Dating. Geostandards and Geoanalytical Research, 33, 145–168.

Szilas, K., Kelemen, P., Rosing, M. (2015) The petrogenesis of ultramafic rocks in the > 3.7 Ga Isua supracrustal belt, southern West Greenland: Geochemical evidence for two distinct magmatic cumulate trends. Gondwana Research, 28, 2, 565-580

Vázquez-Mayagoitia, A., Horton, S. R., Sumpter, B. G., Sponer, J., Sponer, J., Fuentes-Cabrera, M. (2011) On the stabilization of ribose by silicate minerals. Astrobiology, 11, 2, 115-121

Vermeesch, P. (2018) IsoplotR: A free and open toolbox for geochronology. Geoscience Frontiers, 9, 1479–1493.

Waterton, P., Guotana, J. M., Nishio, I., Tani, K., Woodland, S., Legros, H., Pearson, D. G., Szilas, K. (2021) No mantle residue in the Isua Supracrustal Belt. Earth and Planetary Science Letters, 579

Webb, A. A. G., Müller, T., Zuo, J., Haproff, P. J., Ramírez-Salazar, A. (2020) A non–plate tectonic model for the Eoarchean Isua supracrustal belt. Lithosphere, 12, 1, 166-179

White, R W, Powell, R., and Johnson, T.E. (2014) The effect of Mn on mineral stability in metapelites revisited: New a-x relations for manganese-bearing minerals. Journal of Metamorphic Geology, 32, 809–828.

White, R. W., Powell, R., Holland, T.J.B., Johnson, T.E., and Green, E.C.R. (2014) New mineral activity–composition relations for thermodynamic calculations in metapelitic systems. Journal of Metamorphic Geology, 32, 261–286.

White, R.W., Powell, R., and Clarke, G.L. (2002) The interpretation of reaction textures in Fe-rich metapelitic granulites of the Musgrave Block, central Australia: constraints from mineral equilibria calculations in the system K_2O–FeO–MgO–Al_2O_3–SiO_2–H_2O–TiO_2–Fe_2O_3. Journal of Metamorphic Geology, 20, 41–55.

Wiedenbeck, M., Allé, P., Corfu, F., Griffin, W.L., Meier, M., Oberli, F., Von Quadt, A., Roddick, J.C., and Spiegel, W. (1995) Three natural zircon standards for U-Th-Pb, Lu-Hf, trace element and REE analyses. Geostandards Newsletter, 19, 1–23.

Zawaski, M. J., Kelly, N. M., Orlandini, O. F., Nichols, C. I., Allwood, A. C., Mojzsis, S. J. (2020) Reappraisal of purported ca. 3.7 Ga stromatolites from the Isua Supracrustal Belt (West Greenland) from detailed chemical and structural analysis. Earth and Planetary Science Letters, 545, 116409

Appendix:
Additional Thin Section Descriptions

M248482 (and 248482B) - garnet biotite schist

Sample M248482 is a biotite schist with biotite, quartz, and plagioclase defining the foliation. The plagioclase is altered to sericite. The garnets are fractured and are included with various minerals, primarily plagioclase and quartz. Biotite is the major phyllosilicate phase defining the foliation with additional muscovite. There is some alteration on the garnet rims to chlorite, like the garnets in M248484-K. The garnets in this sample do not have the clear growth zones that are present in the other garnet bearing samples. These garnets are heavily included and fractured throughout with no inclusion poor rims, the inclusions are pervasive through the entire grains and they are homogeneous in texture. There is little or no rotation of these garnets, no tails, and no pressure shadows.

This sample has both oxides and sulfides present, and commonly the oxides are overgrowing the sulfides (and vice versa). The sulfides have distinct textures associated with them, which looks like small inclusions or some sort of dissolution texture. The edges are irregular and hackly in appearance. Some of the oxides have a similar texture to the sulfides but it is less common. When sulfides nucleate off oxides the texture of the internal oxide is irregular. The boundaries look to be grainy and non-geometric which is a disequilibrium texture.

There is epidote/zoisite present in this TS similar to those of the other tourmaline rich samples. They are inclusion rich and have idiomorphic contacts with surrounding minerals (altered plagioclase, micas, quartz). Epidote in the thin section has high interference colors in xpl and shows idiomorphic grains that are discordant with the foliation.

There is also staurolite present in this sample, which was lacking in the other schist samples. The staurolite is in good condition and was likely formed at the peak of metamorphism.

Minerals Present:

Plagioclase – Almost all the plagioclase in this sample has gone through pervasive alteration and shows sericitization. There are some localized pockets of unaltered feldspar, but they are rare. Grains tend to be small. Present as matrix and as inclusions in garnet. Some grains show sericitization concentrated to grain boundaries, however other show random patterns.

Sericite – alteration of plagioclase. Sericite is extremely common in this sample and almost all of the matrix plagioclase has been altered to sericite. Retrograde phase.

Garnet – No growth zones. Only one generation of garnet growth. Highly included, staurolite near garnet rims. No rotation, pressure shadows, or tails associated with the garnets. Some of the garnets are being replaced by green chlorite, similar to the tourmalinites and other schists.

Chlorite – Chlorite is present within fractures in quartz veins (retrogression/alteration of bt?), and it is present on the rims of garnets in this sample as well. There is also a dark blue (XPL) fibrous generation of chlorite in this sample. It is rarer and green in PPL, forming fibrous sheath and intergrown with retrogressed plagioclase.

Quartz – Much of the quartz in this sample has begun and aborted the process of recrystallization. This is clearly seen along quartz grain boundaries as sub grains have formed but the new boundaries are not clear. There are also some highly birefringent grains (in XPL) associated with this recrystallization which are likely anhedral epidote.

Biotite – Makes the foliation with plagioclase and quartz. Present in relatively high abundance.

Muscovite – Minor phase. Most of the phylosilicates in this sample are biotite.

Oxides – There is a interesting relationship between the oxides and sulfides in this sample. Some of the oxides have overgrowths of sulfides, and some of the sulfides have overgrowths of oxides. Oxides are present as inclusions in garnet and as part of the matrix.

Pyrite/Chalcopyrite – nucleates around oxides, and has oxides nucleate around it. Disequilibrium textures associated with the oxide/sulfide contacts. Relatively common in sample 248482 and 248482B.

Staurolite – presence of staurolite is significant – it is indicative of a drop in pressure and increase in temperature during its formation. Good for creating pseudosections and constraining temperature and pressure of peak paragenesis.

Epidote – Small grains (50-150um) discordant with the foliation. High second order in xpl, core is so texturally granular that it is impossible to see interference colors and rims lack inclusions. High relief in ppl. The irregular core is likely due to it being allanite and the rim being epidote which is a common feature seen in the epidotes from the tourmaline rich boulder.

Tourmaline – Accessory phase. Grains are small and anhedral, they tend to lack inclusions, are rounded and perpendicular to the foliation. Bluish to greenish in PPL.

M248484-K - Mica-garnet schist

Overview –

M248484-K is mica (bt-mus) rich garnet schist. This is a typical schist with the foliation consisting of biotite, muscovite, quartz, and plagioclase with porphyroblastic garnets with abundant inclusions. Oxides and tourmaline are also present in the foliation as accessory phases. All phases are all in equilibrium with each other and they were all formed on the prograde path as there is not any textural evidence for the retrograde growth or replacement of minerals, besides chlorite infilling fractures within the garnet which is a retrograde hydration process. The grain boundaries are geometric indicating equilibrium.

The garnets have gone through a low degree of rotation which has led to the formation of small pressure shadows in the low strain areas. These shadows commonly have more oxides and quartz relative to the rest of the sample. The garnets have an inclusion rich core and inclusion poor rim, and variable mantles depending on the specific garnet. The garnets have been rotated due to shearing.

The tourmaline in the sample is an accessory phase formed on the prograde path. The tourmaline is in equilibrium with the micas, garnet, oxides, and all other components of the sample, and is forming a lineation perpendicular to the foliation formed by the micas and elongate quartz grains (i.e the tourmaline are mainly visible perpendicular to the c-axis as opposed to parallel to c). They are rarely zoned and some have inclusions in the cores. They appear bluish in PPL and are rounded.

The only phase that is out of equilibrium is chlorite which was likely formed on the retrograde path due to the breakdown of micas or garnet. The chlorite is concentrated to the fractures in garnets and to the rims of garnets where it nucleates from the fracture/rim surfaces. Quartz is a major phase in this sample. Along with the micas it forms the foliation and extends the length of the thin section.

Minerals Present

Major –

Quartz – Defines foliation along with biotite. Highest abundance of grains. Have gone through some deformation in the form of shearing. When there are pressure shadows present in the low strain zone of the garnets there is a high concentration of quartz, which was recrystallized.

Plagioclase— The plagioclase in this sample is commonly twinned. It does not comprise a major component of the sample, however it is present as one of the main phases. There is not a high abundance of plagioclase in contact with garnets.

Biotite — High abundance of biotite. Many grains in contact with garnet (as inclusions and along the rim of garnets). Well-formed and in equilibrium with the rest of the assemblage. Zircon inclusions in biotite are indicated by reaction halos, however they are small or under the surface of the biotite.

Garnet— Garnets in this sample are inclusion rich in the cores and poor in the rims. The garnets have gone through a low degree of rotation which has formed pressure shadows associated with some of the garnets. The garnets are the largest grains (2+ mm) in this thin section and formed at peak conditions.

Chlorite— The chlorite in this sample is the sole retrograde phase. It is concentrated to fractures within the garnets. These fractures were then infilled by fibrous chlorite, and it also nucleates on the external edge of garnet grains. Although the chlorite is fibrous, there are distinct crystals that form these fibers and they radiate into the matrix when forming on the rims of garnet.

Oxides— The oxides present are magnetite (cubic) and ilmenite (elongate). The oxides are well formed and occur in every part of the sample, but the highest abundance of them is concentrated to the pressure shadows of the garnets. This is the only sample that has both ilmenite and magnetite.

Accessory –

Tourmaline – Prograde mineral. Accessory phase of low abundance. In equilibrium with the rest of the assemblage. Generally some growth zoning from core to rim, however some grains are homogeneous. It is difficult to see if there are polar overgrowths due to the orientation of the tourmaline (most are cut perpendicular to c axis). Many of the tourmaline are restricted to the zones of high strain (foliation) and they are not present in the pressure shadows. There are a few tourmalines that appear as inclusions in garnet. Some of the tourmalines have inclusion rich cores and inclusion poor rims in this sample.

Amphibole — Few grains of amphibole present based on multiple (60/120) directions of cleavage. Brown in PPl and dark brown in XPL.

Sulfides — There are some accessory sulfides present, however they are a minor component of the sample. The sulfides are likely pyrite or chalcopyrite due to the bright yellow color in reflected light and they are associated with oxides (commonly act as cores for nucleation of oxides).

Epidote – Epidote occurs sporadically throughout the sample, commonly associated with biotite. It is inclusion rich and in equilibrium with the biotite that it is in contact with. There are also some grains of this which lie oblique to the foliation. The epidote is well formed and have idiomorphic contacts, which high second order interference colors in XPL.

248484-M1 – mica garnet schist

Large Scale Features –

The foliation is defined by muscovite, biotite, quartz and plagioclase (muscovite is more abundant, but biotite is also present). There is a fold in the middle of the thin section indicative of compression. Plagioclase is abundant in this sample (especially near this fold) relative to M2, and it has been slightly altered to sericite (less so than sample 248482). Garnets are strongly altered and the garnet on the bottom of the TS shows inclusions lining up with an original foliation (inclusions are not perpendicular to the orientation of the foliation indicative of some degree of rotation). The top left garnet is altering to chlorite, like the garnets in sample M2, 248482B, and the tourmalinite samples. The chlorite alteration is associated with both garnet and biotite. The chlorite in this is also proximal to both garnets and biotite which is similar to M2. Tourmalines are present throughout the sample and are oriented parallel to the foliation, and commonly fractured relative to the foliation showing that they formed early. They are idiomorphic and zoned (sector and growth). They are also present as inclusions in retrogressed garnets like sample M1.

There are elongate oxides that run parallel to the biotite foliation. Relative to M2 this sample has more biotite and less muscovite and the oxides are generally concentrated to the biotite zones. Muscovite flows around the garnet that is less pervasively altered to chlorite, and biotite rims the garnet that has been replaced by chlorite. This variable appearance of garnets in the same thin section has been noted in many of the samples.

Minerals Present

Tourmaline – Most of the tourmalines are small and cut perpendicular to the c-axis. They are scattered throughout the thin section and bluish and lack clear zoning in this orientation. They are in a variety of locations, some included in garnets, some associated with the muscovite/biotite foliation, and some which are in areas rich in plagioclase. They are not concentrated to specific locations and are ubiquitous throughout the sample.

Garnet – The garnets in this sample are like the ones in M2, although one of the garnets in M1 has gone through less alteration. The pervasive green chlorite is present on the top left garnet, and there are similarities in the inclusions as well. There is a small pressure shadow of plagioclase in this sample (similar to M2)..

Biotite – Abundant in this sample and defines the foliation along with muscovite. Proximal to green chlorite alteration zones. There are 2 generations present based on the crosscutting relationships seen.

Muscovite – More abundant than biotite and forms the foliation along with biotite. Proximal to the garnet and based on the contacts it appears that the garnet has been slightly rotated and the mica has accommodated the strain associated with this deformation event. Large grains, commonly associated with plagioclase rich areas.

Plagioclase – Abundant, especially abundant near the fold. Most of the plagioclase is unaltered, and the grains that have been sericitized have not been fully replaced.

Ilmenite – Present running parallel to foliation and elongate. Highest quantity of oxides is associated with the biotite foliation. Along with this, the oxides are lacking near the plagioclase.

Chlorite – Similar to M2. Replaced garnets, but it is less apparent in this sample. It appears that there is both chlorite and chloritoid present in this sample based on the crystals present in the garnets.

Accessory Minerals: **Allanite**

248484-M2 – chlorite/mica garnet schist

Large Scale Features:

The sample is a chlorite garnet schist. The garnets are retrogressing green chlorite. The chlorite is localized to the areas around the garnets. The foliation is defined by chlorite, and there are additional discordant muscovite rich areas near garnets. There are many tourmaline grains and oxides that follow the chlorite foliation. There are idiomorphic contacts between the tourmaline and chlorite. There are kink bands associated with the muscovite near some of the garnets. Due to the retrogressed nature of the garnets, it is difficult to determine if they have gone through any degree of rotation. The bottom garnet that has been replaced has a square shape with the associated chlorite and it is almost a perfect 90deg angle due to the sectioning of the thin section.

The tourmaline in the sample is oriented parallel to the foliation with some grains oriented perpendicular to it and some randomly oriented with no respect to the micas. They are elongate and well-formed showing strong zoning. Many of them are elongate and unfractured. They are not concentrated to one specific area of the thin section and are present as clusters of grains, single grains, inclusions in chlorite (retrogressed garnet) and as inclusions in garnet.

Minerals Present:

Garnet – Partly to fully retrogressed by chlorite. Grains that are not fully replaced are enveloped by chlorite with garnet relics. The garnets have a variety of inclusions mostly being oxides, tourmaline, and epidote. The rims are clearly replaced by chlorite, and the original shape of the garnets can be seen.

Tourmaline – Abundant throughout the sample, and it occurs in different expressions. Most of the tourmaline is scattered through the chlorite and muscovite. When in muscovite it is perpendicular to the foliation, and when in the chlorite they lie parallel. They are prograde and most likely formed in the same event as these micas.

The next expression of the tourmaline is from within the alteration zone associated with the chlorite and garnets. Near the rim of this zone there are some included tourmaline.

There is also tourmaline present as inclusions in the garnets. This is especially apparent in the garnets on the right side of the TS (away from label). Most of the tourmaline inclusions in garnet are in the garnet rims – there is an exception in the bottom right (square) garnet where there are also inclusions in the “core”, but this might not be the true core depending on the cut of the TS.

Muscovite – Multiple generations of muscovite with some grains are crosscutting earlier foliations. abundant throughout the thin section, similar abundance to chlorite which is the other major phase present. Many other grains are concentrated to the muscovite foliation and are oriented parallel to it (tourmalines and oxides). Muscovite overprints chlorite near a garnet.

Chlorite – multiple generations of chlorite – the bright green retrograde chlorite is only present proximal to the garnets that are being altered.

Primary chlorite is present in other parts of the thin section and makes up a significant part of the host rock. It is black and white in XPL and low relief and colorless in PPL. It is overprinted by muscovite in some areas.

Biotite – Altering to chlorite and proximal to most retrograde chlorite. Lower in abundance than muscovite and chlorite, but still present in appreciable amounts.

Ilmenite – Ilmenite is concentrated to the muscovite and chlorite rich areas and is likely formed at the same times as these phases due to this relationship. They are abundant in this sample and mostly appear as elongate thin grains.

Plagioclase – Forms a pressure shadow around the altered garnets on the left, however due to a lack of rotation this may be an anomoly.

Allanite – Extremely common, present throughout the sample and related to epidote in many cases.

Epidote – Present throughout the sample, especially common in the altered garnets.

M472823 – metasomatic tourmaline vein

Overview –

Sample M472823 contains a large dark colored micro-tourmaline vein in contact with quartz and other accessory minerals (micas, amphibole, carbonate, plagioclase, quartz, additional tourmaline). The vein is deformed, but the deformation is localized to the edges, and to areas near pockets/large fractures. There are kink bands which is indicative of shearing and compressional strain, and as the tourmaline grains are small this led them to them accommodating the deformation

Minerals present –

Tourmaline – highest abundance, in the form of a microcrystalline tourmaline vein as well as fibrous crystals in the fractures. The tourmaline varies in color from an olive green within the core of the vein to a lighter blue color on the edge of the vein. There are many tourmalines growing off the vein and these are zoned with a green/brown interior and a blue rind. We do not see the olive/brown tourmalines in the sample that we see in the matrix of the vein.

Quartz – Quartz is present and is the second most abundant mineral in the sample. The quartz infills fractures and it also flanks the edge of the tourmaline vein. It looks undeformed and does not look recrystallized. The quartz is present throughout the sample, and it is not limited to isolated areas. There are numerous areas in the sample where there is a high abundance of fibrous tourmaline within in the quartz. The quartz has irregular grain boundaries and lacks undulose extinction.

Carbonate – Low abundance and restricted to the fractures for the most part.

Amphibole – There is a large quantity of amphibole present relative to the other accessory minerals. Some of the grains are in contact (or overprinted) by the tourmaline vein and others are above the vein mainly in contact with quartz and other accessory minerals. They are highly fractured and cleaved with irregular grain boundaries. In XPL the amphiboles are yellow to dull brown to high second order with distinct cleavage planes intersecting at 60/120deg. They are equant and somewhat rounded grains, with some showing a skeletal texture. In SEM imaging there are multiple generation of amphibole depending on where one is in the thin section, and they are distinctly compositionally different from each other. The multiple generations of amphibole show irregular contacts and hackly looking rims. The second generation of amphibole and the chlorite are in equilibrium with each other.

Micas/Chlorite – There is both biotite and muscovite present in this sample, albeit in low abundances. The micas are not oriented in any direction. Chlorite is present in low abundance near the fractures associated with the top part of the TS.

Plagioclase – The plagioclase has gone through extensive alteration. There are almost no coherent grains as it has altered to sericite. The grain boundaries are irregular, and although the twinning of the plagioclase can be seen it is often overprinted with sericite. Some of the grains appear to be almost completely replaced by sericite.

Epidote – Small highly birefringent grains are present throughout the fracture system, and they are euhedral grains with some of them being highly included. They are in equilibrium with the matrix and the contacts are idiomorphic.

M472823 B and C – tourmaline vein and chlorite rich amphibolite (host)

Overview –

M472823B shows the same metasomatic tourmaline vein that is present in M472823, however this portion of the vein is in contact with the host rock whereas the other sample lacks this matrix component. The tourmaline vein is in proximity to a quartz vein below it, however they are not in contact with each other. The edge of the tourmaline vein shows idiomorphic zoned tourmalines growing into the matrix. Below the quartz vein the tourmaline has a different expression than it has within the tourmaline vein. The tourmaline which are part of the host are more olive/brown in color and they contain abundant inclusions. The tourmaline vein has a similar deformation texture to the vein in sample M472823, however this sample has less kink bands.

Sample 472823-B has a high modal abundance of chlorite in the host which constitutes most of the matrix. This is primary chlorite. The zoisite/epidote in this thin section is much more abundant, and it is also replacing other minerals which were rhombohedral/wedge shaped. These replaced minerals overprint plagioclase in multiple instances. Zoisite/epidote forms as individual crystals and as inclusions in the quartz vein. The quartz vein extends the length of the thin section, and it is relatively thin. The quartz looks to have not gone through recrystallization due to the lack of 120deg triple junction grain boundaries. The quartz vein itself is undeformed and has many inclusions (tourmaline, zoisite, amphiboles, and some pockets where the full host composition). There is a small portion of the quartz vein in direct contact with the tourmaline vein. On the top left of the TS there is fibrous tourmaline growing off the vein into a plagioclase rich area where there is also amphibole and zoisite present. There is two generations of chlorite present, one of which is in equilibrium with the amphibole (primary) and a later generation which is in disequilibrium with the amphibole (retrograde).

Minerals present and their relationships –

Tourmaline – The tourmaline in this sample is not restricted to the tourmaline vein. It is present in the vein (highest abundance), as inclusions within the quartz vein (close to the host rock) as well as in the chlorite/amphibole matrix as discrete grains with numerous inclusions. The nature of the tourmaline is not homogenous throughout the sample. The vein is composed of microcrystalline grains accommodating deformation and the grain size is very fine (<5um). The tourmaline that is distal to the vein is in equilibrium with the chlorite and forms large (150+ um) idiomorphic grains with numerous inclusions. They are olive green to brown in comparison with the blue/green vein, and this color is accompanied by increased Ti concentrations. The inclusions are quartz and plagioclase with some embayments where the bulk rock composition is seen.

Micas – Micas are rare in this sample; the phyllosilicate minerals are chlorite.

Chlorite – Chlorite is the most abundant mineral in this thin section. The chlorite in this sample is composed of two generations. One of the generations of chlorite is in equilibrium with the amphibole (first, primary generation) and one of the generations is not in equilibrium with the amphiboles. The primary black and white chlorite is in equilibrium with the tourmaline below the quartz vein, however there is a lack of chlorite above the quartz vein. The chlorite is also in disequilibrium with the zoisite and epidote.

Amphibole – The first generation of amphiboles in this sample are in disequilibrium with the peak paragenesis. There are large cores and smaller rims present on these grains. Some of the grains appear to be in equilibrium with the chlorite whereas others are in disequilibrium. This shows that one generation of the amphibole is prograde (cores) and the other is retrograde (rims).

Epidote/Zoisite – The epidote/zoisite in this sample is variable. Some of the grains formed as inclusions in the quartz vein, some are discrete and in the chlorite matrix, and zoisite has replaced some rhombohedral minerals in the zone between the tourmaline vein and the quartz vein. It forms sharp rhombohedral crystals near each other although this would not be the expected morphology that one would see for zoisite. The zoisite is not in equilibrium with the chlorite and is likely part of the amphibolite facies paragenesis, subsequently altered by a retrograde reaction.

Quartz – There is a quartz vein separating the tourmaline vein from the rest of the rock. Between the quartz vein and the tourmaline vein there is a zone where the plagioclase has been extensively altered the sericite.

Titanite – Titanite in these samples appears in multiple ways. One expression is a hydrothermal texture which is irregular and skeletal. The grains fill interstitial spaces between epidote, amphibole, and chlorite. The grains are generally less than 20um, however some of the grains are up to 100um. They are common throughout the sample. They are also expressed as overgrowths on rutile, ilmenite, and apatite. These overgrowth rims are less than 25um and the grains tend to be equant and rounded. They are unzoned.

Accessory Minerals:

Apatite – Low abundance, grains are rounded and equant. Some apatite acts as nucleation points for titanite, and alternatively some apatite nucleated around preexisting oxides.

Rutile – Core of some titanite grains. Not present in matrix besides as inclusions.

Zircon – Trace. All grains <10um. When present very metamict.

472823-D – matrix/host of tourmaline vein

Host rock of metasomatic tourmaline vein –

This thin section is from the host rock of the metasomatic tourmaline vein. There is no microtourmaline vein in this sample, however there are discrete tourmaline grains present within the matrix. The tourmalines are brownish grains and commonly form in small clusters or as isolated grains proximal to each other. The tourmaline grains are heavily included and show some zoning in PPL and XPL (light colored cores, other grains are homogenous). They are present in moderate quantities,

Most of this host rock is chlorite. It is black and white wispy chlorite (primary). It appears to be out of equilibrium with many of the epidote and amphibole grains (but in equilibrium with some of the grains that show secondary growth) present in the thin section which shows that it is likely retrograde and replaced the original host (maybe mica). As noted previously, the matrix has titanite in many different expressions. There is no banding in these samples, and the main noteworthy largescale features are the quartz vein cutting the sample.

Minerals Present –

Amphibole – Abundant in the host rock. Core and rims commonly have different compositions, grains commonly 500um or larger. Similar to previously mentioned amphiboles from 472823.

Tourmaline – Tourmaline is relatively abundant throughout this sample. It occurs as large, heavily included, brownish, zoned grains. The zoning goes from a light blue core to a light brown rim. Most of the tourmaline is proximal to the quartz veins which would introduce the B-rich metasomatic fluid to the host rock. Light blue tourmaline cores seem to lack inclusions, however the growth zones directly next to them are inclusion rich. Grains are commonly 200um or larger and idiomorphic.

Epidote/Zoisite –Epidote is overprinting many of the other minerals present. Some of the epidote grains have a core which has been altered (or heavily included) and then an unaltered rim of a different composition.

Chlorite – Primary chlorite constitutes the matrix of this sample. It is black and white, randomly oriented, and throughout the entire thin section. The chlorite matrix is cut by quartz veins. Amphiboles are in disequilibrium with chlorite, however tourmaline and epidote are in equilibrium with chlorite.

Oxides – Sparce and small. Some oxides act ac nucleation points for titanite grains. Titanite nucleation around is equant, blobby, and anhedral. Sizes of ~20um or less.

Titanite – irregular shape and small (some >50um, although most are smaller than this). Skeletal with many of the ends coming to sharp points. Filling spaces between epidote, amphibole, and chlorite grains. Also expresses itself as overgrowths on ilmenite, rutile, and apatite. These overgrowths are equant and rounded with an anhedral shape. None of the titanites present have the characteristic wedge shape.

Apatite – in matrix – relatively large grains when present (50-100um). Some apatite grains act as nucleation points for titanite, however this is rarer than the oxides acting as nucleation points. Present in matrix and as inclusions.

Rutile – nucleation points of titanite, odd. Inclusion assemblage as it is not present anywhere else in the sample. Small grains only identifiable on SEM.

Zircon – Trace phase. All grains less than 10um.

248483-1 – Garnetiferous Tourmalinite

Large Scale Features –

Tourmalinite – tourmaline is abundant and makes up most of the sample. The tourmaline is cut parallel to the c-axis. The tourmalines are highly included with polymineralic inclusions which are representative of the host composition. They are extensionally fractured, and at this fracture interface there is an abundance of chlorite running the length of the sample. Along with this expression of chlorite it is replacing muscovite in parts of the sample, and it replaces garnet as well (like M1 and M2).

There are garnets and garnet fragments both present in this sample which is different from sample IV but consistent with sample VIII. The garnets have been altered to chlorite and they contain abundant tourmaline inclusions which is important for determining the timing of tourmaline introduction (prograde path due to them being inclusions). This thin section has oxides that are expressed in two ways – one of the ways is as inclusions in tourmaline and these are generally equant, and the other expression is as elongate grains associated with the muscovite and chlorite. The matrix of the sample is altered and most of the plagioclase has altered to sericite. There are epidote grains within the matrix that are small and highly birefringent.

Minerals Present –

Oxides – Equant and rounded oxides which is a deviation from samples M1 and M2 where the oxides are almost all elongate. Most oxides in this sample are present as inclusions in tourmaline and are in textural equilibrium.

Tourmaline – The most abundant mineral in the sample. They are elongate and heavily included with polymineralic inclusions, quartz, and oxides. Many of the tourmaline have complexly zoned cores which can be seen due to the light blue cores.

Plagioclase – Present throughout the sample. Most of the grains have been altered to sericite, however there is an area where plagioclase replaces garnet and these plagioclase grains do not show the pervasive alterations that the rest shows.

Epidote/Zoisite/Staurolite – Present in the matrix as small highly birefringent grains in XPL. Equant to elongate in shape and upwards of 100um.

Biotite – Minor phase, present in localized areas but not widespread.

Amphibole – Minor phase present only in localized areas. Distinctive cleavage.

Chlorite – Multiple expressions – 1. Similar to M1 and M2 replacing garnet (green), 2. Fracture filling (blue), replacing muscovite (blue).

Garnet – Garnet is expressed as fragments and partial crystals. Some of the garnets are replaced by chlorite and there are tourmalines proximal to both the tourmaline and garnet.

Accessory Minerals:

Xenotime, Monazite, Allanite, Apatite – All present near altered garnet. Core of apatite and epidote with radiating and intergrown REE rich minerals. Discrete xenotime grains are also present above this area. It is the only local environment in this thin section that has this intergrown relationship of REE minerals and phosphates/silicates.

M248483-VIII – muscovite rich tourmalinite

Large scale features: Tourmaline is extremely abundant in the middle of the thin section and most grains are cut perpendicular to the c-axis. On the righthand side of the TS there is a greater abundance of plagioclase relative to the rest of the TS. Lefthand side of the TS has a much higher abundance of muscovite than the rest of the TS. The overall abundance goes tourmaline > muscovite >> garnet > plagioclase > oxides

There is localized alteration of plagioclase to sericite, but this seems to be concentrated to zones near the rims of garnets. There is some alteration outside of these zones as well, but the alteration is most pervasive at these contacts.

Some tourmaline are included in the rim of the garnets. It is possible that they are not fully included depending on the sectioning of the thin section. The tourmaline is almost all cut perpendicular to the c-axis and they are commonly strongly zoned. Many tourmalines show 4 or more growth zones with characteristic blue cores, olive/light green mantles, and dark green rims (ppl). Tourmalines form a vertical band through the middle of the thin section. The plagioclase on the right of this sample has idiomorphic micas between grains and is almost identical in nature to the ones seen in sample IV. The micas and plagioclase form clean contacts.

There are relatively abundant oxides throughout the TS. The highest abundance of the oxides is near the transition from the mica rich area (left) to the tourmaline rich area (middle). There are no sulfides present. The tourmaline in this sample is equilibrium with garnet (idiomorphic contacts).

Minerals Present:

Tourmaline – 50-60% of the sample is tourmaline. Strongly zoned with blue cores, highly included with quartz, plagioclase, apatite, and rarely small zircon (recognizable based on fracture pattern from breakdown). It is present throughout the thin section but highly concentrated to a band in the middle.

Garnet – Large (2+ mm) and highly included. Inclusions appear to be aligned with each other which likely previously defined a foliation which is not longer present, or has been overprinted by new phases. Zones in garnets can be identified based on quantity of inclusions – similar to the zones seen in the schists. These zones include rims which lack inclusions, mantles which are inclusions rich, and cores of intermediate character. One of the garnets contains a large quartz inclusion lining up with the alignment of the other inclusions.

Muscovite – Muscovite is present in multiple areas in this sample. It defines a foliation on the left hand side of the sample and has numerous tourmaline within the foliation. The muscovites in this area form kink bands, and in ppl the tourmalines in the foliation are a much lighter color (potentially due to the thin section being thinner in this area). The second expression of muscovite appears between plagioclase grains and the muscovite grains are small and in equilibrium with the plagioclase and tourmaline that it is in contact with. Tourmaline overprints some of these muscovite grains.

Plagioclase – Plagioclase is present in pressure shadows/reactions rims near the garnets in this sample, and there is another large cluster of plagioclases on the opposite side of the thin section as the muscovite foliation. There is a low degree of sericite, and it is not as pervasive as sample IV.

Apatite – Apatite occurs as inclusions in garnet and tourmaline.

Chlorite – Retrograde phase, present throughout sample and fills fractures in garnet in many instances.

Oxides – present throughout the sample, within tourmalines and in matrix.

Sericite – Minor retrograde phase.

M248483-IV – tourmalinite

Overview –

Tourmaline makes up about 40% of the assemblage. The tourmaline is oriented parallel making distinct bands, with some clusters and individual grains oriented perpendicular to the banding. The tourmaline overprints and includes the rest of the assemblage, which is plagioclase altering the sericite, muscovite, chlorite (potentially from the alteration of muscovite), biotite, quartz, epidote, and oxides. The tourmaline is large, highly included, and extensionally fractured parallel to the c-axis. The inclusions represent the composition of the host and they are large relative to the size of the tourmaline. Not all the tourmalines are inclusion rich, it is the larger ones that contain the most inclusions.

There is a quartz vein below the tourmaline foliation, and below this quartz vein there are additional tourmalines (smaller and less abundant than above the vein). In this area there is also chlorite along the quartz grain boundaries. There is biotite present in this lower part of the thin section, and although it is present above the quartz vein as well it is in much lower abundance. There is a high abundance of oxides present. They are commonly in contact with or included in tourmalines and they have not gone through alteration. They are elongate and irregular ilmenites. Some of these ilmenites overprint fractures.

Minerals Present –

Tourmaline – Tourmaline is the most abundant mineral in this sample (45-50%). The grains are large (1+mm). They are strongly zoned with blue cores and light to dark green rims. The zones are sharp and many of the grans also appear to be sector zoned based on the wedge shaped formed by the light blue cores. Some of the cores are complexly zoned perpendicular to the c-axis and appear to have “wispy” cores. Tourmaline edges form sharp contacts with the host and grains overprint it. The grains are highly fractured, both extensionally and roughly parallel to the c-axis.

Quartz – Quartz forms veins of varying grain size, although it was undergoing the process of recrystallization based on the texture and formation of subgrains within the vein. The quartz veins wrap around both the top and the bottom of the tourmaline band in the thin section. The subgrains have unclear grain boundaries and the extinction is irregular. Chlorite infills fractures between quartz grains.

Muscovite – Muscovite is a minor phase and is present in between (mostly) unaltered plagioclase grains with idiomorphic grain contacts. These are the only plagioclase grains that are not pervasively altered, and they are spatially unrelated to the tourmalines.

Biotite – The highest abundance of biotite is found below the quartz vein. It is not a major phase.

Chlorite – Fracture filling, retrograde phase. Green in PPL and somewhat fibrous although there are clearly single crystals present. Also present as an extremely fibrous phase where there are no individual crystals visible. This second generation is dark blue in XPL and is spatially associated with amphiboles breaking down.

Plagioclase – Pervasively altered to sericite, although there is also a plagioclase vein that is relatively unaltered above the tourmaline band. This vein has few micas in equilibrium with the plagioclase. Some of the plagioclase is altered to sericite and it is not possible to see any features of the previous plagioclase grains.

Sericite – Abundant alteration product. Almost all plagioclase has been altered to sericite, especially the plagioclase within the tourmaline band.

Ilmenite – Ilmenite is the dominant oxide in this sample. It is present mainly as inclusions in the tourmalines, however it is also present in the matrix. The grains are relatively small (<100um).

Amphibole – Elongate amphiboles are present near chlorite. Due to the orientation only one direction of cleavage can be seen. The external shape of the amphiboles is suggestive of them breaking down to form the blue generation of chlorite.

Accessory Minerals:

Apatite – Mainly present as inclusions in tourmaline

Zircon – Small, well formed, appear to be metamorphic based on the lack of zoning.

Sample Name	Sample Type	Qtz	Bt	Mus	Plg	Tur	Grt	Ep	Ttn	Ilm	Mag	Amp	Cal	St	Chl	Py
248484-K	Schist	x	x	x	x	a	x	a		a	a	t	t		a-r	a
248482	Schist	x	x	x	x	a	x	a		a	a	t	t	a	a-r	a
472823	Met. Vein	a			t	x		t	t			t	t		a	
472823 B	Met Vein + matrix	x		a	a	a		x	a	t		x	a		x-p,r	
472823 C	Matrix of vein	x		x	x	x		x	a	t		x	a		x-p,r	
472823 D	Matrix	x				a		x	a	t		x	a		x-p,r	
248483-IV	Tourmalinite	x	x	x	x	x	x	x		a			t		x-r	
248483-VIII	Tourmalinite	x	x	x	x	x	x	x		a			t		x-r	
248483-1	Tourmalinite	x	x	t	x	x	t	t	t	a			t		x-r	
M1	Boulder Schist (bt/mus)	x	x	x	x	x	x	x		x		x	a		x-r	
M2	Boulder Schist (chl)	x	x	x	x	x	x	x		x		x	a		x-p,r	

Table 2: Paragenesis of each sample – x = major phase, a = accessory phase, t = trace phase. If label followed by (r) it is a retrograde phase, and p,r if both primary and retrograde.